Local AGN Survey (LASr): I. Galaxy sample, infrared colour selection and predictions for AGN within 100 Mpc

D. Asmus,[1,2]★ C. L. Greenwell,[1] P. Gandhi,[1] P. G. Boorman,[1,3] J. Aird,[4] D. M. Alexander,[5] R. J. Assef,[6] R. D. Baldi,[1,7,8] R. I. Davies,[9] S. F. Hönig,[1] C. Ricci,[6,10,11] D. J. Rosario,[5] M. Salvato,[9] F. Shankar,[1] and D. Stern[12]

[1]*Department of Physics & Astronomy, University of Southampton, Hampshire SO17 1BJ, Southampton, United Kingdom*
[2]*European Southern Observatory, Casilla 19001, Santiago 19, Chile*
[3]*Czech Academy of Sciences, Národní 3, 117 20 Staré Mesto, Czechia*
[4]*Department of Physics & Astronomy, University of Leicester, University Road, Leicester LE1 7RJ, UK*
[5]*Centre for Extragalactic Astronomy, Department of Physics, Durham University, South Road, Durham, DH1 3LE, UK*
[6]*Núcleo de Astronomía de la Facultad de IngenierÃŋa y Ciencias, Universidad Diego Portales, Av. Ejército Libertador 441, Santiago*
[7]*Dipartimento di Fisica, Universitá degli Studi di Torino, via Pietro Giuria 1, 10125 Torino, Italy*
[8]*INAF - Istituto di Astrofisica e Planetologia Spaziali, via Fosso del Cavaliere 100, I-00133 Roma, Italy*
[9]*Max Planck Institute for Extraterrestrial Physics(MPE), Giessenbachstr. 1, 85748 Garching, Germany*
[10]*Kavli Institute for Astronomy and Astrophysics, Peking University, Beijing 100871, China*
[11]*George Mason University, Department of Physics & Astronomy, MS 3F3, 4400 University Drive, Fairfax, VA 22030, USA*
[12]*Jet Propulsion Laboratory, California Institute of Technology, 4800 Oak Grove Drive, Pasadena, CA 91109, USA*

Accepted 2020 Mar 12. Received 2019 Dec 19

ABSTRACT

To answer major questions on supermassive black hole (SMBH) and galaxy evolution, a complete census of SMBH growth, i.e., active galactic nuclei (AGN), is required. Thanks to all-sky surveys by the *Wide-field Infrared Survey Explorer* (*WISE*) and the *Spectrum-Roentgen-Gamma* (*SRG*) missions, this task is now feasible in the nearby Universe. We present a new survey, the Local AGN Survey (LASr), with the goal of identifying AGN unbiased against obscuration and determining the intrinsic Compton-thick (CT) fraction. We construct the most complete all-sky galaxy sample within 100 Mpc (90% completeness for $\log(M_*/M_\odot) \sim 9.4$), four times deeper than the current reference, the Two Micron All-Sky Survey Redshift Survey (2MRS), which misses ∼ 20% of known luminous AGN. These 49k galaxies serve as parent sample for LASr, called LASr-GPS. It contains 4.3k already known AGN, ≥ 82% of these are estimated to have $L^{\rm nuc}(12\,\mu{\rm m}) < 10^{42.3}\,{\rm erg\,s^{-1}}$, i.e., are low-luminosity AGN. As a first method for identifying Seyfert-like AGN, we use *WISE*-based infrared colours, finding 221 galaxies at $L^{\rm nuc}(12\,\mu{\rm m}) \geq 10^{42.3}\,{\rm erg\,s^{-1}}$ to host an AGN at 90% reliability. This includes 61 new AGN candidates and implies and optical type 2 fraction of 50–71%. We quantify the efficiency of this technique and estimate the total number of AGN with $L^{\rm int}(2\text{-}10\,{\rm keV}) \geq 10^{42}\,{\rm erg\,s^{-1}}$ in the volume to be 362^{+145}_{-116} ($8.6^{+3.5}_{-2.8} \times 10^{-5}\,{\rm Mpc^{-3}}$). X-ray brightness estimates indicate the CT fraction to be 40–55% to explain the *Swift* non-detections of the infrared selected objects. One third of the AGN within 100 Mpc remain to be identified, and we discuss the prospects for the eROSITA all-sky survey to detect them.

Key words: galaxies: active – galaxies: Seyfert – infrared: galaxies – X-rays: galaxies

1 INTRODUCTION

Today it is commonly accepted that all massive galaxies host a supermassive black hole (SMBH) at their centres. Furthermore, there is increasing evidence that the SMBHs somehow co-evolve with their host galaxies as, for example, indicated by empirical scaling relations between the SMBH mass and galaxy properties, such as the stellar velocity dispersion or stellar mass of the spheroidal component (e.g., Kormendy & Ho 2013; Shankar et al. 2016). The existence of such relations is somewhat surprising given the many orders of magnitude difference in size between the black hole sphere of influence and the bulk of the galaxy. This raises the questions of how the feeding of the SMBH exactly works (e.g., Alexander & Hickox 2012), and if there is significant feedback from the SMBH onto the host galaxies. The latter process is postulated by current cosmological simulations to suppress star formation and explain the galaxy population as observed today in

★ E-mail: d.asmus@soton.ac.uk

the nearby Universe (e.g., Granato et al. 2004; Shankar et al. 2006; Lapi et al. 2006).

The last decades of research have significantly increased our understanding of SMBH growth (see Netzer 2015 for a recent review). We know that SMBHs grow through several phases over cosmic time, during which large amounts of matter are accreted. During its journey towards the event horizon, the material forms an accretion disk which, due to the release of gravitational energy, emits large amounts of radiation, mostly in the ultraviolet (UV) which then is partly reprocessed by surrounding material and secondary processes. As a result, the galaxy nuclei appear as bright compact sources, often outshining the rest of the galaxy. They are called active galactic nuclei (AGN). AGN are bright emitters across most of the electromagnetic range and, thus, detectable throughout the entire visible Universe which allows us to directly trace SMBH growth over cosmic history. In addition, AGN can produce strong outflows which are prime candidates for the feedback onto the host galaxy postulated above. However, to robustly answer which processes are dominating the SMBH growth and the feedback, we require a complete census of the AGN phenomenon. For example, precise knowledge of the AGN number counts in the local Universe would provide tight constraints on the duty cycle of AGN, radiative efficiencies and the luminosity and accretion rate distributions (e.g., Martini & Weinberg 2001; Goulding et al. 2010; Shankar et al. 2009, 2019). Such a census is very challenging to carry out. First of all, the accretion rates of SMBHs span a wide range from essentially zero up to values in excess of the Eddington limit. Therefore, AGN span a huge range in luminosities from the nearly quiescent Galactic Centre, Sgr A*, to the most powerful quasars roughly twelve orders of magnitude more luminous. Faint AGN are difficult to detect, in particular if they do not outshine their host galaxy at some wavelengths. Moreover, the majority of SMBH growth seems to be highly obscured from our lines of sight (e.g., Fabian 1999; Ueda et al. 2014; Buchner et al. 2015; Ricci et al. 2015). So what is the best, i.e., most efficient and least biased, way to find all the AGN? Our best chance to achieve this is certainly in the nearby Universe, where the sensitivity and angular resolution of our instruments can be used to their largest effect for finding and characterising even highly obscured AGN. This is the ultimate goal of the new survey presented here, the Local AGN Survey (LASr). Its design is motivated by the following insights.

1.1 Selecting AGN in the X-ray regime

So far, one of the most successful ways to identify AGN has proven to be in the hard X-ray regime ($\gtrsim$ 10 keV). Here, most AGN are luminous owing to UV photons from the accretion disk being Compton-up-scattered to higher energies by hot electrons. These electrons are most likely part of a coronal region surrounding the innermost accretion disk. As a result, AGN are easily more luminous in X-ray than any other non-transient astronomical objects. Another advantage is that X-ray emission are less affected by extinction than longer wavelength emission. Both reasons together make AGN selection at these energies very reliable. Specifically, the ongoing all-sky scan at 14-195 keV with the Burst Alert Telescope (BAT; Barthelmy et al. 2005) on the *Swift* satellite (Gehrels et al. 2004) provided us with the so far least biased local AGN samples (Markwardt et al. 2005; Tueller et al. 2008; Baumgartner et al. 2013). Prominent examples are the Luminous Local AGN with Matches Analogues sample (LLAMA; Davies et al. 2015; see Riffel et al. 2018 for the Northern analogue) and the BAT AGN Spectroscopic Survey (BASS) samples, e.g., after 70 month scanning time (hereafter B70 AGN sample; Koss et al. 2017; Ricci et al. 2017).

However, even the BAT AGN samples are restricted in two ways. First, the sensitivity of this selection method is relatively low because of the low photon counts. This caveat results in relatively high flux limits, so that even relatively powerful AGN remain undetected by BAT. Second and more importantly, even at such high energies, Compton-thick (CT) obscuration ($N_{\rm H} > 1.5 \cdot 10^{24}\,{\rm cm}^{-2}$) extinguishes the intrinsic flux by factors of ten and larger, resulting in a detection bias against CT obscured AGN. This last point is a severe problem because the intrinsic fraction of CT-obscured AGN is probably around ∼ 30% (e.g., Ricci et al. 2015; Lansbury et al. 2017; Georgantopoulos & Akylas 2019, Boorman et al., in prep.), and possibly even up 50% (Ananna et al. 2019; but see Gandhi et al. 2007). Both caveats will be somewhat mitigated in the future with deeper *Swift*/BAT maps although only slowly as the mission has already reached more than eight years of total integration time. The newest X-ray satellite, the Russian-German "*Spectrum-Roentgen-Gamma*" (*SRG*) mission could allow for advance in this matter. It hosts two telescopes which will perform a four-year all-sky survey at complementary X-ray energies, namely the extended ROentgen Survey with an Imaging Telescope Array (eROSITA; Predehl et al. 2010; Merloni et al. 2012) operating at 0.2-10 keV and the Astronomical Roentgen Telescope - X-ray Concentrator (ART-XC; Pavlinsky et al. 2011, 2018) operating at 4-30 keV. In terms of detecting AGN with their X-ray emission described by a typical power-law, these surveys are expected to be approximately ten times deeper than the current *Swift*/BAT survey. Thus, these surveys are our best chance to probe the local AGN population at sufficient depth, in particular to detect (or place stringent constraints on) many of the still missing CT AGN.

1.2 Selecting AGN in the mid-infrared regime

Complementary to X-ray selection of AGN is selection in the mid-infrared (MIR). About half of the primary emission from the accretion disk is absorbed by dust, surrounding the AGN probably on parsec scales in a more or less coherent structure (see Almeida & Ricci 2017 and Hönig 2019 for recent reviews). As a result, this dust is heated to temperatures of several hundred Kelvins and radiates thermally with the emission peaking in the MIR (∼ 3 to 30 μm). Owing to the more extended and probably clumpy structure of the dust, obscuration becomes a secondary effect at this wavelength regime and usually does not exceed a factor of a few, even in the worst cases (Stalevski et al. 2016). This makes MIR emission a formidable tracer of the primary power of the AGN and allows a highly complete selection. The recent all-sky survey of the *Wide-field Infrared Survey Explorer* (*WISE*; Wright et al. 2010) allowed for the most progress here in the last years, thanks to its high sensitivity and spectral coverage. However, AGN selection in the MIR has some major caveats as well, namely, severe contamination by emission of stellar origin. At shorter wavelengths, $\lesssim$ 6 μm, this includes radiation of old stars, while at longer wavelengths, $\gtrsim$ 6 μm, dust heated by young stars in star forming regions can dominate the total MIR emission of galaxy. Moreover, AGN and intense star formation events often occur together in time and space, e.g., triggered through galaxy interaction and mergers. Therefore, any AGN selection in the MIR is prone to host contamination. Finally, both X-ray and MIR selection are biased against low luminosity and low accretion rate objects, in particular if the SMBH accretes radiatively inefficiently (e.g., Ho 2009). Such systems can be much more efficiently selected at radio wavelengths (e.g., Best et al. 2005; Padovani 2016; Tadhunter 2016; Baldi et al. 2018).

1.3 The new local AGN survey

The discussion above shows that no single selection technique can lead by itself to a complete, unbiased AGN sample (see Hickox & Alexander 2018 for a comprehensive review on AGN selection). Instead a combination of techniques is required. This is the approach of LASr. Specifically, we want to combine the advantages of the high completeness achievable in the MIR and the high level of reliability in the X-rays to identify all efficiently accreting SMBHs. Applied to the all-sky surveys of *WISE* , eROSITA and ART-XC, combined with our nearly complete knowledge of the local galaxy population, LASr should allow us to significantly improve our understanding of the local AGN population and construct the most complete AGN census yet in the nearby Universe with particular focus on the highly obscured objects.

LASr will be performed throughout a series of papers, combining different AGN identification techniques to construct a highly complete AGN sample as final result. In this first paper, we start LASr by selecting the survey volume, assembling the parent sample of galaxies, and employing the first AGN identification technique. Specifically, we create a list of all known galaxies within the volume (Sect. 2) called the LASr galaxy parent sample (LASr-GPS). It will serve as a base sample for the application of different AGN identification techniques. In this paper, we focus on the MIR and use the *WISE* catalogs to first characterise LASr-GPS in terms of completeness and bulge MIR properties (Sect. 3) before starting the AGN census (Sect. 4). This first includes the characterisation of the already known AGN in the volume, followed by the application of the first AGN identification technique, namely by *WISE* colours. This is the most easily-available technique, allowing us to find most of the more luminous AGN in the sample, i.e., those that are more luminous than their host galaxy in at least one *WISE* band. Usually, this is the case for AGN with bolometric luminosities $\gtrsim 10^{43}\,\mathrm{erg\,s^{-1}}$ (e.g., Alexander et al. 2005) and corresponds to AGN classified as "Seyferts" based on their optical emission line ratios. Such AGN probe significant SMBH growth, which seem to be the most relevant for our main science questions, i.e., cases that contribute significantly to the total mass budget of the SMBH and/or cases where sufficient energy is released to have an impact on the host galaxy. The big advantage of MIR colour selection is that it is little affected by obscuration bias, allowing us to identify highly obscured AGN with particular focus on new CT candidates. We discuss the newly found AGN and CT AGN candidates in Sect. 4.4 and Sect. 4.5, respectively, including the prospects to detect them in X-rays. Throughout this work, we will use the so far least biased AGN sample, the B70 AGN sample, in order to characterise the selection steps of LASr AGN. Specifically, the characterisation of the MIR colour-based AGN identification technique employed here allows us to estimate the total number counts of AGN in our volume (Sect. 4.6). This paper is then concluded by a comparison of these numbers to luminosity functions from the literature (Sect. 4.7).

In future papers, we will employ additional MIR-based AGN identification techniques, e.g., variability and SED decomposition, as well as present follow-up observations of AGN candidates. The highly complementary X-ray-based AGN identification can then be provided by the eROSITA and ART-XC all-sky surveys once available.

2 CREATION OF THE GALAXY PARENT SAMPLE

In this section, we first describe the motivation for the selection of the volume for LASr. Next, we require a galaxy parent sample highly complete in terms of galaxies sufficiently massive to host an AGN, which can then be used to select AGN from. We will see that current local galaxy samples do not fulfill this criterion so that we have to assemble our own galaxy parent sample. Finally, we describe the assembly of the galaxy properties relevant for this work, namely the coordinates, redshifts, and distances, allowing us to find the MIR counterparts of the galactic nuclei and compute their luminosities.

2.1 Selection of the volume

We wish to construct a highly complete census of SMBH growth in the local Universe. The choice of volume to be used for this purpose is motivated by several factors.

- In order to obtain a census that is representative for the whole AGN population, the volume needs to be representative of the larger scale, low redshift Universe. It is estimated that cosmological isotropy is reached for length scales of $\sim 200h^{-1}$ Mpc with $h = H_0/100\,\mathrm{km\,s^{-1}Mpc^{-1}}$ and H_0 the Hubble constant (Sarkar et al. 2019).
- The volume should also be large enough to sample rarer AGN sub-populations in sufficient numbers to yield statistically robust conclusions on their relevance. Here particular emphasis should be on the high luminosity AGN regime because these may dominate the integrated black hole growth and AGN feedback (e.g., Aird et al. 2010; Fabian 2012). However, high-luminosity AGN have a low space density. For example, current estimates of the AGN luminosity function in X-rays, e.g., Aird et al. (2015), let us expect a space density of $\sim 5 \times 10^{-7}\,\mathrm{Mpc^{-3}}$ for AGN with an intrinsic X-ray luminosity of $L^{\mathrm{int}}(2\text{-}10\,\mathrm{keV}) \geq 10^{44}\,\mathrm{erg\,s^{-1}}$, e.g., ~ 20 objects within a sphere of 200 Mpc radius.
- On the other hand, the volume should be small enough so that the depth of the all-sky surveys, used to identify and characterise the AGN, is sufficient to probe the lower parts of the AGN luminosity range. This is particularly important in the X-rays where extinction is large for obscured AGN. For example, the final all-sky maps of eROSITA and ART-XC are expected to have depths of $\sim 1.6 \cdot 10^{-13}\,\mathrm{erg\ cm^{-2}s^{-1}}$ and $\sim 3 \cdot 10^{-13}\,\mathrm{erg\ cm^{-2}s^{-1}}$ at 2-10 keV, respectively (Merloni et al. 2012; Pavlinsky et al. 2018), which corresponds to a distance of 150 – 250 Mpc for an observed X-ray luminosity of $L^{\mathrm{obs}}(2\text{-}10\,\mathrm{keV}) = 10^{42}\,\mathrm{erg\,s^{-1}}$. However, CT AGN are suppressed by easily a factor of 10 to $\sim$ 100 at these wavelengths.
- The MIR is much less affected by extinction, but sensitivity is the key restricting factor. I.e., the *WISE* all-sky maps have an average depth capable of detecting an AGN with a 12 μm luminosity $L^{\mathrm{nuc}}(12\,\mu\mathrm{m}) = 10^{42}\,\mathrm{erg\,s^{-1}}$ up to a distance of 220 Mpc with $\geq 3\sigma$ in band 3 (W3$\sim$ 11.6 mag; *WISE* documentation[1]).
- Another factor to take into account is that the completeness of our parent sample of galaxies directly restricts the completeness of our AGN search. According to a recent estimate, our all-sky redshift completeness is only 78% for galaxies with a redshift $z < 0.03$ (Kulkarni et al. 2018), and the completeness is quickly dropping towards higher redshifts.

[1] http://wise2.ipac.caltech.edu/docs/release/allsky/

- Finally, once identified, we need to follow-up and characterise all the AGN in the volume. We are especially interested in spatially resolving the in and outflows on sub-kiloparsec scales for as many objects as possible, which puts a feasibility-based upper limit on the volume. For example, at an object distance of 250 Mpc, one kiloparsec corresponds to one arcsec on sky, which is close to the effective resolution limit of most telescopes.

The above factors advocate to implement LASr as an all-sky survey with a spherical volume given by a radius between ∼ 100 Mpc and ∼ 250 Mpc. While, we plan to later use the larger value, 250 Mpc, we start LASr first with the lower value, 100 Mpc, to verify our approach. Using the cosmological parameters of Collaboration et al. (2016), an object distance of 100 Mpc corresponds to a redshift of $z = 0.0222$.

2.2 On the 2MRS galaxy sample

The current, commonly used reference sample for the local galaxy population is based on the the Two Micron All Sky Survey (2MASS; Skrutskie et al. 2006), namely the 2MASS Redshift Survey (2MRS; Huchra et al. 2012). It contains 45k galaxies which were selected from the 2MASS Extended Source Catalog (XSC) and the 2MASS Large Galaxy Atlas (LGA; Jarrett et al. 2003) according to the following criteria, a) detected in the K-band with $\mathrm{K_S} \leq 11.75$ mag; b) low foreground extinction with $E(B-V) < 1.0$ mag; and c) sufficiently far from the Milky Way plane with $|b| > 5°$ for $30° < l < 330°$ and $|b| > 8°$ otherwise with l and b being the Galactic longitude and latitude, respectively. For ∼ 98% of the objects, redshifts were collected from the literature or dedicated follow-up observations by Huchra et al. (2012), so that the final galaxy sample with redshifts comprises 43.5k galaxies. Out of those, 15k galaxies are within 100 Mpc distance from us, to which we refer to simply as the "2MRS sample" in the following.

So far, it has been assumed that the 2MRS sample contains all major galaxies, at least outside of the Galactic plane. However, 13% of the host galaxies of the 191 B70 AGN within $D < 100$ Mpc are not part of the 2MRS. This fraction increases to 26% for $D < 250$ Mpc. Since we aim at a final completeness of > 90% for AGN-hosting galaxies, we have to complement the 2MRS sample (next section). The necessity of this extension of the 2MRS is further discussed in Sect. 3.1.

2.3 The LASr-GPS

In order to build our parent sample of galaxies for LASr, hereafter LASr-GPS, we combine the 2MRS with galaxies from the major public astronomical databases. Namely, the LASr-GPS is created by querying the December 2018 release of the NASA/IPAC Extragalactic Database (NED[2]), the May 2018 release of the Centre de Données astronomiques de Strasbourg (CDS) Set of Identifications, Measurements and Bibliography for Astronomical Data (SIMBAD[3]; Wenger et al. 2000), and the most recent, i.e., 15th, data release of the Sloan Digital Sky Survey (SDSS[4]; Blanton et al. 2017; Aguado et al. 2019) for all objects within the redshift limit.

A multi-stage cleaning process is necessary with iterations before and after merging of these different subsets to remove duplications, spurious redshifts and other contaminants in order to obtain a clean galaxy sample. The full assembly process is illustrated in Fig. 1. Its order is partly dictated by practical aspects in the selection process.

In short, we first exclude all objects classified as stars if they have a redshift $z < 0.001$ as well as objects with unreliable or photometric redshifts (step 1 in Fig. 1), yielding 157k, 60k, and 22k from NED, SIMBAD and SDSS respectively. We crossmatch these subsets in step 2, unifying all matches within a cone of 3 arcsec radius[5]. Not for all objects a counterpart is found in every subset. However, many of these objects actually have entries in NED, SIMBAD or SDSS but either without assigned redshift or are classified as stars in that database. Thus, they were not selected in step 1. In order to gather as much information as possible about each object, we therefore query for all still missing counterparts in the corresponding databases (step 3). These steps yield 183k potential galaxies.

Next, we identify all known AGN within these potential galaxies by crossmatching with all major literature samples of AGN (step 4; see Sect. 2.4 for details)[6]. In the next steps, 5 and 6, we first add the NED compiled redshifts and redshift-independent distances (NED-D; Steer et al. 2017) and then use the added information from all the crossmatching to perform another cleaning of Galactic objects. This is necessary because many objects are unclassified (or even erroneously classified as galaxies) in some of the databases but then identified as Galactic objects in others. Most of these contaminants result from previous SDSS data releases included in NED and SIMBAD. Those contaminants we can now eliminate by using the most recent and improved classifications of SDSS DR15. Specifically, we exclude all objects which have either (i) at least one classification as Galactic object but none as galaxy in NED, SIMBAD and SDSS (63k cases); (ii) at least two classifications as Galactic objects (4.8k cases); (iii) at least one classification as Galactic object and a redshift < 0.0011 (20k cases); or (iv) no classification as galaxy and a redshift < 0.0011 (18k cases). This redshift threshold is determined from SDSS DR15 with the probability of being a genuine galaxy being < 1% for all redshifts lower than that. We make sure to keep all 2MRS galaxies during this step and check all doubtful cases individually to make sure that we do not erroneously exclude any genuine galaxy. As a result of this cleaning, the sample is further reduced to 77k potential galaxies. Then, we perform crossmatching with *WISE* (step 7; see Sect. 2.7). During this step, we also check all objects visually and identify another 22k contaminants. These are either entries from NED and SIMBAD where no optical counterpart is identifiable in the vicinity of the given coordinates, or cases where the coordinates point to a part of another galaxy in the sample. The reason for the latter can be inaccurate coordinates in NED and SIMBAD or multiple fibers placed on different parts of larger galaxies in SDSS. This step is also used to correct coordinates of galaxies that are offset from its nucleus, or geometric centre (if the nucleus is unidentifiable). The final two steps (8 and 9) clean the remaining duplicates, e.g., objects sharing the same *WISE* counterpart, as well as objects with erroneous redshifts (see Sect. 2.6).

The final galaxy sample contains 49k visually verified galaxies and includes all but 3 of the 15k 2MRS galaxies in the volume[7].

[2] http://ned.ipac.caltech.edu/
[3] http://simbad.u-strasbg.fr/simbad/
[4] https://www.sdss.org

[5] The radius is chosen to be well below the angular resolution of *WISE* and prevent incorrect matches.
[6] This is done at this early stage to ensure we are not losing any relevant objects in the following steps.
[7] The excluded are: NGC 6822 aka 2MASX J19445619-1447512 is a very nearby dwarf galaxy which is over-resolved in *WISE* and 2MASS and

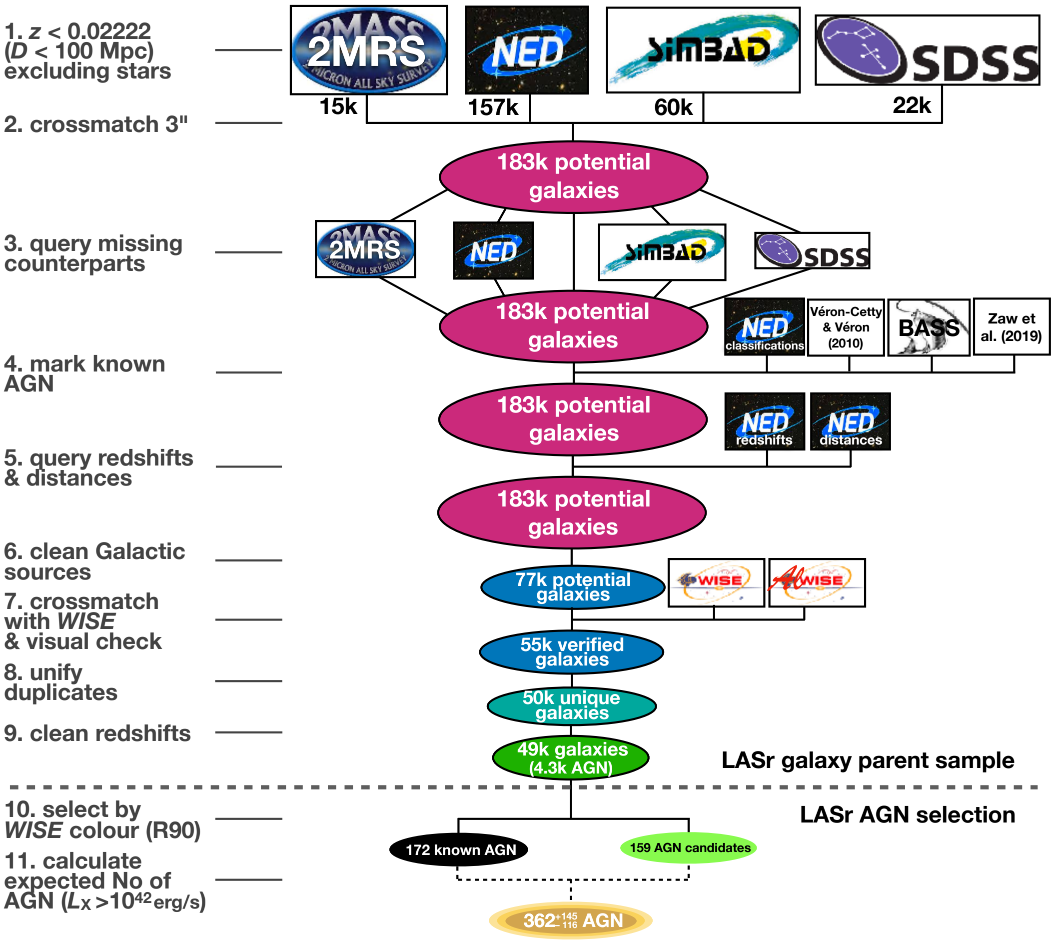

Figure 1. Schematic recipe for assembly of the LASr-GPS and following AGN selection. It starts at the top with the numbers of potential galaxies within the redshift limit found in the different databases 2MRS, NED, SIMBAD and SDSS. These are then merged into one sample of potential galaxies which is then cleaned and further information added in a number of steps, proceeding to the bottom, until the final parent sample of 49k verified galaxies, the LASr-GPS, is reached after step 9. See Sect. 2.3 for a detailed description of each step in the LASr-GPS assembly, while the AGN selection that follows below the dashed line in steps 10 and 11 is described in Sect. 4.3 for the known AGN, Sect. 4.4 for the new candidates, and Sect. 4.6 total AGN number estimate.

Therefore, the LASr-GPS can indeed be seen as an extension of the 2MRS, and all the following steps performed with the LASr-GPS apply in equal measure to the 2MRS, unless mentioned otherwise. The galaxies are listed in Table 1 which is available in its entirety online. The LASr-GPS forms the parent sample for searching local AGN.

2.4 Identification of known AGN

In our quest for a highly complete AGN sample, we benefit from the large amount of literature that already identified many of the AGN in our volume. NED and SIMBAD have collected a lot of these classifications which we obtained together with the object queries. In addition, for NED, we query the website of each individual object to extract the homogenized activity class as well as the basic description ("classifications") that also often contains information about any AGN in the system. This results in 2617 AGN classifications from NED and 4398 from SIMBAD. SDSS also provides AGN identifications based on an automatic assignment from the template fitting to the optical spectra, resulting in 271 automatic AGN classifications among the SDSS galaxies.

We complement these classifications with the two largest independent AGN collections, namely Véron-Cetty & Véron (2010) and Zaw et al. (2019). The former authors have collected 169k AGN from the literature of which 1135 are in our volume, while the latter have analysed all available optical spectra of the 2MRS galaxies, resulting in 8.5k AGN identifications of which 3078 are in our volume. Finally, we add the new AGN identifications of the 191 B70 AGN within our volume.

In total, this leads to 4309 known AGN among the 49k galaxies of the LASr-GPS, of which 3887 are also in the 2MRS sample. Most of these have been identified using optical spectroscopic classifications. We adopt optical AGN type classifications whenever they are available in the databases. In addition, for the narrow-line AGN from Zaw et al. (2019), we perform the Seyfert, LINER (low-ionization nuclear emission-line region) and H II nucleus classification based on the emission line fluxes published in that work and the AGN diagnostics of Kewley et al. (2006).

thus can not be included. 2MASX J18324515-4131253 is actually part of ESO 336-3. which is also in 2MRS, and, thus, it is excluded. 2MFGC 02101 is most likely a foreground star in the outskirts of NGC 1035 which is also in the 2MRS.

This way, we could retrieve optical type classifications for 95% (4101 of 4309) of the known AGN including 2409 Seyfert , 2053 LINER and 1777 H II classifications[8]. Here, we allow for multiple classifications of the same object[9] which is the case for 47% of the AGN and to a large part the likely result of varying spectroscopic aperture, data quality and classification methods used. In addition, some of the AGN identifications might be unreliable, in particular if the object has not been optically classified as Seyfert (1900 objects). Most of the latter are optically classified as LINERs which is a controversial class with respect to its AGN nature because also stellar phenomena can produce similar emission line ratios (e.g., StasiÅĎska et al. 2008; Cid Fernandes et al. 2010, 2011; Yan & Blanton 2012; Belfiore et al. 2016; Hsieh et al. 2017). These caveats have to be taken into account when using this compilation of classifications, and, in this work, we use them only for indicative purposes. The same applies to the more detailed Seyfert obscuration type classifications, where we find 1012 objects classified as type 1 (Sy 1.x) and 1545 as type 2 (Sy 2) with 9% (219) of the objects having both classifications or intermediate type (Sy 1.8 or Sy 1.9). If we exclude all objects with multiple optical classifications, 490 type 1 and 475 type 2 AGN remain.

The known AGN are marked as such in Table 1 and their characteristics are further discussed in Sect. 4.1.

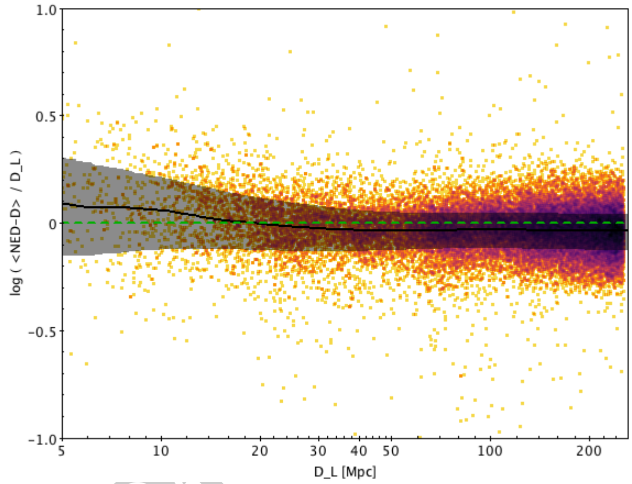

Figure 2. Distribution of the logarithmic ratio of the median NED-D redshift-independent distance and the luminosity distance, D_L, of each object as a function of D_L. The colour scaling marks the density of the data points from yellow to black. The black line indicates the median value at a given D_L with a width of 2 Mpc, while the grey shaded area encompasses 2/3 of the population at each D_L. The green dashed line marks the 1 to 1 correspondence.

2.5 Identification of known starbursts

Not only AGN can produce significant MIR emission but also intense star formation does. Therefore, starbursts are the main source of contamination for AGN selection in the MIR (e.g., Hainline et al. 2016). In order to understand the effects of starbursts on the MIR appearance of galaxies, we also collect galaxies explicitly classified as starbursts in either of the databases, resulting in 4006 starbursts, mostly from SDSS (3762 objects). Similar to the known AGN, the starburst sample is probably highly incomplete, but it shall serve us to understand the locus of starburst galaxies in the different parameter distributions in comparison to the AGN. The corresponding objects are marked as well in Table 1.

2.6 Determination of redshifts & distances

The most fundamental quantity that we require for each galaxy is its distance from us, not only to decide whether the galaxy is within our volume but also to determine its luminosity. For most galaxies, the distance is estimated from the redshift for which we generally prefer the value provided by SDSS DR15, or NED if the former is not available. We consider a redshift robust if we either have a robust value in SDSS DR15 (their redshift confidence flag = 0), or we have at least two independent redshift measurements from all databases combined (including the redshift compilations in NED). Otherwise, we consider the redshift somewhat uncertain and use a redshift confidence flag in Table 1 to mark these cases with a value of 1 (0.5% of the LASr-GPS), meaning that these values are not verified but there is no suspicion of a problem either. In addition, there are several cases where the different redshift measurements are discrepant (standard deviation of measurements > 20%; 4.6% of all galaxies). In most of these cases, only one of the redshift measurements for the affected object is offset from the rest, often by a factor of two or more. In particular for the very nearby galaxies, we can thus often guess the "right" redshift from the visual size of the galaxy. For objects with discrepant redshifts, where we can not make a clear decision based on all available information, we assign a value of 2 to the redshift confidence flag (0.3% of the LASr-GPS), meaning that those redshifts are controversial and can not be trusted. Therefore, we have robust redshifts for 99.2% of the galaxies.

With the redshifts, we compute the luminosity distance, D_L, for all galaxies. However, in the nearby Universe D_L can be inaccurate owing to the speed of the Hubble flow here being comparable to the peculiar motion of the galaxies. Fortunately, a major effort of NED led to a large collection of 320k redshift-independent distance estimates for 182k galaxies dubbed NED-D (Steer et al. 2017).

Of our 49k galaxies, NED-D values are available for 10.6k galaxies. NED-D contains multiple measurements of very different methods for many galaxies, leading to a very heterogeneous data set. Unfortunately, it is not feasible here to perform a selection or weighting of different methods for each galaxy. Instead, we simply compute the median of the different measurements. Before adopting the NED-D values, we first compare them to our D_L values in Fig. 2. As expected, we see that the deviation between NED-D and D_L increases for small distances, while for larger distances the median ratio between the two converges to a constant value close to 1. This happens roughly at D_L = 50 Mpc. Here, also the width of the scatter converges to 0.16 dex (factor 1.44), indicating that above this value the scatter between the individual redshift-independent methods dominates over deviations from the Hubble Flow. This motivates us to adopt the median NED-D value for the object distance if D_L < 50 Mpc (4.6k galaxies; 9.3%). Otherwise we use D_L. The resulting final redshifts and distances used are listed in Table 1.

[8] The remaining 208 objects are simply classified as "AGN" in the databases without any optical type given.

[9] There are 402 objects classified both as Seyfert and LINER, 993 as Seyfert and H II and 846 as LINER and H II.

2.7 Identification of WISE counterparts

For the planned identification of AGN, we require the MIR properties of all the galaxies. Therefore, we crossmatch our galaxy samples with the all-sky pointsource catalogues of *WISE*, specifically, the AllWISE catalogue (Cutri & et al. 2013), and then visually verify the counterpart most likely corresponding to the nucleus of the galaxy. In 93.3% of the cases, this is the AllWISE source that is closest to the galaxy coordinates. The median angular separation is 0.6 arcsec and the 90th percentile is 2.7 arcsec. The large majority of the remaining 6.7% are caused by inaccurate galaxy coordinates in the databases, which we clean manually. Furthermore, for many small, late-type or disturbed galaxies, no nucleus can be robustly identified. This is the case for 4% of the LASr-GPS and 0.2% of the 2MRS sample. We mark these galaxies with a corresponding warning flag in Table 1. In these cases, we choose either the source closest to the approximate apparent geometric centre, or we take the brightest MIR emission knot overlapping with the optical counterpart (whichever seems more applicable). Fortunately, these cases are predominantly small galaxies, which are the least relevant for our AGN search. Furthermore, in 0.6% of the galaxies, the AllWISE catalogue failed to capture the nucleus for unknown reasons. For those, we fall back to the original data release catalogue (Cutri & et al. 2012), which delivered a better counterpart in all cases. This strategy allows us to allocate a *WISE* counterpart to almost every object that is not rejected in any of the sample cleaning steps and iterations so that our final *WISE* coverage is 99.94%.

However, we found that in 1.4% of the galaxies, a nearby brighter source actually dominates the *WISE* emission. In those cases, the MIR emission of the latter is taken as upper limit for the fainter object.

Finally there are five cases[10] where the angular separation of two galactic nuclei was too small to be picked up as individual sources in the *WISE* catalogues. They are treated as one object, i.e., late-stage galaxy merger, in the following.

2.8 Computation of MIR colours and luminosities

After having identified the most likely *WISE* counterparts, we can now estimate the MIR emission of the galactic nuclei. The majority (67%) of the galaxies are resolved in *WISE*, and, thus, their total MIR emission is not well captured in either of the *WISE* catalogues (see, e.g., Cluver et al. 2014). However, since here we are mostly interested in the nuclear MIR emission we use the profile-fitting magnitudes in AllWISE, which roughly capture, and certainly not underestimate, the nuclear emission. This was verified for nearby AGN by, e.g., Ichikawa et al. (2017) through comparison with high angular resolution MIR data. One might argue that the profile-fitting photometry is even superior for other purposes because it excludes most of the extended non-nuclear emission.

We calculate the observed central 3.4 μm and 12 μm luminosities, $L(W1)$ and $L(W3)$, for each galaxy using the best estimate distance determined in Sect. 2.6 and the assigned *WISE* band 1 and 3 magnitudes, *W1* ($\lambda = 3.4\,\mu$m) and *W3* ($\lambda = 11.56\,\mu$m), after first converting magnitudes to flux densities following the WISE documentation[11]. Owing to the low redshifts of our sources, no *K* corrections are required.

[10] 2MASX J09181316+5452324, AM 1333-254, IC 1623, IC 2554, VV 662

[11] http://wise2.ipac.caltech.edu/docs/release/allsky/expsup/sec4_4h.html

3 CHARACTERISATION OF THE PARENT SAMPLE OF GALAXIES

Before we study the AGN in our volume, we first compare the 2MRS and LASr-GPS and then address the completeness of the latter to better understand which limitations this might put on our subsequent AGN selection.

3.1 Comparison of galaxy samples

First, we examine the spatial distribution of the galaxy parent samples in different projections, namely the all-sky map (Fig. 3), the 2D projection onto the Galactic plane (Fig. 4) and the redshift distribution (Fig. 5). Most of the additional galaxies in the LASr-GPS compared to the 2MRS are in the Northern hemisphere (DEC> 0°), which is mostly owing to SDSS. This is visible also in Galactic coordinates (Fig. 3), where the core area of SDSS is in the Galactic North ($b > 30°$). In addition, both the LASr-GPS and 2MRS are clearly missing galaxies behind the Milky Way plane (we come back to that in Sect. 3.2). Otherwise, the distribution of the 2MRS galaxies in particular follows the cosmological filaments and galaxy clusters contained in our volume (Fig. 3). This is also visible in the Galactic plane projection (Fig. 4), although to a lesser degree probably owing to the collapse of the latitude dimension and the proper motions of the galaxies. The latter can affect the redshift-based luminosity distances and, this way, artificially spread the filaments and clusters in radial direction (e.g., Centaurus, labelled in the figure). Both sky projections indicate that our galaxy samples probe more or less well the cosmological structure of matter within the volume.

The redshift distribution (Fig. 5, left) illustrates that the number of galaxies in the LASr-GPS steeply rises with increasing distance up to the border of the volume. In addition, there is a dip in the redshift distribution around $z \sim 0.01$ ($D \sim 45$ Mpc) which is probably caused by the small scale anisotropy of the nearby Universe, namely voids to the Galactic East, North and West visible in Fig. 4.

The redshift distribution of the 2MRS sample, on the other hand, levels off at $z \sim 0.017$ and even decreases towards higher redshifts (Fig. 5, left). This indicates that already at 100 Mpc, the 2MRS starts missing galaxies owing to its *K*-band brightness cut. The comparable shallowness of 2MRS with respect to the LASr-GPS is also visible in the *WISE* central *W1* magnitude and luminosity distributions (Fig. 5, middle and right), as well as in the *W1* luminosity over redshift distribution (Fig. 6). The latter plot shows that the LASr-GPS probes the galaxy population down to central luminosities of $L(W1) \sim 10^{41}$ erg/s at a distance of 100 Mpc, while the 2MRS has a depth of $L(W1) \sim 10^{42.5}$ erg/s. The median central *W1* luminosity compared to the LASr-GPS and SDSS are also significantly higher for the 2MRS (by 1 dex and 1.4 dex, respectively). Similar trends apply as well to the other *WISE* bands, just at higher magnitudes and lower luminosities (thus not shown here).

Interestingly, there are, however, also a significant number of galaxies well within the 2MRS brightness range but missing from 2MRS, as can be seen best in Fig. 5, middle and right. Are all these galaxies situated in the Galactic plane?

To investigate this further, we examine how the galaxy number ratio of 2MRS over LASr-GPS evolves with luminosity in Fig. 7. In the low luminosity regime, the galaxy ratio is $\sim$ 30%, while for $L(W1) \gtrsim 10^{41}\,\mathrm{erg\,s^{-1}}$, it starts to rise, surpassing 90% at $L(W1) > 10^{42.6}\,\mathrm{erg\,s^{-1}}$ and finally reaching the maximum value of 96% at $L(W1) > 10^{42.9}\,\mathrm{erg\,s^{-1}}$. The latter numbers are for exclud-

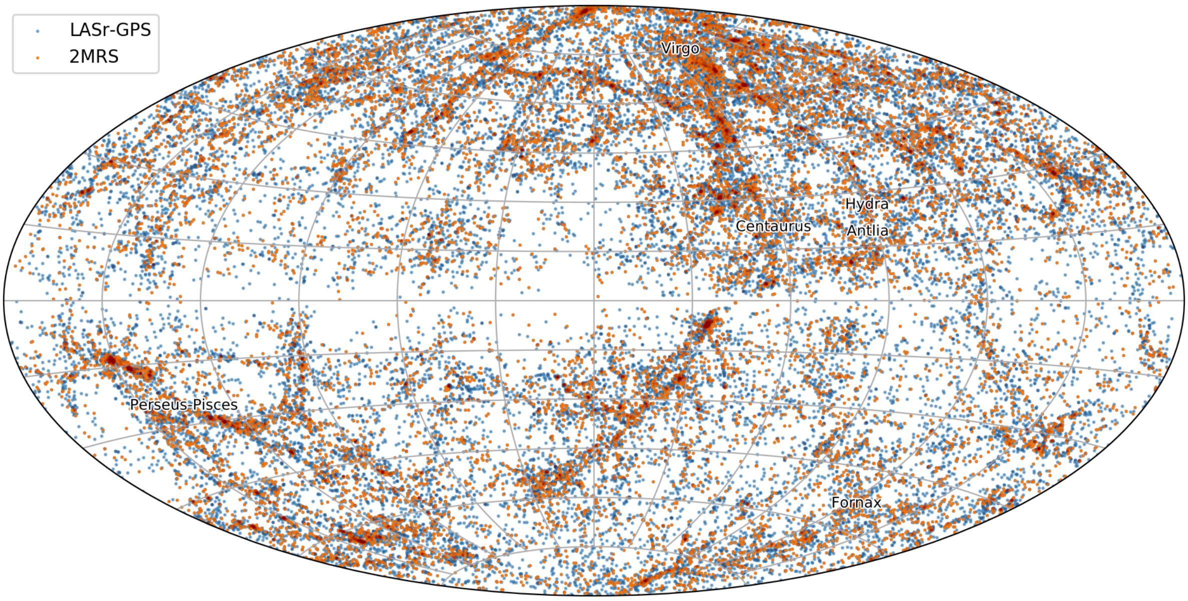

Figure 3. Aitoff projection of the Galactic coordinate distributions of all galaxies within the redshift limit from the 2MRS (orange) and LASr-GPS (blue). Darker colours mark areas of overdensity in linear scale, mostly marking the cosmic filaments within the volume. The center lines of the plot mark Galactic longitude $l = 0\,\mathrm{h}$ and Galactic latitude $b = 0°$, respectively. Some nearby galaxy clusters are labelled.

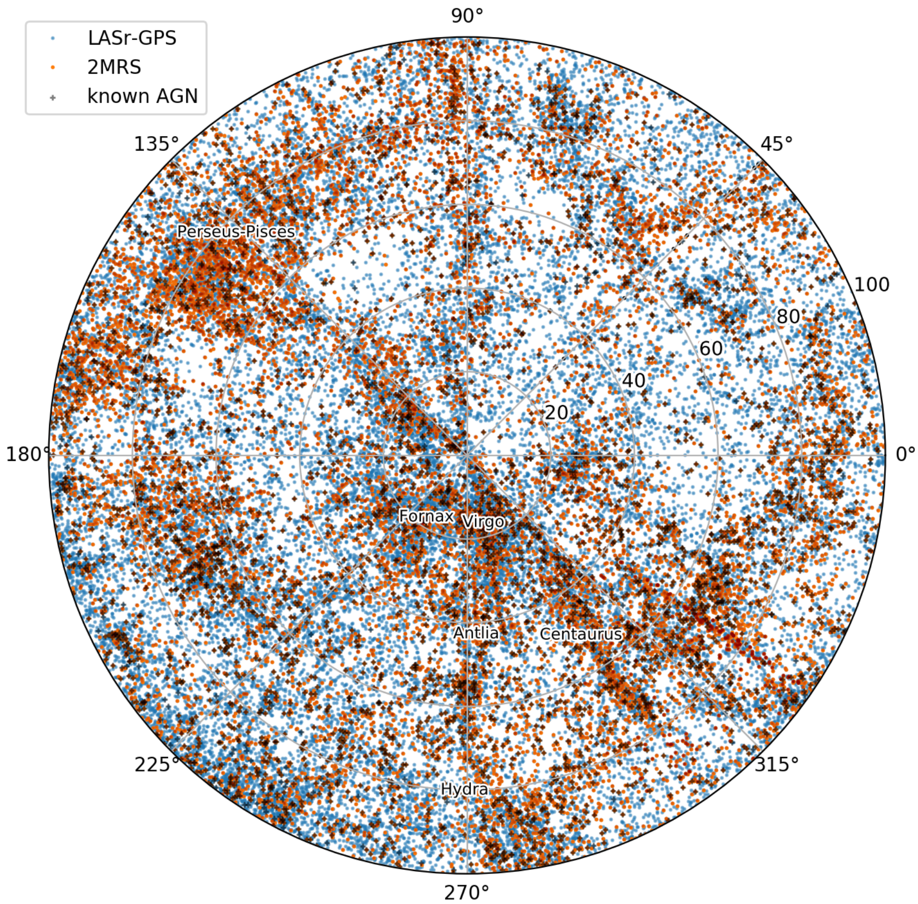

Figure 4. 2D projection of the distributions of all galaxies into the Galactic longitude plane within the redshift limit from the 2MRS (orange) and LASr-GPS (blue). Darker colours mark areas of overdensity in linear scale. Semi-transparent black crosses mark known AGN. The radial axis states the radial object distance in Mpc. Some nearby galaxy clusters are labelled.

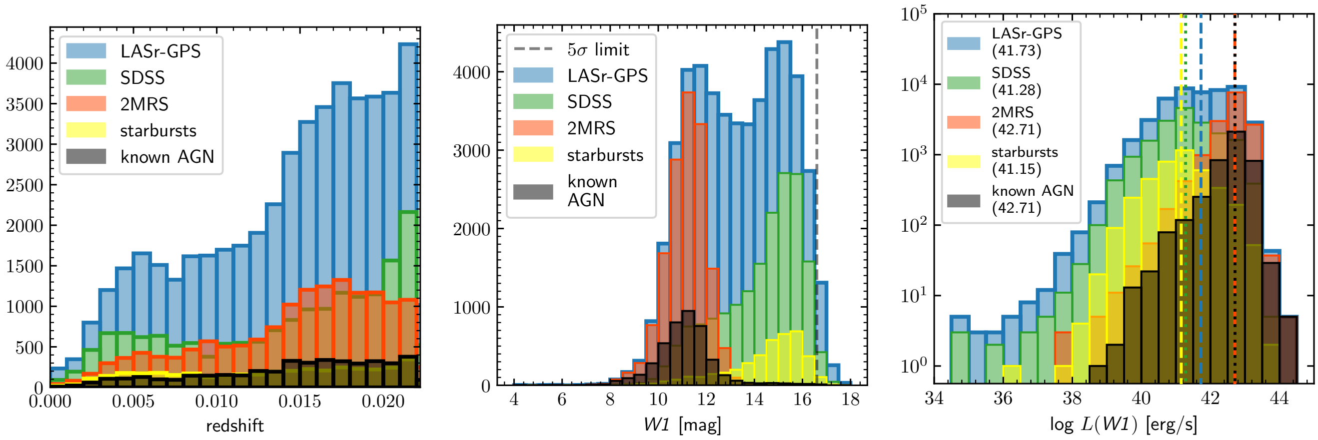

Figure 5. Redshift (left), *WISE* central *W1* magnitude (middle) and luminosity (right) distributions of all galaxies from the 2MRS (orange) and LASr-GPS (blue). For comparison, also the distribution of sources in SDSS DR15 is shown (green). The distribution of known starbursts is shown in yellow, while known AGN are shown in black. In addition, the middle plot shows the nominal 5σ depth of the AllWISE catalog as grey dashed line, while the right plot shows the median luminosities for each subsample as vertical dashed, dotted and dash-dotted lines of the corresponding colour.

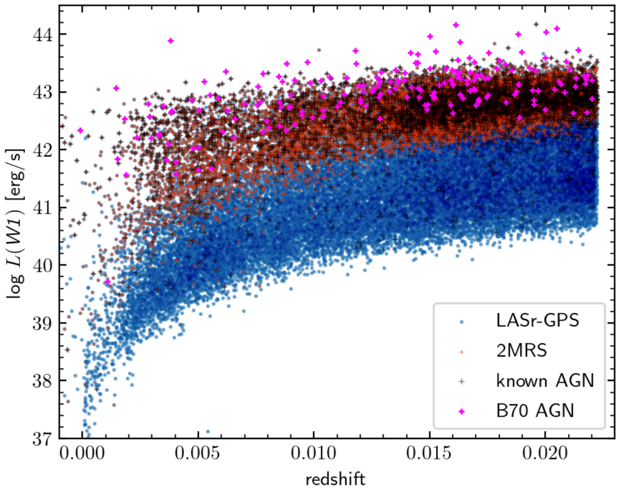

Figure 6. Central *WISE W1* luminosity over redshift for all galaxies from the 2MRS (orange) and LASr-GPS (blue). Semi-transparent black crosses mark known AGN, while magenta crosses mark B70 AGN.

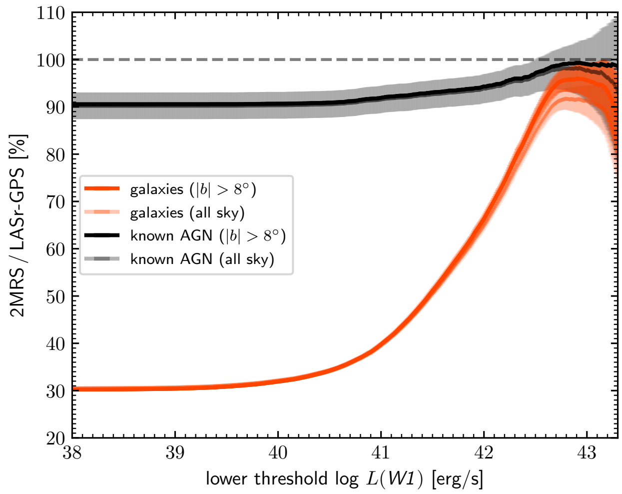

Figure 7. Galaxy and known AGN number ratios of 2MRS to LASr-GPS over a lower central *W1* luminosity limit (orange lines). The dark orange coloured line marks the galaxy ratio outside the Galactic plane, $|b| > 8°$, while the light orange coloured line shows the galaxy ratio for the whole sky. Furthermore, the black (grey) line shows the known AGN ratio outside the Galactic plane, $|b| > 8°$ (for the whole sky).

ing the Galactic plane as defined for the 2MRS sample selection ($|b| > 8°$). If, we compare the 2MRS to LASr-GPS ratio over the whole sky, the maximum 2MRS fraction drops to 91.6%, reached at the same $L(W1)$. We can also look at the ratio of known AGN in 2MRS over LASr-GPS (also shown in Fig. 7). Here, the minimum fraction is relatively high at 90% already for low luminosity thresholds, i.e., 90% of known AGN host galaxies are in the 2MRS. However, the ratio reaches its maximum of 99.1% only at $L(W1) > 10^{42.9}$ erg s^{-1}.

In conclusion, even outside the Galactic plane, the completeness of the 2MRS sample peaks only at $L(W1) > 10^{42.9}$ erg s^{-1}, which is well within the AGN regime, e.g., the B70 AGN host galaxies have a median of $L(W1) = 10^{43}$ erg s^{-1}. This explains why the 2MRS is missing a significant fraction of B70 host galaxies and thus probably of the whole local AGN population, which justifies our extension to the LASr-GPS to maximise completeness.

3.2 Completeness of LASr-GPS

In the previous section, we have shown that the LASr-GPS provides a higher completeness in terms of potentially AGN hosting galaxies compared to the 2MRS sample. However, how complete and deep is the LASr-GPS in absolute terms?

Optimally, one would want to express this depth in the physical galaxy property of total stellar mass. However, here we simply use the unresolved *WISE* emission which is missing significant stellar light depending on the galaxy size and distance. Furthermore, the mass-to-light ratio is not constant but depends on many galaxy parameters like galaxy type, metallicity and star formation rate and history (e.g., Wen et al. 2013 and discussion therein). Therefore, we refrain here from attempting stellar mass estimates but rather

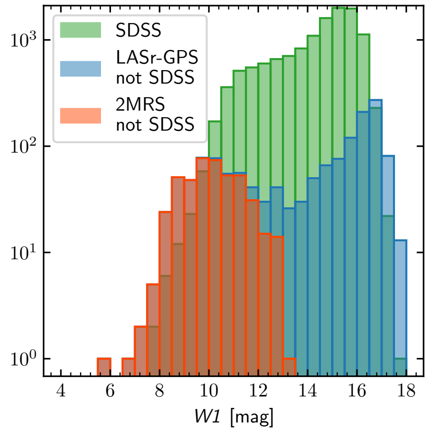

Figure 8. *W1* distribution of galaxies within the SDSS spectroscopic core area. Galaxies with SDSS spectra are shown in green, galaxies without but part of the LASr-GPS are shown in blue, and 2MRS galaxies without SDSS spectra in that area are shown in orange.

express the sample depth simply in the central *W1* luminosity. For most galaxies, this quantity is probably dominated by the stellar bulge.

In Fig. 6, we already constrained the maximum depth of the LASr-GPS to be $\sim 10^{41}\,\mathrm{erg\,s^{-1}}$ at a distance of 100 Mpc. The actual achieved completeness above this luminosity is dictated by the redshift completeness in our case. Owing to the heterogeneous nature of the public databases, their completeness is difficult to assess, and this can only be done empirically. For example, Kulkarni et al. (2018) used a comparison of detected supernova events in galaxies with and without redshifts in NED to estimate the redshift completeness of the latter database to be $\sim 78\%$ within a redshift of $z < 0.03$. This value provides a lower limit for our LASr-GPS, combining NED with other sources and being at lower redshift where completeness should be higher. It particular, we will try to derive more accurate estimates here based on comparisons with two highly complete galaxy surveys, one large-area survey (being representative of the volume), and one small-area survey (being very deep and highly complete).

3.2.1 Comparison with SDSS

The most powerful constraint for our redshift completeness is coming from the comparison to SDSS as reference for the highest available redshift completeness at reasonable depth and representative sky coverage. For simplicity, we here define the SDSS spectoscopic core area with simple cuts of $0° < \mathrm{DEC} < +60°$, 8:40 h (130°) < RA < 16:00 h (240°). This area comprises 13.2% of the sky and contains 12.7k galaxies selected by LASr-GPS with SDSS spectroscopy in DR15 and a redshift placing them within our volume. The average redshift completeness of SDSS is $\sim 90\%$ but decreasing towards brighter galaxies for technical reasons (Montero-Dorta & Prada 2009; Reid et al. 2016). Indeed, we find that there are an additional 1503 galaxies of the LASr-GPS within this area but without SDSS redshifts, implying that the SDSS completeness is at most 88%. As expected, these missing galaxies are bimodially distributed at the extremes of the galaxy brightness distribution (Fig. 8), whereas the bright peak is almost completely made up by 2MRS galaxies that are not in SDSS.

To mitigate the incompleteness of SDSS, we complement it

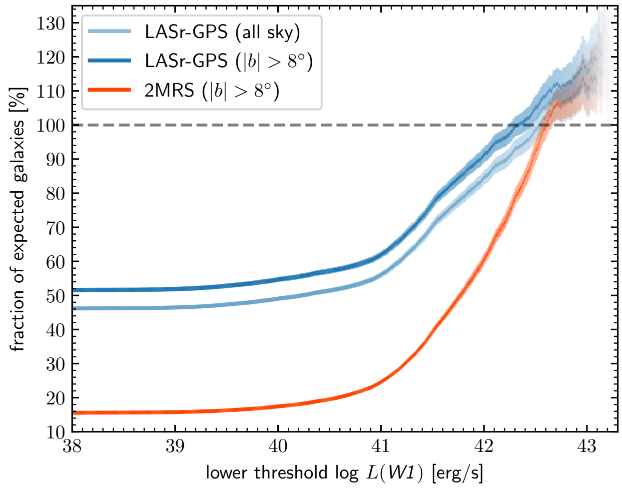

Figure 9. Fraction of expected galaxy included in the LASr-GPS, i.e., completeness of LASr-GPS, over a minimum central *W1* luminosity. The expected numbers are extrapolated from the SDSS core area (see main text for details). The solid coloured lines mark the fraction of galaxies away from the Galactic plane, $|b| > 25°$, for the LASr-GPS (blue) and the 2MRS sample (orange), whereas the semitransparent surface gives the 1σ uncertainty. The the lighter coloured blue line shows the same without excluding the Galactic plane. The grey dashed line marks the 100% completeness level.

with all galaxies from the 2MRS and LASr-GPS within the SDSS core area and assume that the result is 100% complete within this area down to $W1 \lesssim 17$ mag. Further assuming that the SDSS core area define above is representative of the whole sky, we can use the above galaxy sample to estimate the galaxy *W1* luminosity distribution for the whole sky within our volume. In Fig. 9, we examine how the fraction of expected galaxies that are in the LASr-GPS above a lower *W1* luminosity limit, i.e., the completeness, depends on that lower luminosity threshold. For $L(W1) \lesssim 10^{41}\,\mathrm{erg\,s^{-1}}$, the completeness is approximately constant between 50% and 60%, if we cut out the Milky Way plane ($|b| > 8°$), and $< 50\%$ otherwise. For higher $L(W1)$, the completeness outside the Milky Way plane rises and reaches 90% (100%) at $L(W1) = 10^{42}\,\mathrm{erg\,s^{-1}}$ ($10^{42.3}\,\mathrm{erg\,s^{-1}}$).

Maybe surprising, the observed to expected fraction continues rising above 100% at higher luminosities. We interpret this behaviour as the result of a possible under-density of such luminous galaxies in the SDSS spectroscopic core area, which could lead to such an effect given the decreasing number statistics at high luminosities and the relatively small fraction of the sky contained in that area. This would also explain why the observed to expected fraction for the whole sky as well reaches 100% despite the obvious undersampling in the Milky Way plane. Alternatively, this could imply that for galaxies with $L(W1) > 10^{42.5}\,\mathrm{erg\,s^{-1}}$, the under-sampled area does not contain a significant number of such luminous galaxies (13.9% of the sky for $|b| = 8°$). Finally, the 2MRS sample reaches 100% completeness at only $L(W1) > 10^{42.6}\,\mathrm{erg\,s^{-1}}$, excluding the Milky Way plane (also shown in Fig. 9).

3.2.2 Comparison with GAMA

To further assess the completeness of the LASr-GPS, we also compare to a smaller area survey than SDSS with higher depth and completeness like the Galaxy And Mass Assembly survey (GAMA;

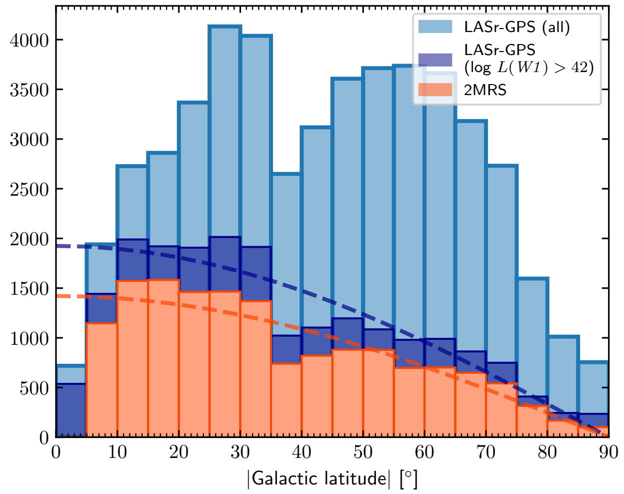

Figure 10. Absolute galactic latitude distribution of galaxies from the LASr-GPS (light blue) and the 2MRS sample (orange). The dark blue histogram marks galaxies from the LASr-GPS with $L(W1) > 10^{42}\,\mathrm{erg\,s^{-1}}$. The dashed lines mark fits of cosine shape to the corresponding distributions.

Liske et al. 2015). In particular, we use the two deep fields G12 and G15 from the latest release DR3[12] (Baldry et al. 2018). The two fields combined cover a sky area of $\sim$ 120 deg^2 with a redshift completeness of 98.5% for $r < 19.8$ mag (Liske et al. 2015). Combined, they contain almost 100k galaxies, of which 811 are within $D < 100$ Mpc. The release versions of NED and SIMBAD used here do not include the GAMA DR3, allowing us to use them to test the completeness of LASr-GPS in an independent way. For this, we cross-match the GAMA galaxies with the AllWISE catalogue, following the same method as throughout this work. This yields counterparts for 720 of the 811 GAMA galaxies (89%). Out of those, 68 have $L(W1) > 10^{42}\,\mathrm{erg\,s^{-1}}$. Based on the SDSS-based result we would expect at least 90% of them to be in the LASr-GPS. Indeed, 64 out of 68 , i.e., 94%, are also in the LASr-GPS, verifying our high completeness above this lower luminosity threshold.

3.2.3 *Galactic plane shadow*

The above results indicate that the LASr-GPS has a relatively high completeness for at least moderately luminous galaxies ($L(W1) > 10^{42}\,\mathrm{erg\,s^{-1}}$). However, this statement excludes one big source of incompleteness of course, the shadow of the Milky Way, which through a combination of densely clustered foreground emission sources, and high values of extinction makes it very difficult to identify and characterize galaxies that have sky coordinates close to the Galactic plane. To quantify this effect, we look at the absolute Galactic latitude distribution of galaxies (Fig. 10). If the galaxies were distributed fully randomly in the sky, then the latitude distribution should describe a cosine, which is approximately the case, at least for the 2MRS and the LASr-GPS, if restricted to galaxies with $L(W1) > 10^{42}\,\mathrm{erg\,s^{-1}}$. At low latitudes ($|b| \lesssim 20°$), the observed distributions fall short of the expectations owing to the Galactic plane shadow. In addition, the latitude distributions of all galaxy samples show a valley, i.e., an under-density between $35° \lesssim |b| \lesssim 45°$, caused by the voids in the local volume as already seen in the previous sky position and redshift distributions.

In order to quantify the Galactic plane shadowing, we fit a cosine functions to the bins with $|b| > 20°$ (shown as dashed lines in Fig. 10), and find the deficiency is 6.4 ± 0.8%, whereas the uncertainty is estimated from using different binnings for the latitude distributions. As expected, the 2MRS has a slightly higher missing fraction, owing to its latitude cut (7.4 ± 1.2%). The Milky Way foreground will always be a problem for the study of galaxies behind it. Therefore, is is probably easier to simply exclude this area from the volume when constructing samples for the AGN census in order to maximise completeness.

3.2.4 *Concluding remarks on completeness*

In the previous subsections, we addressed the completeness of the LASr-GPS empirically including the effect of the shadowing by the Galactic plane, leading to an all-sky completeness of 84% for $L(W1) > 10^{42}\,\mathrm{erg\,s^{-1}}$ and 96% for $L(W1) > 10^{42.3}\,\mathrm{erg\,s^{-1}}$). Outside the Galactic plane, we reach a completeness of at least 90% for central luminosities of $L(W1) > 10^{42}\,\mathrm{erg\,s^{-1}}$ and approximately 100% for $L(W1) > 10^{42.3}\,\mathrm{erg\,s^{-1}}$. These luminosities approximately correspond to stellar masses of $\log(M_*/M_\odot) \sim 9.4$ and 9.7, respectively, using the simple relation provided by Wen et al. (2013). But again one has to keep in mind that these values are missing significant amounts of stellar light for most galaxies including only their bulges.

We plan to further increase the redshift completeness of the LASr-GPS in future work. However, the above values mean that LASr can already now probe quite deep into the SMBH accretion regime, probing all galaxies where significant growth is occurring. By going to smaller volumes, we could decrease lower luminosity limits further. Although, at low luminosities, usually the stellar light by far dominates the total galaxy emission over the AGN, making it very difficult to isolate the AGN from its host. We will address this as well in future follow-up works where we will try to use more sensitive (but complex) AGN identification techniques. Here, we will utilize the simple but effective *WISE* colour selection as a first probe of the AGN activity within the volume.

4 STARTING THE AGN CENSUS

With the depth and completeness of the LASr-GPS characterised, we can now move on to identify and characterise the AGN population within our volume. We start with a brief summary of the already known AGN and then move on to the first AGN identificationn technique for LASr, namely *WISE* MIR colour selection. We estimate the efficiency of this technique and discuss possible limitations before applying it to the LASr-GPS to find new AGN candidates, in particular highly obscured and CT objects. Next, we discuss possible host contamination and provide prospects for detecting these new AGN with the current X-ray all-sky surveys. We conclude this section with an estimate of the total number AGN above a given luminosity limit within the volume, constraints on the CT fraction, and a comparison to luminosity functions from the literature.

4.1 Luminosity estimates for the known AGN

We know already from the collection of AGN identifications from the literature that there are at least 4.3k AGN within the volume

[12] http://www.gama-survey.org/dr3/

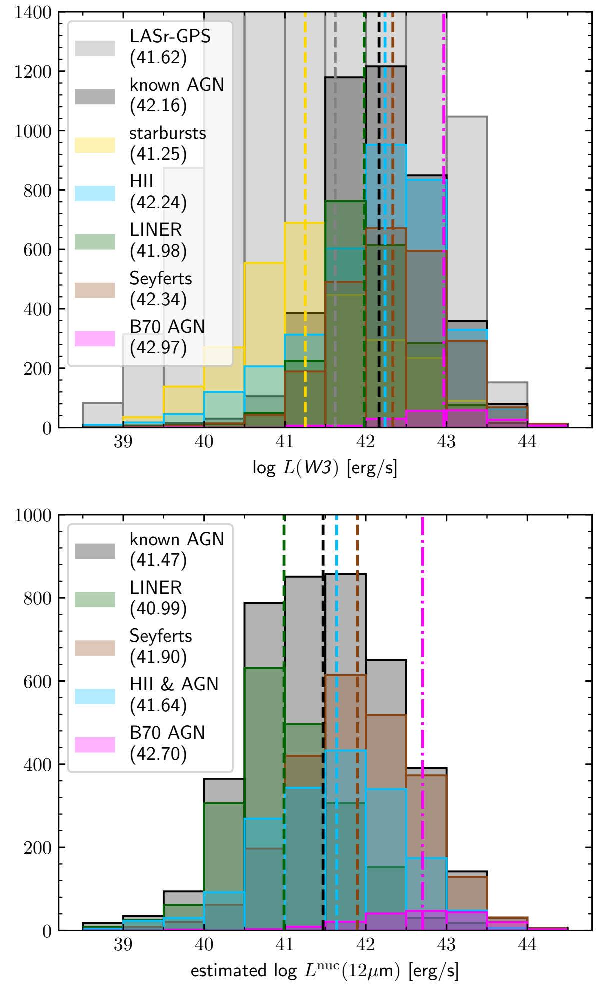

Figure 11. Top: *W3* luminosity distribution for different AGN and star-formation hosting galaxy populations within LASr-GPS, namely known AGN (black), starbursts (yellow), H II nuclei (blue), LINERs (green), Seyferts (brown) and B70 AGN (magenta). The distribution of the whole LASr-GPS is shown in grey in the background. The dashed lines of the corresponding colour mark the median value which is also shown in the legend. Bottom: Estimated $L^{\rm nuc}(12\,\mu{\rm m})$ distribution after decontamination of $L(W3)$ as described in Sect. 4.1.

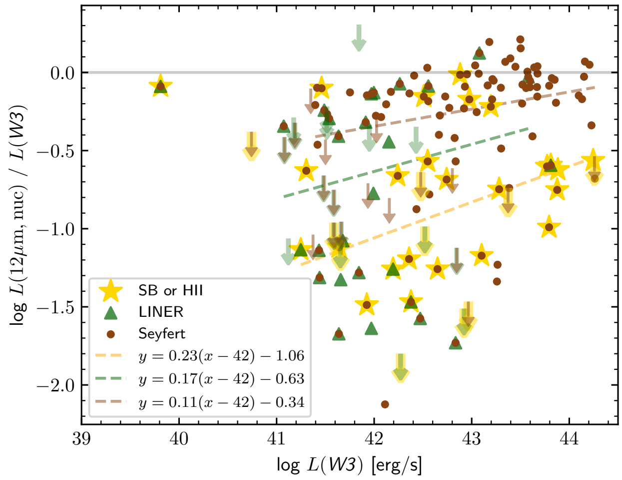

Figure 12. Logarithmic ratio of nuclear 12 μm luminosity, $L^{\rm nuc}(12\,\mu{\rm m})$ from Asmus et al. (2014) to profile-fitting *W3* luminosity, $L(W3)$, over $L(W3)$ for all 146 objects in common. Objects that are identified as star-forming in the literature (SB or HII) are marked with golden stars, while such with LINER classification have green triangle, and those with Seyfert classifications have brown dots. Objects can have several of these classifications in which cases the corresponding symbols are over-plotted. Nuclear 12 μm non-detections are marked by arrows of the corresponding colours. The light grey line marks the zero line, while the dashed lines provide linear fits to various sub-populations of detections, namely the dark-gray line for all objects only classified as Seyferts, the green line for Seyferts that also have LINER classification but not star-forming and in orange for all objects without Seyfert classification.

(Sect. 2.4). The redshift and brightness distributions of their host galaxies are shown in Fig. 5 and Fig. 6. In order to further characterise the AGN population, we can use the *W3* luminosities, tracing the 12 μm continuum of the AGN, dominated by warm ($\sim$ 300 K) AGN heated dust. Compared to the shorter bands, *W3* has the advantage of not being affected by stellar light. The *W3* luminosity distribution of known AGN is shown in Fig. 11, top panel. As expected, the majority of known AGN seem to be relatively low-luminosity, e.g., compared to the B70 AGN. However, we know that star formation can also significantly contribute to *W3* , in particular in large aperture measurements as used here[13].

Decoupling AGN and star formation emission in *W3* is a serious issue and requires detailed SED modelling, beyond the scope of this work. However, we can attempt at least a rough decontamination of the *W3* luminosities by computing statistical correction factors from the comparison of *W3* to high angular resolution measurements at the same wavelength. In particular, Asmus et al. (2014) presented a catalog of 253 nearby AGN with ground-based subarcsecond MIR photometry and estimated accurate estimates of the 12 μm AGN luminosity, $L^{\rm nuc}(12\,\mu{\rm m})$. We crossmatch our AGN sample with this catalog, finding 146 objects in common. In Fig. 12 we show the ratios of $L^{\rm nuc}(12\,\mu{\rm m})$ to the *W3* profile-fitting luminosity, $L(W3)$. While we already know from, e.g., Asmus et al. (2014) that the nuclear to large aperture 12 μm ratio is a strong function of the AGN luminosity, the same ratio shows only a weak increasing trend with increasing $L(W3)$ with a large scatter of 0.5 dex (Kendall's $\tau_{\rm K}$ = 0.25, null hypothesis probability log $p_{\rm K}$ = 4.1). On the other hand, we see that the ratio depends somewhat on the optical classification of the object with Seyferts having the highest and starbursts the lowest ratios. Therefore, we determine a $L(W3)$ to $L^{\rm nuc}(12\,\mu{\rm m})$ correction based on optical classification. Owing to the differing classifications in the literature, some of the objects are classified at the same time as Seyferts, LINERs, H II and/or starbursts (Sect. 2.4 and Sect. 2.5). Therefore, we test different groupings and find a distinction in the following three subgroups leading to the best corrections: a) pure Seyferts (no other classification), b) Seyferts also classified as LINERs[14] (but not as

[13] The relatively high luminosities of the H II nuclei confirms this statement. This does not apply to the systems classified as starbursts because many of them are compact dwarfs and, thus, do not reach such high luminosities.

[14] These probably correspond to objects situated in the Seyfert and LINER overlapping region in the BPT diagrams, i.e., Seyfert-LINER transition objects.

H II or starburst classification), and c) non-Seyferts (no classification as Seyfert). Corresponding ordinary least-square linear regression in logarithmic space with treating $L(W3)$ as the independent variable leads to the following corrections:

$$\log \frac{L^{\mathrm{nuc}}(12\,\mu\mathrm{m})}{L(W3)} = \begin{cases} 0.11(\log L(W3) - 42) - 0.34 & \text{pure Seyfert} \\ 0.17(\log L(W3) - 42) - 0.63 & \text{Sy-LINER} \\ 0.23(\log L(W3) - 42) - 1.06 & \text{non-Seyfert} \\ 0.18(\log L(W3) - 42) - 0.57 & \text{no classif.} \end{cases}$$

The last case provides the general correction if no optical classification is available. The 2/3-of-the-population scatter around these best fit lines is 0.22 dex, 0.57 dex, 0.23 dex and 0.43 dex, respectively. As said, this scatter is considerable and the above corrections should not be used for individual objects but only in a statistical sense.

Applying the above corrections to estimate $L^{\mathrm{nuc}}(12\,\mu\mathrm{m})$ for all known AGN, we obtain the following distribution shown in the bottom panel of Fig. 11. The estimated $L^{\mathrm{nuc}}(12\,\mu\mathrm{m})$ distribution for all known AGN is on average 0.7 dex lower than the one of $L(W3)$ with a median $L^{\mathrm{nuc}}(12\,\mu\mathrm{m})$ of $10^{41.47}$ erg s^{-1}. Only 18% (781) of the known AGN have $L^{\mathrm{nuc}}(12\,\mu\mathrm{m}) > 10^{42.3}$ erg s^{-1}, i.e., are at least moderately luminous. For Seyferts, this number increases to 30% (716 of 2385), while it is 68% for the B70 AGN (130 of 190). Again, these numbers should just provide a rough guidance for the luminosity ranges to be expected for the AGN in the volume. More accurate numbers will become available in the future based on SED decomposition and MIR follow-up observations.

4.2 MIR colours of AGN, galaxies and starbursts

Let us now examine the MIR colour distribution of the known AGN in the context of normal and starburst galaxies. The MIR colour distribution in the *W1*-*W2* over *W2*-*W3* plane is shown in Fig. 13 for all galaxies that are detected in the three *WISE* bands (76% of the LASr-GPS and 99.9% of the 2MRS samples), while the distributions of the individual colours are shown in Fig. 14. The large majority of galaxies, and in particular the 2MRS galaxies, form a relatively narrow star formation main sequence from blue to red *W2*-*W3* colours at almost constant *W1*-*W2* colour (as already previously found in the literature, e.g., Jarrett et al. 2019). This sequence is caused by star formation which leads to an increasing amount of warm dust emission and, thus, redder *W2*-*W3* colours with increasing star formation intensity relative to the direct stellar emission of the galaxy. For example, the bluest *W2*-*W3* objects are mostly passive, early-type galaxies like, e.g., NGC 548 at $W2 - W3 = 0.23$ mag and $W1 - W2 = -0.08$ mag. On the red side, the sequence is bending up to redder *W1*-*W2* colours of $W1 - W2 \sim 0.4$ mag at its approximate reddest end of $W2 - W3 \sim 5$ mag. One of the most extreme objects here is the starbursting NGC 1808 ($W2 - W3 = 0.43$ mag; $W1 - W2 = 4.98$ mag). In addition, the galaxy distribution of the LASr-GPS extends to redder *W1*-*W2* colours ($W1 - W2 \sim 0.3$ mag at intermediate *W2*-*W3* colours ($2 \lesssim W2 - W3 \lesssim 4$) filling up roughly the expected locus area of the spiral galaxies in Fig. 12 of Wright et al. (2010). Most of the galaxies are dwarfs according to their *W1* luminosity and optical appearance. The reason for the redder *W1*-*W2* colours is again star formation which can dominate *W2* if strong enough with respect to the stellar light of the host. This *W1*-*W2* reddening effect of star formation is the main source of contamination in AGN selections that are based on this colour, and will have to be taken into account (further discussed in Sect. 4.4.1).

Most of the galaxies known to host an AGN follow the *WISE* colour distributions of the 2MRS, i.e., rather massive galaxies. Only in *W2*-*W3* colour, they are slightly redder on median (2.66 mag vs. 2.42 mag), i.e., they either prefer star-forming hosts, or contribute themselves the most to this colour. Galaxies with hosting a luminous AGN, comparable MIR brightness at least in *W2*, have a redder *W1*-*W2* colour. They leave the main sequence and move upward in the colour–colour plane of Fig. 13 with increasing AGN luminosity. This trend motivates the colour selection based on *W1*-*W2* as discussed in the following.

4.3 Identification of AGN by MIR colour

We now proceed to the MIR colour-based identification of AGN and quantify how its efficiency depends on the AGN luminosity. Since the advent of the *WISE* mission, many MIR colour selection methods have been put forward to find AGN (e.g., Stern et al. 2012; Mateos et al. 2012; Assef et al. 2013). At the core, they are similar, building on the fact that the AGN-heated, warm dust emits significantly redder *W1*-*W2* colours than the light of the old stellar population in the host galaxy. In addition, the *W1*-*W2* is little affected by extinction, in particular at low redshifts (e.g., Stern et al. 2012), making *W1*-*W2* based AGN selection a formidable tool to select highly obscured and even CT AGN. Here, we will use the most recent and refined selection criterion introduced in Assef et al. (2018), namely one that was designed to have 90% reliability in selecting AGN (hereafter R90):

$$W1 - W2 > \begin{cases} 0.65 & \text{if } W2 < 13.86\,\text{mag}, \\ 0.65\exp[0.153(W2 - 13.86)^2] & \text{otherwise}, \end{cases}$$

The R90 criterion is illustrated in Fig. 15 for typical galaxy and AGN SEDs from Assef et al. (2010). This criterion works best for *W2* detections with a signal-to-noise greater than 5 (otherwise biases can occur; see Assef et al. 2018 for details[15]). All the 2MRS galaxies and 93% of the LASr-GPS are above this limit (99% for $L(W3) > 10^{41}$ erg s^{-1}).

The R90 criterion for $W2 < 13.86$ mag is shown as grey dashed line in Fig. 13. Out of the 4.3k known AGN in the volume, 172 fulfil the R90 criterion as visualized in that figure with larger symbols[16]. For 97% (167) of the 172 R90 AGN, optical type classifications are available, 97% (162) of which have a classification as Seyfert, while 9% (15) are classified as LINERs and 18% (29) as H II, i.e., 21% (34) have multiple classifications in the literature. The type 2 to type 1 ratio for the R90 AGN is 0.52 (similar as for the whole population of known AGN; Sect. 2.4) with a significant population with intermediate (Sy 1.8 or Sy 1.9) or both type 1 and 2 classifications (36%). Depending on their treatment, the type 2 fraction among the known AGN[17] is between 38 and 62%. The R90 AGN including their optical classifications are listed in Table 2.

As said, we expect the R90 criterion to preferentially select

[15] Normally, it is recommended to also remove objects for which the contamination and confusion flag in the AllWISE catalogue is set (cc_flags). However, here, to be inclusive, we keep such galaxies and examine them individually where necessary.

[16] Interestingly, only 83% of the corresponding galaxies are in the 2MRS, once more confirming the incompleteness of 2MRS in terms of AGN.

[17] The intrinsic type 2 fraction is probably higher because we expect the majority of AGN candidates to be obscured, i.e., type 2 (Sect. 4.4).

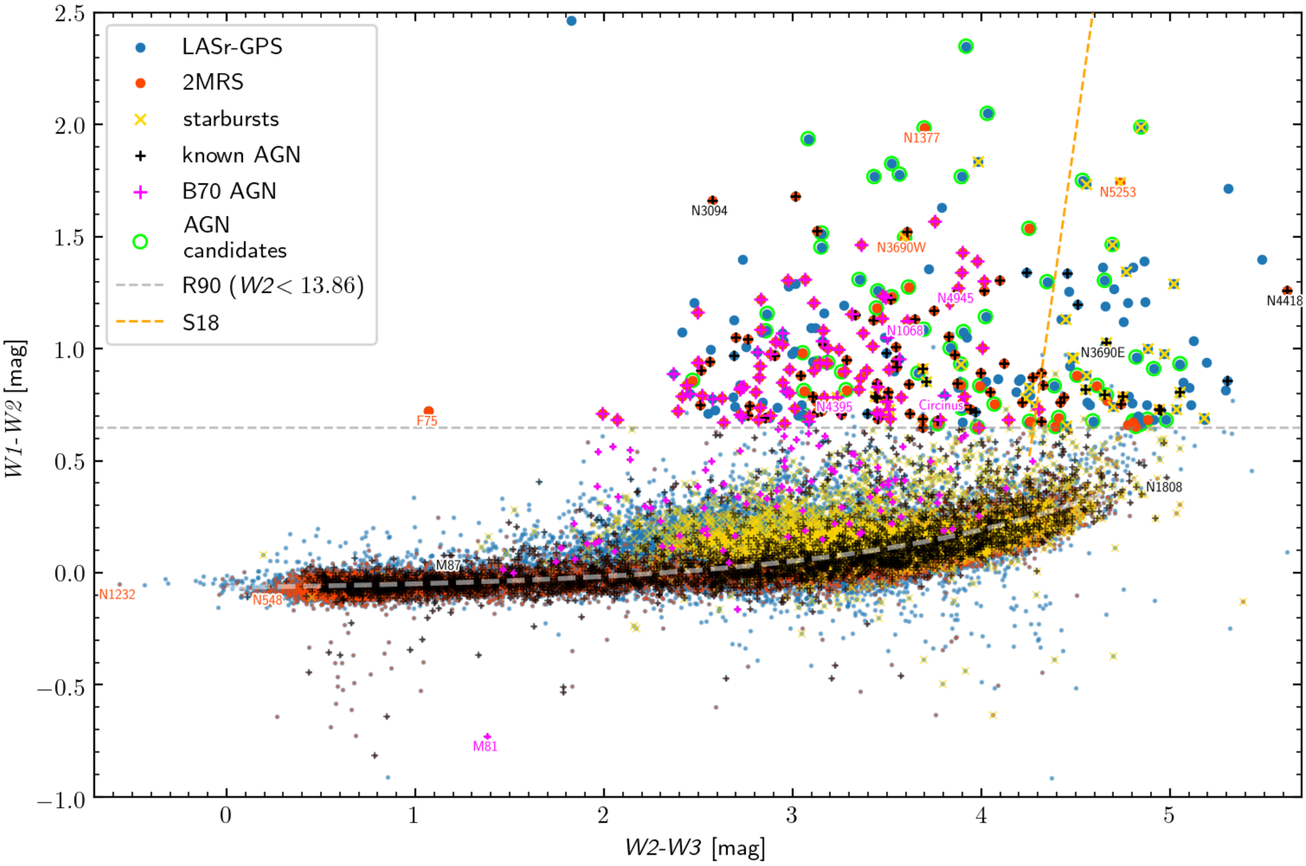

Figure 13. *W1-W2* versus *W2-W3* colour–colour distribution for all galaxies from the 2MRS (orange) and LASr-GPS (blue) detected in *W1*, *W2* and *W3*. Yellow 'X's mark starburst galaxies, while black crosses mark known AGN and magenta crosses mark B70 AGN. The R90 AGN colour selection criterion is shown as dashed, grey line (for $W2 < 13.86$ mag), and galaxies that fulfill R90 are marked with large symbols. In addition, the R90 AGN candidates with $L(W3) > 10^{42.3}$ erg s^{-1} have green circles. The theoretical AGN/extreme-starburst discriminator line from Satyapal, Abel & Secrest (2018) is shown as dashed orange line (AGN left, starbursts right). The star formation main sequence line from Jarret et al. (2019) is shown as white dashed line. Some notable galaxies are labelled with short names ("M" stands for Messier, "N" for NGC, and "F" for Fairall.

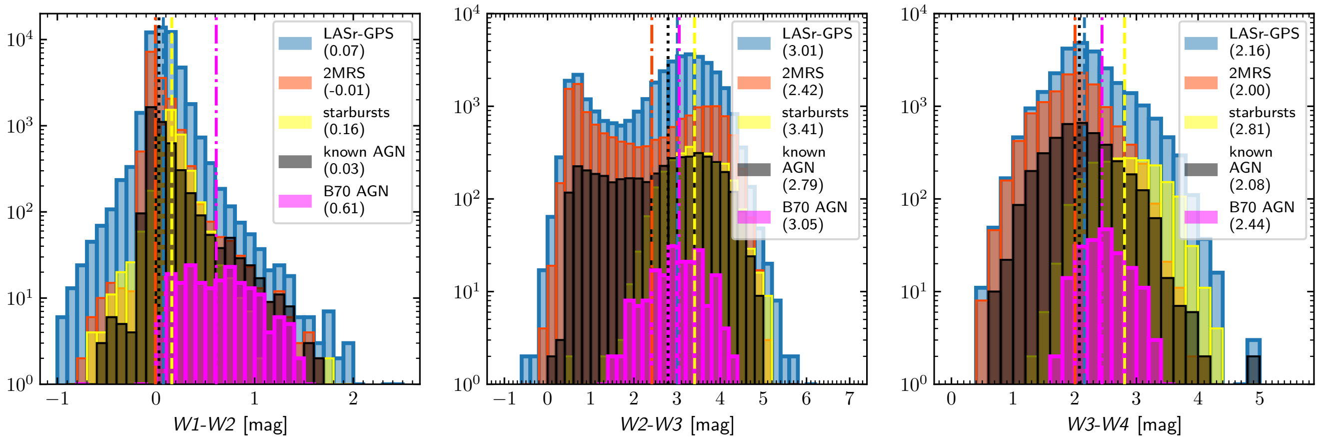

Figure 14. *WISE* colours *W1-W2* (left), *W2-W3* (middle) and *W3-W4* (right) distributions of all galaxies from the 2MRS (orange) and LASr-GPS (blue) that have detections in the corresponding bands of each colour. The distribution of known starbursts is shown in yellow, while known AGN are shown in black and B70 AGN are shown in magenta. In addition, the median colours for each subsample are shown as vertical dashed, dotted and dash-dotted lines of the corresponding colour, and listed in the figure legends.

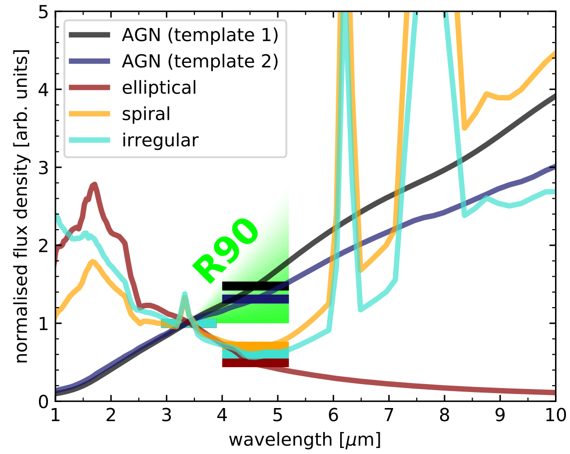

Figure 15. Illustration of the R90 *WISE* colour selection criterion based in *W1-W2*. The solid lines show the different SED templates for AGN and galaxy types taken from Assef et al. (2010), see that work for details. The thick horizontal bars indicate the synthetic photometry in *W1* and *W2*, for each SED in the same color, respectively. The SEDs are normalised to the *W1* synthetic flux density. The green semitransparent triangle indicates the SED slopes that would be selected by the R90 criterion as AGN. *W1-W2* = 0.65 mag corresponds to straight line in flux density space.

luminous AGN. This effect is clearly visibile in Fig. 16, where galaxies hosting known AGN, and in particular those from the B70 AGN sample, exhibit a trend of redder *W1-W2* colour for increasing *W3* luminosity. The $L(W3)$ and estimated $L^{\rm nuc}(12\,\mu{\rm m})$ distributions of R90 selected objects are shown in Fig. 17. While the median $L(W3)$ of known AGN is $10^{42.2}$ erg s^{-1}, the corresponding median luminosity for R90 selected AGN is more than 1 dex higher, i.e., $10^{43.3}$ erg s^{-1}. For B70 AGN the trend is similar albeit smaller, i.e., 0.3 dex. If instead of the observed $L(W3)$, we use the estimated AGN luminosity, $L^{\rm nuc}(12\,\mu{\rm m})$, the trend becomes even clearer, and the gap in luminosities larger (1.6 dex for all known AGN and 0.5 dex for the B70 AGN.

To quantify the fraction of AGN selected by the R90 criterion we look at its luminosity dependence in Fig. 18 for different subsamples of known AGN. Independent of the AGN subsample and selected luminosity as AGN power tracer, for $L \lesssim 10^{42.5}$ erg s^{-1} the fraction of AGN selected by the R90 criterion is relatively low and constant, while for higher luminosities is rapidly increases. For using *W3* as AGN power tracer, the fraction of AGN selected by R90 levels off at a relatively low 60 − 70% for $L(W3) > 10^{43.5}$ erg s^{-1} (grey line in Fig. 18). Most of the remaining 30 − 40% of AGN not selected by R90 despite high *W3* luminosity are situated in heavily star forming galaxies that dominate the MIR over the AGN. These are classified as HII in the optical indicating that the corresponding AGN are intrinsically much less luminous than $L(W3)$ values suggest. Indeed, if we use the decontaminate $L^{\rm nuc}(12\,\mu{\rm m})$ estimates from Sect. 4.1, the R90-selected fraction increases more rapidly, reaching 67% at $L^{\rm nuc}(12\,\mu{\rm m}) > 10^{43.1}$ erg s^{-1} and peaking at 92% (black line in Fig. 18). The completeness of the R90 selection even further increases if one only looks at the X-ray luminous B70 AGN (magenta line in Fig. 18). For this particular sample, we have the advantage of a better tracer of the AGN power than the *W3* luminosity, namely the intrinsic 2-10 keV X-ray luminosity (taken from Ricci et al. 2017). This allows us to assess the "true" efficiency of the R90 criterion (dark violet line in Fig. 18). Namely, R90 selects 54 ± 9% of the AGN with $L^{\rm int}$(2-10 keV) $> 10^{42}$ erg s^{-1}, while for $L^{\rm int}$(2-10 keV) $> 10^{43}$ erg s^{-1}, 86 ± 26% are selected[18]. Using our estimated $L^{\rm nuc}(12\,\mu{\rm m})$ gives similar results to $L^{\rm int}$(2-10 keV) which confirms the validity of our decontamination of the former in Sect. 4.1. In addition, the comparison between the R90 fractions depending on $L(W3)$ and $L^{\rm int}$(2-10 keV) for the B70 sample verifies that the $L(W3)$-based fractions are to be regarded as lower limit on the true efficiency of the R90 selection.

4.4 New AGN candidates

Not all the galaxies selected by the R90 criterion are already known to host AGN. There are 159 such galaxies, and thus new AGN candidates based on their *W1-W2* colour. We double-check all galaxies individually to make sure that they are genuine galaxies with valid *WISE* measurements and robust redshifts (as far as we can assess from the information at hand). The resulting list of new AGN candidates and their properties can be found in Table 3. Only 31 (19%) of the hosts of the new AGN candidates are in the 2MRS sample, indicating that they are relatively faint or compact galaxies. Indeed, the median $L(W3)$ of the candidate systems is only 10^{42} erg s^{-1}, so much lower than the median of the verified AGN systems that fulfil the R90 criterion ($10^{43.3}$ erg s^{-1}; see Fig. 17, top). If we apply our *W3* decontamination (Sect. 4.1), the resulting $L^{\rm nuc}(12\,\mu{\rm m})$ distribution fractures into two peaks, one peaking at $L^{\rm nuc}(12\,\mu{\rm m}) \sim 10^{41.3}$ erg s^{-1} and the other at $L^{\rm nuc}(12\,\mu{\rm m}) \sim 10^{42.6}$ erg s^{-1} (Fig. 17, bottom). This is caused by 51 of the AGN candidates having H II or starburst classifications and thus higher corrections to their $L(W3)$. It indicates that a significant fraction of objects with low $L(W3)$ luminosities might be contaminants, i.e., not AGN but star-formation dominated systems.

4.4.1 *On contamination by starbursts*

The R90 criterion was designed for selecting distant, luminous and point-like AGN. Its 90% reliability in selecting AGN might not hold for local, extended galaxies. We saw in Fig. 13 that the large majority of star-forming galaxies lie on the red *W2-W3* tail of the main sequence but significantly below typical AGN *W1-W2* colours . However, it was argued by Hainline et al. (2016) that strong star formation, in particular in dwarf galaxies, can also lead to red, AGN-like *W1-W2* colours. These systems would then have as well very red *W2-W3* colours ($\gtrsim$ 4 mag) which would motivate to add a *W2-W3* colour cut to improve the reliability of a *W1-W2* -based AGN selection. Satyapal et al. (2018) further investigated this with theoretical colour tracks of extreme starburst systems and determined a theoretical *W2-W3* colour criterion (hereafter S18):

$$W2 - W3 < 0.17\,(W1 - W2 + 24.5),$$

to separate AGN and starbursts. This criterion is plotted in Fig. 13 as orange dot-dashed line and marked for individual known R90 AGN and R90 AGN candidates in Table 2 and Table 3, respectively. Of the 159 R90 AGN candidates, 100 (63%) fulfil the S18 criterion and, thus, are expected to not be starburst dominated. Among the R90 AGN candidates not fulfilling S18, there are indeed some of those compact star-forming galaxies that Hainline et al. (2016) identified as "AGN imposters" (e.g., II Zw 40, Mrk 193, SBS 0335-052, and UGC 5189). In total, 28 (18%) of the AGN candidates are

[18] The relatively large uncertainties results from the small number statistics of the B70 within the volume at such high luminosities.

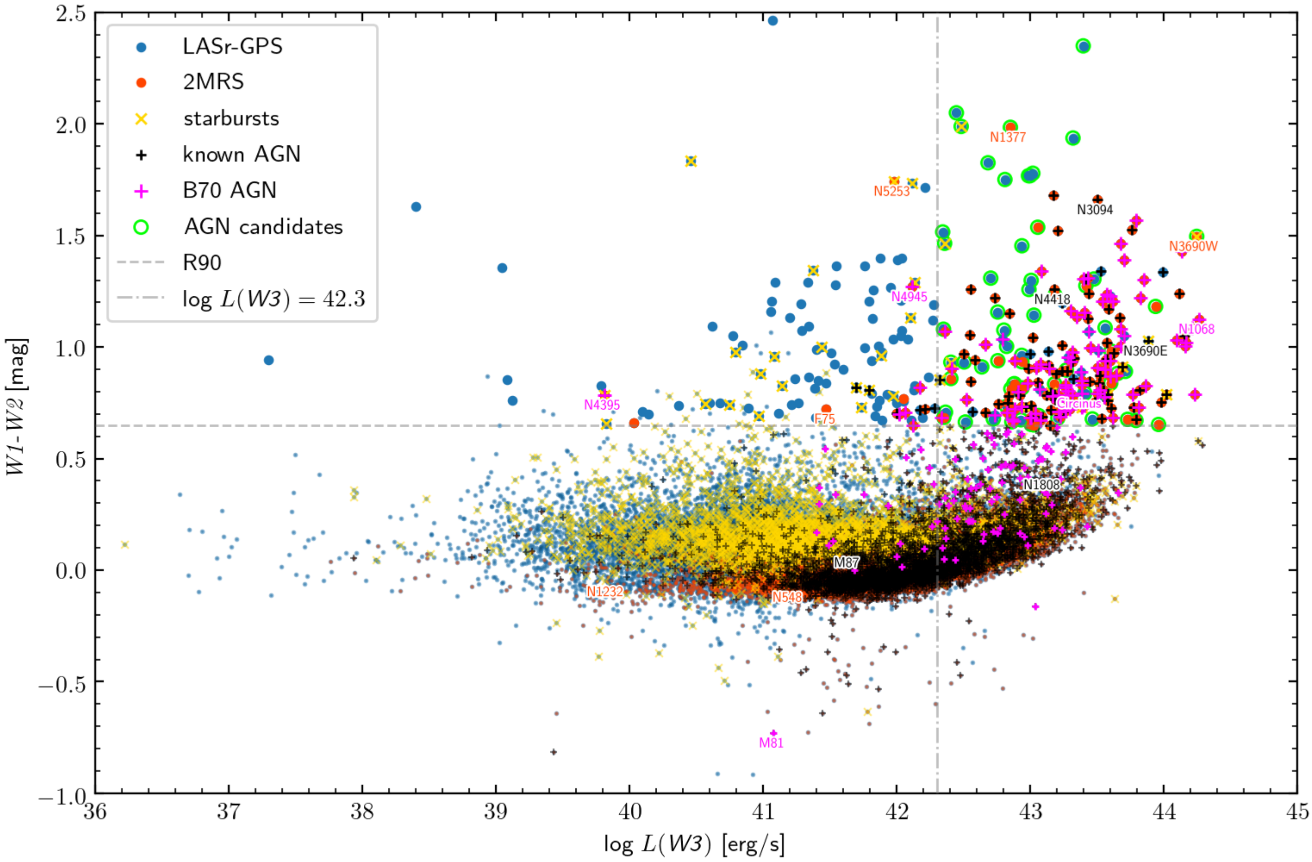

Figure 16. *W1-W2* colour over *W3* luminosity for all galaxies from the LASr-GPS detected in *W1*, *W2* and *W3*. Description of the symbols is as in Fig. 13. In addition, the vertical dot-dashed line marks $L(W3) = 10^{42.3}$ erg s^{-1}.

classified as starbursts or blue compact dwarfs in our literature collection. However, only 14 (50%) of them would be excluded by the S18 criterion.

Among the known AGN, 89% (154 of 172) fulfil the S18 criterion[19]. For the B70 AGN, fulfilment is even 98% (89 of 91). Of the 17 R90 AGN not fulfilling S18, nine show signs of strong star formation in the literature and are in fact controversial concerning the existence of luminous AGN in these galaxies[20]. On the other hand, two of the remaining galaxies, NGC 4418 (aka NGC 4355) and 2MASX J04282604-0433496, show no signs of strong star formation, judging from their *Spitzer*/IRS spectra (Asmus et al. 2014). Instead, NGC 4418 hosts a highly obscured nucleus with the obscuration probably causing the red *W2-W3* colour (see e.g., Roche et al. 2015). In fact, both objects are among the reddest in terms of *W2-W3* colour (> 5) of all galaxies in the LASr-GPS. While, the nature of the dominating MIR emitter in NGC 4418 is still somewhat controversial (e.g., Sakamoto et al. 2013; Varenius et al. 2014), the case of object makes clear that also heavy obscuration can lead to very red *W2-W3* colours[21]. Thus, the application of the S18 criterion might exclude the most obscured AGN, which are the ones we are hunting for!

In addition, for a complete, unbiased sample of AGN, one wants to include even star-formation dominated galaxies, as long as the intrinsic luminosity of the AGN is above the selected lower threshold[22]. We conclude from this discussion that applying a *W2-W3*-based criterion like the S18 in addition to the R90 criterion indeed increases pureness of AGN selection. However, a significant fraction of starbursts still remains while many AGN that are either heavily obscured or live in hosts with dominating star formation are excluded.

Instead, we notice that in the *W3* luminosity distribution in Fig. 17 that most of the starbursts have relatively low luminosities. For example, 90% (25 of 28) of the starbursts and BCDs selected by R90 have $L(W3) < 10^{42.3}$ erg s^{-1}. This suggests that a lower luminosity cut could be more successful at removing contaminating non-AGN galaxies with dominating starbursts. Using $L(W3) > 10^{42.3}$ erg s^{-1} as threshold, leaves 61 of the R90 AGN candidates which according to the above number should be genuine AGN with 90% probability. They are marked with green circles in Fig. 13 and Fig. 16.

[19] One object, Mrk 3 aka UGC 3426 has no valid *W3* measurement and thus S18 can not be computed.

[20] These are Arp 220, CGCG 032-017, Mrk 93, NGC 253, NGC 3256, NGC 3690E, NGC 7130, NGC 7552, and TOLOLO 1220+051.

[21] See also the similarly mysterious Arp 220; e.g., Martín et al. 2016; Paggi et al. 2017; Sakamoto et al. 2017; Yoast-Hull et al. 2017).

[22] Finding such objects is difficult with *WISE* colour selection alone but might require high angular resolution data over a wide wavelength range, something we plan for the future with dedicated follow-up of these red objects.

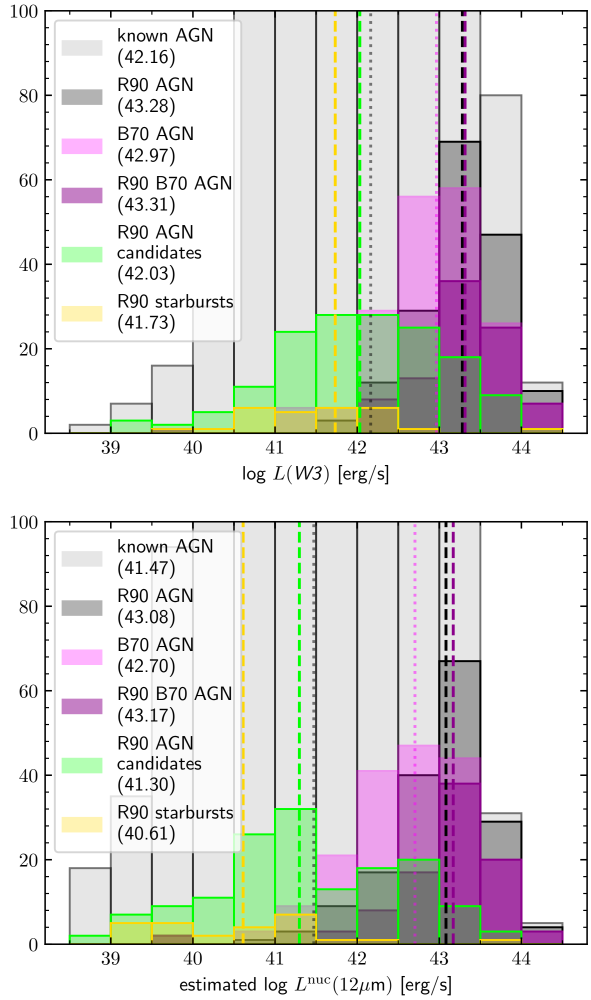

Figure 17. Top: *W3* luminosity distribution for R90 selected AGN and candidates in comparison to all known AGN (grey) and B70 AGN (light magenta). R90 selected objects from all known AGN are shown in black, from B70 in dark magenta, from unidentified AGN in green and from known starbursts in gold. The dashed lines of the corresponding colour mark the median value which is also shown in the legend.
Bottom: Corresponding estimated $L^{\rm nuc}(12\,\mu{\rm m})$ distribution after decontamination of $L(W3)$ following Sect. 4.1.

4.4.2 *Prospects for detection in X-rays*

There is a close correlation between the observed MIR and intrinsic X-ray luminosities for local AGN (e.g. Lutz et al. 2004; Gandhi et al. 2009), allowing us to estimate the intrinsic X-ray AGN luminosities of our new AGN candidates and infer the chances to detect them with the X-ray all-sky missions, *Swift*/BAT, *SRG*/ART-XC/eROSITA. In the following, we detail our Monte Carlo simulation per source to estimate the detection rates for the 61 R90 AGN candidates with $L(W3) > 10^{42.3}\,{\rm erg\,s}^{-1}$ (corresponding to intrinsic X-ray luminosities above the nominal sensitivity of eROSITA after eight passes; $F^{\rm obs}(2\text{-}10\,{\rm keV}) \gtrsim 1.6\cdot10^{-13}\,{\rm erg\,cm}^{-2}{\rm s}^{-1}$ (Merloni et al. 2012)). In particular, these steps are performed:

(i) $L^{\rm nuc}(12\,\mu{\rm m})$ **prediction:** we use the $L(W3)$ decontamination method from Sect. 4.1 to estimate $L^{\rm nuc}(12\,\mu{\rm m})$.

(ii) **Intrinsic $L_{\rm X}$ prediction:** we use the most accurate determination of the MIR–X-ray luminosity relation by Asmus et al. (2015) to convert $L^{\rm nuc}(12\,\mu{\rm m})$ into $L^{\rm int}(2\text{-}10\,{\rm keV})$:

$$\log\left(\frac{L^{\rm int}(2\text{-}10\,{\rm keV})}{10^{43}{\rm erg\,s}^{-1}}\right) = -0.32 + 0.95\log\left(\frac{L^{\rm nuc}(12\,\mu{\rm m})}{10^{43}{\rm erg\,s}^{-1}}\right)$$

with an observed scatter of 0.4 dex.

(iii) $N_{\rm H}$ **assignment:** to estimate the observed X-ray fluxes from $L^{\rm int}(2\text{-}10\,{\rm keV})$, we have to assign an obscuring column density, $N_{\rm H}$. Here, we use the bias-corrected intrinsic $N_{\rm H}$ distribution from the BAT 70 month AGN (Ricci et al. 2015) as reference probability function to draw a random $N_{\rm H}$ (shown in Fig. 19, left).

(iv) **Application of extinction:** In Fig. 19, middle, we show the B70 AGN observed to intrinsic X-ray flux ratios vs. $N_{\rm H}$ from Ricci et al. (2017). This was fit with an exponential function, which was found to give a good description of the data yielding a theoretical extinction curve.

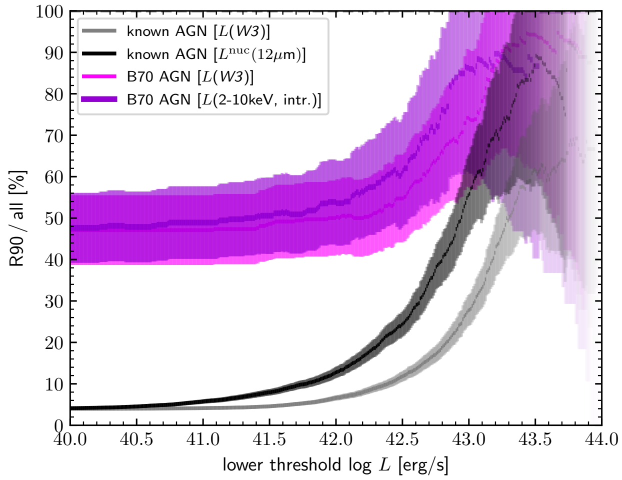

Figure 18. Fraction of AGN selected by the R90 criterion depending on luminosity. The grey line marks the fraction for all known AGN as a function of *W3* luminosity, while the black marks the fraction as a function of the estimated $L^{\rm nuc}(12\,\mu{\rm m})$. The thin magenta line shows the fraction for the B70 AGN as a function of *W3* luminosity, while the thick, dark violet line shows the same fraction but as a function of intrinsic 2-10 keV X-ray luminosity. The shaded regions indicate the 1-σ uncertainty on the number counts.

We then performed a Monte Carlo resampling of the above steps. We assumed the probability distributions of each $L^{\rm nuc}(12\,\mu{\rm m})$ and $L^{\rm int}(2\text{-}10\,{\rm keV})$ value to be Gaussian-distributed with width equal to the observed scatter in both conversions (much larger than the individual source X-ray fit uncertainties). For 10^4 iterations, the resulting observed X-ray flux distributions are stable (Fig. 19, right) and can be compared to the flux limits provided for the all-sky surveys of *Swift*/BAT and *SRG*/eROSITA[23].

According to this simulation, we would expect to detect 33 ± 9 of the 61 R90 AGN candidates already in the first pass of the eROSITA all-sky survey, and 43 ± 6 in the full survey. The remaining objects would then expected to be highly obscured, with

[23] We omit ART-XC here because its different energy band would require futher conversion with additional uncertainties but given the flux limit of its all-sky survey (Pavlinsky et al. 2018), we expect detection rates to be a factor two to three lower than with eROSITA.

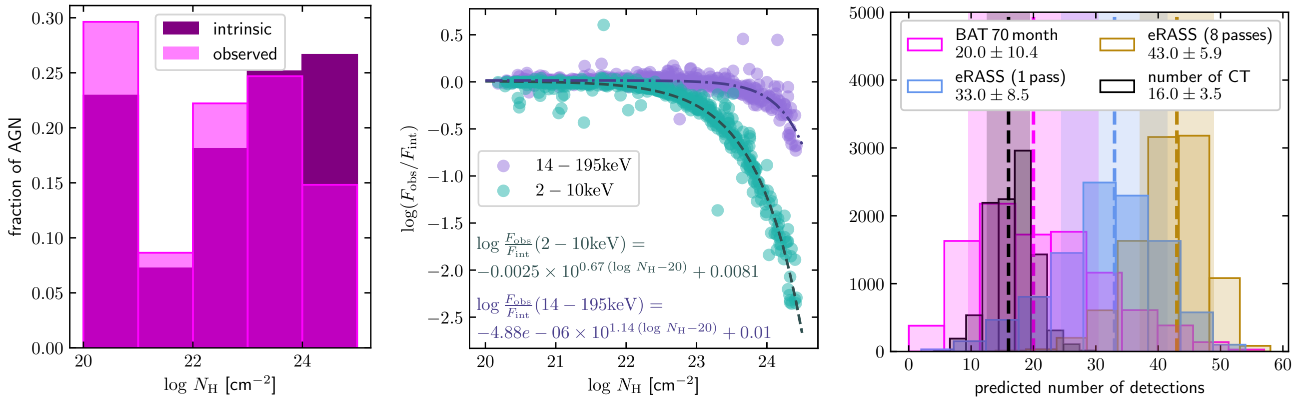

Figure 19. *Left:* normalised distributions of obscuring column density, N_H, for the BAT 70 month AGN sample. In light magenta is shown the observed distribution for the B70 AGN in LASr fulfilling R90, while in dark purple is shown the inferred intrinsic distribution from Ricci et al. (2015).
Middle: empirical X-ray extinction curves for the BAT 70 month AGN sample with $10^{20} \leq \log(N_H\,\mathrm{cm}^2) \leq 24.5$ for observed and intrinsic fluxes as well as N_H values taken from Ricci et al. (2017). In purple is the shown the observed to intrinsic flux ratio for the 14-195 keV energy range, while in green the same is shown for the 2-10 keV range. The darker colored dot-dashed and dashed lines give exponential fits to the data, respectively, with the corresponding best parameters shown as well in the same color.
Right: simulated detection rates for *Swift*/BAT after 70 months (magenta) and *SRG*/eROSITA after one (blue) and eight all-sky passes (gold). The distributions show the results of the iterations of the Monte Carlo simulation using the intrinsic N_H distribution, while the dashed lines give the median and the shaded areas the standard deviation. These values are given in the legend as well. In addition, the expected number of CT AGN is shown in black.

16±3.5 objects expected to be CT obscured. However, if we convert the intrinsic 2-10 keV fluxes into 14-195 keV fluxes using the median ratio 0.42 ± 0.25 dex as determined from the BAT 70 month AGN, then we would expect that 20 ± 10 of the candidates[24] would have been detected already in the 70 month *Swift*/BAT all-sky map with the nominal detection limit is F^{obs}(14-195 keV) = $1.34 \cdot 10^{-11}$ erg cm^{-2}s^{-1} (Baumgartner et al. 2013). This might indicate that a larger fraction of the R90 AGN candidates are highly obscured than assumed. On the other hand, the fact that none are detected in the 70 month BAT map is in fact consistent with the design-based expectation that only 90% of the 221 galaxies that fulfill the R90 criterion indeed host an AGN. In other words, we have to expect that ~ 22 of the 221 R90 objects are contaminants, and all of them would be among the R90 AGN candidates.

Alternatively, one could argue that possibly many of the CT obscured AGN that are missing according to the difference of the intrinsic to observed N_H distribution (Fig. 19) are among the R90 AGN candidates. If we assume that the R90 selection is independent of X-ray obscuration, we expect 54 CT objects according to the intrinsic N_H distribution from Ricci et al. (2015), while only 18 AGN are currently known to be CT obscured, as we further discuss in Sect. 4.5. Therefore, easily twice as many CT AGN might be present among the candidates as assumed in the above simulation which would then lower the expected detection rates correspondingly, and, in particular, remove any expected detections in the BAT 70 month map.

4.5 On the CT AGN fraction and CT candidates

As discussed in Sect. 1, one of the main caveats of current AGN samples is the bias against the most obscured, i.e. CT, objects[25].

The real fraction of the CT AGN is still highly uncertain with estimates ranging from 10% to 50% of all AGN (e.g., Burlon et al. 2011; Ricci et al. 2015; Akylas et al. 2016; Lansbury et al. 2017; Georgantopoulos & Akylas 2019; Gandhi & Fabian 2003; Gilli et al. 2007; Ueda et al. 2014; Ananna et al. 2019; Boorman et al., in prep.). The effort of building a complete AGN sample, starting with this work, will hopefully help to narrow down the uncertainty on this fraction. In the meantime, we can derive lower limits on the CT fraction by simply adding up the number of known CT AGN in the volume. The first lower limit comes from the B70 AGN sample. It has 20 out of 153 AGN with L^{int}(2-10 keV) > 10^{42} erg s^{-1} within the volume determined to be CT, i.e., a fraction of 13%. Among the R90 galaxies with $L(W3) > 10^{42.3}$ erg s^{-1}, 10 of the 84 B70 AGN are CT obscured, i.e., 12%. In addition, there are eight more known AGN that are not in the B70 but are CT and fulfill the R90 and luminosity cuts[26]. Together, this means at least 18 of the 160 R90 AGN with $L(W3) > 10^{42.3}$ erg s^{-1} are CT obscured, i.e., 11%.

However, it is likely that the true CT fraction is significantly higher as was indicated in Sect. 4.4.2 already, since none of the (predicted) intrinsically X-ray-bright R90 AGN candidates have been detected by BAT. In particular, if we assume the bias-corrected N_H distribution of Ricci et al. (2015), i.e., a CT fraction of 27%, to apply for all 221 R90 objects with $\log L(W3) > 10^{42.3}$ erg s^{-1}, then we would expect 60 CT AGN in total. Since in the BAT detected subset, there are only 10, there should be 50 CT AGN among the 137 R90 objects not in B70. To test whether this is consistent with the observations, we repeat the Monte Carlo simulation of Sect. 4.4.2 for these 137 objects assuming 50 CT AGN among

[24] The large uncertainty on this expected number of detections is caused by the scatter of the flux ratio in the X-ray bands.
[25] Note that CT AGN are likely not a special class of AGN but just the high end of a continuous obscuration distribution in the AGN population which is hard to detect because obscuration becomes opaque even at the highest photon energies.
[26] These are IC 3639, Mrk 573 aka UGC 1214, NGC 660, NGC 1320, NGC 1386, NGC 4418, NGC 5135, and NGC 5347 (in order of the object list: Boorman et al. 2016; Guainazzi et al. 2005; Annuar et al., in prep.; Baloković et al. 2014; Levenson et al. 2006; Maiolino et al. 2003; Singh et al. 2012; Levenson et al. 2006).

them. As a result we would still expect 60 ± 25 objects to have been detected in the 70 month BAT map. Even if we assume again 22 contaminants as a result of the R90 selection, this leaves 38 ± 25. In fact, it would take an intrinsic CT fraction of 40% to become consistent with no BAT detection within 1σ uncertainty. On the other hand, we do not expect more than $\sim$ 100 CT AGN among the 137 because of at least 14 of the known AGN being optically classified as type 1 AGN and thus unlikely CT. This would translate into an intrinsic CT fraction of 55% which we regard as an upper limit. These findings suggest that the intrinsic CT fraction is between $40 - 55\%$ in the here probed luminosity regime. However, these numbers should be regarded as indicative only owing the large number of very simplified assumptions made here.

Let us examine some of the objects in more detail. The most promising CT candidates are those with the highest MIR-to-X-ray ratio, for example sources that are not detected by *Swift*/BAT after 70 months but are 1 dex brighter than the *W3* magnitude corresponding to the nominal detection limit of $F^{\rm obs}$(14-195 keV) = $1.34 \cdot 10^{-11}$ erg cm^{-2}s^{-1}, namely *W3* < 4.7 mag. Indeed, we find that six out of the eight known CT AGN that remained undetected in the BAT 70 month map fulfil this criterion, so a 75% success rate. If we apply this magnitude limit to the whole R90 AGN sample excluding B70, we identify a further nine CT candidates among the known AGN. Six of them do not fulfil the S18 criterion and are in fact known to host starbursts (Arp 220, IC 1623B, NGC 253, NGC 3256, NGC 3690E, and NGC 7552)[27]. So their *W3* emission could be star-formation dominated. This leaves three more robust CT AGN candidates (ESO 420-13, NGC 1377, and NGC 3094).

We can also apply this diagnostic to the R90 AGN candidates which yields six galaxies, of which three are known to host starbursts (MCG +12-02-001, NGC 520 and NGC 3690W), leaving another three candidates for CT AGN (ESO 127-11, ESO 173-15, and ESO 495-5). We plan to investigate these candidates further in the future.

4.6 Total number of AGN estimate

Even without having confirmed all the R90 objects as AGN, we can make a rough estimate of the total number of AGN above a given luminosity limit within the volume based on the characterisation of the criterion and found numbers from the previous sections. The main assumption is that the defining feature of the R90 criterion is valid also in our volume, namely that 90% of galaxies with such a red *W1*-*W2* colour indeed host an AGN, at least for objects with $L(W3) > 10^{42.3}$ erg s^{-1} as concluded in Sect. 4.4.1. This lower luminosity limit matches well with our completeness limit for the LASr-GPS (Sect. 3.2). Furthermore, R90 selects the majority of AGN with luminosities greater than this threshold (Sect. 4.3). Therefore, we use $L(W3) > 10^{42.3}$ erg s^{-1} here in the absence of a more accurate AGN power tracer.

There are 221 R90 galaxies with $L(W3) > 10^{42.3}$ erg s^{-1}, of which 160 are known to host an AGN, 84 of which are in the B70 sample. According to the R90 definition, we expect that 199 (90%) of them host genuine AGN. This number is consistent with applying the S18 cut to the R90 sample instead, which would return 186 objects, i.e., 84%, which is slightly lower but we know that S18 also removes some AGN. Owing the complications of S18 discussed in Sect. 4.4.1, we stick with the simple R90-based estimate in the following, i.e., our initial estimate for the total number of AGN in the volume is $N_{\rm ini} = 199$. For the final best estimate, this number has to be corrected by the various factors of incompleteness as discussed in the following.

4.6.1 *Colour selection incompleteness*

The main source of incompleteness is the colour selection. The R90 criterion from Assef et al. (2018) was designed for high reliability. This reliability comes at the price of a significant level of incompleteness, which we have seen already in Sect. 4.3. Namely, for a lower luminosity of $L(W3) > 10^{42.3}$ erg s^{-1}, only $51 \pm 10\%$ of AGN are selected. Thus, we require $N_{\rm ini}$ to be multiplied by a colour selection incompleteness correction factor, $c_{\rm CSI} = 1.95^{+0.48}_{-0.32}$. This factor does not yet account for contamination of the $L(W3)$ flux, which is addressed next.

4.6.2 *Host contribution to W3*

Host contribution, mostly through star formation, to *W3* leads us to overestimate the intrinsic AGN luminosity and, thus, to the inclusion of AGN with intrinsic luminosities below our completeness limit. We have already estimated this effect statistically in Sect. 4.1 and applied a corresponding correctop in the Monte Carlo simulations of Sect. 4.4.2. Thus, we here just repeat the first part of the Monte-Carlo simulation of that section to estimate the $L^{\rm nuc}(12\,\mu{\rm m})$ distribution for the AGN in our R90 galaxies, where no direct measurement is available. This way, we find that 187 ± 22 out of the 221 ($85 \pm 10\%$) of the R90 galaxies have expected $L^{\rm nuc}(12\,\mu{\rm m}) > 10^{42.3}$ erg s^{-1} . Therefore, the corresponding host contamination correction factor is $c_{\rm HC} = 0.85 \pm 0.1$.

4.6.3 *Parent sample incompleteness*

Another source of incompleteness is of course the galaxy parent sample used for the AGN selection. The level of incompleteness of the LASr-GPS was estimated in Sect. 3.2. There, we used *W1* as rough tracer of the stellar mass of the galaxies, while here we want to know the completeness with respect to the $L(W3)$ luminosity threshold. Thus, we repeat the completeness analysis of Sect. 3.2 but using *W3*, and find that for $L(W3) > 10^{42.3}$ erg s^{-1} and $|b| > 8°$, the galaxy parent sample is $96.1 \pm 4.2\%$ complete[28]. As discussed in Sect. 3.2.3, the shadow of the Milky Way further increases the incompleteness of the parent sample by $6.4 \pm 0.8\%$. Therefore, we adopt a total galaxy parent sample incompleteness correction factor, $c_{\rm PSI} = 1.11 \pm 0.04$.

4.6.4 *Other corrections, not accounted for*

We did not attempt to correct for the fact that redshift-independent distances are not available for all of the galaxies. This is the case for 71% of the R90 AGN and candidates. We found that the redshift independent distances are on average 10% smaller than the

[27] However, Teng et al. (2015) find that the X-ray data of Arp 220 is consistent with a CT AGN being present in this source.

[28] The crossmatching with *WISE* is normally another source of incompleteness but we found *WISE* counterparts for all galaxies in the LASr-GPS. On the other hand, the *WISE* counterparts for 1.4% of the galaxies were drowned by brighter nearby objects (Sect. 2.7). However, we do not consider this effect in the total number of AGN estimate because it is much smaller than the uncertainties of the other corrections.

redshift-based distances. This would mean that the luminosities of these galaxies would decrease by 0.04 dex, leading to the loss of 3 candidate AGN but none of the known AGN. At the same time, 31 additional known AGN and 20 candidates would fall into the volume. However, since we did not consider redshift-independent distances for galaxies with $D_L > 50$ Mpc, a correction is not straightforward and thus not applied here.

In addition to the above incompleteness effects, there are also object intrinsic effects like obscuration in the MIR. The latter, however, has little effect on the *W1*-*W2* colour at low redshifts as shown in Stern et al. (2012), because extinction at the wavelengths of *W1* and *W2* is low and approximately constant in typical extinction laws (e.g., Fritz et al. 2011). Thus, no correction for that is applied here.

Finally, one might ask, what about beamed MIR emission, i.e., blazars? Out of the full sample of 838 AGN in the full BAT 70 month catalogue, 105 are classified as beamed sources according to BZCAT (Massaro et al. 2009), and 5 are in our $D < 100$ Mpc volume, implying a beamed fraction of ∼ 3%! On the other hand, all of these 5 objects are known to have SEDs that are not dominated by beamed emission (Cen A, Mrk 348, NGC 1052, NGC 1275, NGC 7213). This suggests that the true beamed fraction is ≪ 1%, and, thus we ignore this effect here.

4.6.5 *Best estimate*

We applied all the above correction factors to our initial average estimate, $N_{\mathrm{ini}} = 199$, to arrive at our best estimate:

$$N_{\mathrm{best}} = N_{\mathrm{ini}} \cdot c_{\mathrm{CSI}} \cdot c_{\mathrm{HC}} \cdot c_{\mathrm{PSI}} = 1.82 N_{\mathrm{ini}} = 362^{+145}_{-116}$$

AGN with $L^{\mathrm{nuc}}(12\,\mu\mathrm{m}) > 10^{42.3}\,\mathrm{erg\,s^{-1}}$ (equivalent to $L^{\mathrm{int}}(2\text{-}10\,\mathrm{keV}) > 10^{42}\,\mathrm{erg\,s^{-1}}$) in our $D < 100$ Mpc volume. This corresponds to a number density of $8.6^{+3.5}_{-2.8} \times 10^{-5}\,\mathrm{Mpc^{-3}}$.

We also repeat the above estimation for $L^{\mathrm{int}}(2\text{-}10\,\mathrm{keV}) > 10^{43}\,\mathrm{erg\,s^{-1}}$ and $L^{\mathrm{int}}(2\text{-}10\,\mathrm{keV}) > 10^{44}\,\mathrm{erg\,s^{-1}}$, resulting in 101^{+55}_{-25} and 4^{+2}_{-1} AGN above these luminosity thresholds, respectively. These compare to 53 and 2 AGN known with $L^{\mathrm{int}}(2\text{-}10\,\mathrm{keV}) > 10^{43}\,\mathrm{erg\,s^{-1}}$ and $L^{\mathrm{int}}(2\text{-}10\,\mathrm{keV}) > 10^{44}\,\mathrm{erg\,s^{-1}}$, respectively, within the volume.

4.7 Comparison to estimates from luminosity functions

Finally, with these purely observational estimates for the number of AGN within 100 Mpc, one might want to compare to the predictions from currently used AGN luminosity functions. First, we compare to an optical luminosity function, namely the one derived by Palanque-Delabrouille et al. (2013) for luminous AGN in the redshift range $0.7 < z < 4$, whereas its shape was assumed to be a standard double power law following Boyle et al. (2000). For a redshift of 0.01, they found a break magnitude of -22.1 and the power-law indices $\alpha = 3.5$ and $\beta = 1.43$, while the break value for the bolometric luminosity is $\sim 10^{45}\,\mathrm{erg\,s^{-1}}$. Here, we used the lower cut-off of $10^{43}\,\mathrm{erg\,s^{-1}}$ for the bolometric luminosity which with the simple assumption of $L_{\mathrm{bol}} = 10 L^{\mathrm{int}}(2\text{-}10\,\mathrm{keV})$ (e.g., Vasudevan & Fabian 2007) corresponds to the same lower luminosity cut used for our total AGN number estimate in the previous section, i.e., $L^{\mathrm{int}}(2\text{-}10\,\mathrm{keV}) = 10^{42}\,\mathrm{erg\,s^{-1}}$. We then integrated the luminosity function over the whole sky up to a redshift of 0.0222 (corresponding to our distance limit of 100 Mpc). This results in an estimated number of optical AGN of 82. The latter number corresponds only to the unobscured AGN, so we need to correct for the obscuration fraction which is somewhere between ∼ 50% to 80% (e.g., Schmitt et al. 2001; Hao et al. 2005), resulting in 164 to 410 objects.

Instead of an optical luminosity function, using an X-ray luminosity function has the advantage of also including obscured AGN (e.g., Ueda et al. 2003). There is a large variety of such functions available in the literature. For simplicity, we here choose only one of the recent works that attempted to incorporate the CT fraction as well, namely Aird et al. (2015). This work compares several different approaches for determining an X-ray luminosity function, and we refer the reader to that work for more details. We try several of those functions, for example the luminosity-dependent density evolution model which returns an estimate of 125 AGN including obscured objects, while the flexible double power law (FDPL) yields a total number estimate of 175 AGN above our luminosity limit. Finally, Aird et al. (2015) put forward a model that includes a description of the absorption distribution function (XLAF), allowing to compute the number of unobscured and obscured AGN separately. It results in an estimate of 97 unobscured and 264 obscured AGN, i.e., 361 AGN in total. This number is indeed very close to our best estimate of 362 AGN in our volume and also agrees well with a corresponding estimate using the luminosity function from Ueda et al. (2014). Interestingly, the best fitting CT/Compton-thin obscured fraction found in Aird et al. (2015) of 34% predicts that 90 out of the 361 AGN are CT, i.e., a total CT fraction of 25%. Once, the R90 AGN sample has been better characterised and the candidates verified, more constraining tests will be possible.

5 SUMMARY & CONCLUSIONS

The recent and ongoing sensitive all-sky surveys including *WISE*, eROSITA and ART-XC , in combination with the collected knowledge of large astronomical databases, now allow us to obtain a complete census of significantly accreting SMBHs manifesting as AGN in the local Universe. This is the goal of LASr, and this work has presented the first steps in this project. In particular, we first created a LASr galaxy parent sample, LASr-GPS, of ∼ 49k galaxies by combining NED, SIMBAD, SDSS and 2MRS for a volume of $D < 100$ Mpc. We then crossmatched the sample with *WISE* to obtain the MIR properties of the host galaxy bulges. The analysis based on this sample leads to the following main results:

- First, we estimated the resulting LASr-GPS is ∼ 90% complete for galaxies with central (bulge) luminosities of $L(W1) > 10^{42}\,\mathrm{erg\,s^{-1}}$ (Sect. 3.2), a factor ∼ 4 deeper than the 2MRS galaxy sample (Sect. 3.1).
- The 20.6k galaxies above this luminosity harbour 4.3k known AGN collected from identifications in the literature (Sect. 2.4). However, we caution the reader that not all of these AGN identifications might be reliable which is particularly true for the controversial class of the LINERs. Of these 56% have an optical classification as Seyfert with the apparent type 2 to type 1 ratio between 49 to 60%.
- We compute optical classification-based corrections to estimate the nuclear 12 µm luminosities of the AGN from the *W3* profile fitting magnitudes, and find that the majority of the known AGN have low luminosities, i.e., only 18% are estimated to have $L^{\mathrm{nuc}}(12\,\mu\mathrm{m}) > 10^{42.3}\,\mathrm{erg\,s^{-1}}$ (Sect. 4.1).
- We then proceed to use *WISE*-based AGN identification by MIR colour to find new AGN candidates. For this purpose we employ the R90 criterion from Assef et al. (2018), which is based on the *W1*-*W2* and selects AGN with a 90% pureness. We estimate that

this criterion has an average efficiency of 51 ± 10% to select AGN with $L^{\rm int}$(2-10 keV) > 10^{42} erg s^{-1} (Sect. 4.3).

• The R90 criterion selects 172 galaxies known to host AGN (Sect. 4.3), and 159 AGN *candidates* (Sect. 4.4). Of the R90 selected AGN, 97% are classified optically as Seyferts with an apparent type 2 fraction between 38 and 62%, depending on how objects with multiple or intermediate classifications are treated. The intrinsic optical type 2 fraction is likely higher than 50% because we expect most of the R90 candidates to be type 2. It could be up to 71%, depending how many of the R90 candidates are genuine AGN and obscured.

• We find that the *W2-W3*-based criterion presented by Satyapal et al. (2018) to exclude strong starbursts indeed further increases the pureness of R90 selected AGN but also excludes some highly obscured AGN and AGN hosted in star-forming galaxies (Sect. 4.4.1).

• A lower luminosity cut of $L(W3) > 10^{42.3}$ erg s^{-1} is 90% efficient at removing compact star-forming galaxies, so that remaining contamination in our R90 sample should be low (Sect. 4.4.1). This luminosity cut leaves 61 robust AGN candidates.

• We predict detection rates for the eROSITA all-sky survey, and find that the majority of the AGN candidates are expected to be highly obscured, in order to explain their non-detection by *Swift*/BAT and reach the expected intrinsic CT fraction for the whole sample (Sect. 4.4.2).

• The discussion of constraints on the CT fraction based on the R90 selected AGN sample indicates the intrinsic CT fraction is likely higher than the 27% estimated from the BAT 70 month sample, and could be up to 55% (Sect. 4.5).

• Finally, we use the R90 selection to estimate the total number of AGN with $L^{\rm int}$(2-10 keV) > 10^{42} erg s^{-1} within 100 Mpc to be 362^{+145}_{-116}, corresponding to a number density of $8.6^{+3.5}_{-2.8} \times 10^{-5}$ Mpc^{-3} (Sect. 4.6). This estimate is consistent with estimates from recent X-ray luminosity functions for AGN in the literature (Sect. 4.7).

In future LASr work, we plan to follow up the new AGN candidates, e.g., with optical spectroscopy and present a full characterisation of the R90 AGN sample, before adding additional AGN identification techniques, e.g., based on MIR variability to increase the fraction of identified AGN within 100 Mpc. In the long term, data from the X-ray missions will complement the MIR-based identification of AGN and provide intrinsic AGN power estimates, allowing us to combine MIR and X-ray diagnostics to identify and characterise the majority of CT AGN. The final volume-limited sample of LASr AGN should provide a robust redshift zero anchor for AGN population models.

ACKNOWLEDGEMENTS

The authors would like to especially thank the user support teams of NED and SIMBAD, without whom this work would not have been possible. DA would also like to give special thanks to the development teams of the two fantastic and ever-improving tools TOPCAT and Aladin, both of which played a fundamental part in this research. Furthermore, we cordially thank the referee for valuable comments that helped to improve the manuscript. DA acknowledges funding through the European UnionâĂŹs Horizon 2020 and Innovation programme under the Marie Sklodowska-Curie grant agreement no. 793499 (DUSTDEVILS). PG acknowledges support from STFC (ST/R000506/1) and a UGC-UKIERI Thematic Partnership. PG also acknowledges discussions with the *eROSITA* AGN team, especially A. Merloni and A. Georgakakis. P. B. acknowledges financial support from the STFC and the Czech Science Foundation project No. 19-05599Y. RJA was supported by FONDECYT grant number 1191124. SF acknowledges support from the Horizon 2020 ERC Starting Grant DUST-IN-THE-WIND (ERC-2015-StG-677117). FS acknowledges partial support from a Leverhulme Trust Research Fellowship. JA acknowledges support from an STFC Ernest Rutherford Fellowship, grant code: ST/P004172/1. This publication makes use of data products from the *Wide-field Infrared Survey Explorer*, which is a joint project of the University of California, Los Angeles, and the Jet Propulsion Laboratory/California Institute of Technology, funded by the National Aeronautics and Space Administration. We acknowledge the usage of the HyperLeda database (http://leda.univ-lyon1.fr; Makarov et al. 2014). This research made use of the NASA/IPAC Extragalactic Database (NED), which is operated by the Jet Propulsion Laboratory, California Institute of Technology, under contract with the National Aeronautics and Space Administration. This research has made use of the SIMBAD database, operated at CDS, Strasbourg, France (Wenger et al. 2000). This research has made use of "Aladin sky atlas" developed at CDS, Strasbourg Observatory, France (Bonnarel et al. 2000; Boch & Fernique 2014). This research made use of Astropy, a community-developed core Python package for Astronomy (Astropy Collaboration et al. 2013, 2018). This research has made use of NASA's Astrophysics Data System. This research has made use of TOPCAT (Taylor 2005).

REFERENCES

Aguado D. S., et al., 2019, ApJSS, 240, 23
Aird J., et al., 2010, MNRAS, 401, 2531
Aird J., Coil A. L., Georgakakis A., Nandra K., Barro G., Pérez-González P. G., 2015, MNRAS, 451, 1892
Akylas A., Georgantopoulos I., Ranalli P., Gkiokas E., Corral A., Lanzuisi G., 2016, A&A, 594, A73
Alexander D. M., Hickox R. C., 2012, New Astronomy Reviews, 56, 93
Alexander D. M., Bauer F. E., Chapman S. C., Smail I., Blain A. W., Brandt W. N., Ivison R. J., 2005, ApJ, 632, 736
Almeida C. R., Ricci C., 2017, Nature Astronomy, 1, 679
Ananna T. T., et al., 2019, ApJ, 871, 240
Asmus D., Hönig S. F., Gandhi P., Smette A., Duschl W. J., 2014, MNRAS, 439, 1648
Asmus D., Gandhi P., Hönig S. F., Smette A., Duschl W. J., 2015, MNRAS, 454, 766
Assef R. J., et al., 2010, ApJ, 713, 970
Assef R. J., et al., 2013, ApJ, 772, 26
Assef R. J., Stern D., Noirot G., Jun H. D., Cutri R. M., Eisenhardt P. R. M., 2018, ApJSS, 234, 23
Astropy Collaboration et al., 2013, A&A, 558, A33
Astropy Collaboration et al., 2018, AJ, 156, 123
Baldi R. D., et al., 2018, MNRAS, 476, 3478
Baldry I. K., et al., 2018, MNRAS, 474, 3875
Baloković M., et al., 2014, ApJ, 794, 111
Barthelmy S. D., et al., 2005, Space Science Reviews, 120, 143
Baumgartner W. H., Tueller J., Markwardt C. B., Skinner G. K., Barthelmy S., Mushotzky R. F., Evans P. A., Gehrels N., 2013, ApJSS, 207, 19
Belfiore F., et al., 2016, MNRAS, 461, 3111
Best P. N., Kauffmann G., Heckman T. M., Ivezić v., 2005, MNRAS, 362, 9
Blanton M. R., et al., 2017, AJ, 154, 28
Boch T., Fernique P., 2014, in Astronomical Data Analysis Software and Systems XXIII. p. 277, http://cdsads.u-strasbg.fr/abs/2014ASPC..485..277B
Bonnarel F., et al., 2000, A&A Supplement Series, 143, 33
Boorman P. G., et al., 2016, ApJ, 833, 245
Boyle B. J., Shanks T., Croom S. M., Smith R. J., Miller L., Loaring N., Heymans C., 2000, MNRAS, 317, 1014

Buchner J., et al., 2015, ApJ, 802, 89
Burlon D., Ajello M., Greiner J., Comastri A., Merloni A., Gehrels N., 2011, ApJ, 728, 58
Cid Fernandes R., StasiÅĎska G., Schlickmann M. S., Mateus A., Vale Asari N., Schoenell W., Sodré L., 2010, MNRAS, 403, 1036
Cid Fernandes R., StasiÅĎska G., Mateus A., Vale Asari N., 2011, MNRAS, 413, 1687
Cluver M. E., et al., 2014, ApJ, 782, 90
Collaboration P., et al., 2016, A&A, 594, A13
Cutri R. M., et al. 2012, VizieR Online Data Catalog, 2311
Cutri R. M., et al. 2013, VizieR Online Data Catalog, 2328
Davies R. I., et al., 2015, ApJ, 806, 127
Fabian A. C., 1999, MNRAS, 308, L39
Fabian A. C., 2012, ARA&A, 50, 455
Fritz T. K., et al., 2011, ApJ, 737, 73
Gandhi P., Fabian A. C., 2003, MNRAS, 339, 1095
Gandhi P., Fabian A. C., Suebsuwong T., Malzac J., Miniutti G., Wilman R. J., 2007, MNRAS, 382, 1005
Gandhi P., Horst H., Smette A., Hönig S., Comastri A., Gilli R., Vignali C., Duschl W., 2009, A&A, 502, 457
Gehrels N., et al., 2004, ApJ, 611, 1005
Georgantopoulos I., Akylas A., 2019, A&A, 621, A28
Gilli R., Comastri A., Hasinger G., 2007, A&A, 463, 79
Goulding A. D., Alexander D. M., Lehmer B. D., Mullaney J. R., 2010, MNRAS, 406, 597
Granato G. L., De Zotti G., Silva L., Bressan A., Danese L., 2004, ApJ, 600, 580
Guainazzi M., Matt G., Perola G. C., 2005, A&A, 444, 119
Hainline K. N., Reines A. E., Greene J. E., Stern D., 2016, ApJ, 832, 119
Hao L., et al., 2005, AJ, 129, 1795
Hickox R. C., Alexander D. M., 2018, ARA&A, 56, 625
Ho L. C., 2009, ApJ, 699, 626
Hönig S. F., 2019, ApJ, 884, 171
Hsieh B. C., et al., 2017, The ApJL, 851, L24
Huchra J. P., et al., 2012, ApJSS, 199, 26
Ichikawa K., Ricci C., Ueda Y., Matsuoka K., Toba Y., Kawamuro T., Trakhtenbrot B., Koss M. J., 2017, ApJ, 835, 74
Jarrett T. H., Chester T., Cutri R., Schneider S. E., Huchra J. P., 2003, AJ, 125, 525
Jarrett T. H., Cluver M. E., Brown M. J. I., Dale D. A., Tsai C. W., Masci F., 2019, ApJSS, 245, 25
Kewley L. J., Groves B., Kauffmann G., Heckman T., 2006, MNRAS, 372, 961
Kormendy J., Ho L. C., 2013, ARA&A, 51, 511
Koss M., et al., 2017, ApJ, 850, 74
Kulkarni S. R., Perley D. A., Miller A. A., 2018, ApJ, 860, 22
Lansbury G. B., et al., 2017, ApJ, 846, 20
Lapi A., Shankar F., Mao J., Granato G. L., Silva L., De Zotti G., Danese L., 2006, ApJ, 650, 42
Levenson N. A., Heckman T. M., Krolik J. H., Weaver K. A., Życki P. T., 2006, ApJ, 648, 111
Liske J., et al., 2015, MNRAS, 452, 2087
Lutz D., Maiolino R., Spoon H. W. W., Moorwood A. F. M., 2004, A&A, 418, 465
Maiolino R., et al., 2003, MNRAS, 344, L59
Makarov D., Prugniel P., Terekhova N., Courtois H., Vauglin I., 2014, A&A, 570, A13
Markwardt C. B., Tueller J., Skinner G. K., Gehrels N., Barthelmy S. D., Mushotzky R. F., 2005, The ApJL, 633, L77
Martín S., et al., 2016, A&A, 590, A25
Martini P., Weinberg D. H., 2001, ApJ, 547, 12
Massaro E., Giommi P., Leto C., Marchegiani P., Maselli A., Perri M., Piranomonte S., Sclavi S., 2009, A&A, 495, 691
Mateos S., et al., 2012, MNRAS, 426, 3271
Merloni A., et al., 2012, arXiv e-prints, p. arXiv:1209.3114
Montero-Dorta A. D., Prada F., 2009, MNRAS, 399, 1106
Netzer H., 2015, ARA&A, 53, 365
Padovani P., 2016, A&ARv, 24, 13
Paggi A., et al., 2017, ApJ, 841, 44
Palanque-Delabrouille N., et al., 2013, A&A, 551, A29
Pavlinsky M., et al., 2011, Society of Photo-Optical Instrumentation Engineers (SPIE) Conference Series, 8147, 814706
Pavlinsky M., et al., 2018, Space Telescopes and Instrumentation 2018: Ultraviolet to Gamma Ray, 10699, 106991Y
Predehl P., et al., 2010, Space Telescopes and Instrumentation 2010: Ultraviolet to Gamma Ray, 7732, 77320U
Reid B., et al., 2016, MNRAS, 455, 1553
Ricci C., Ueda Y., Koss M. J., Trakhtenbrot B., Bauer F. E., Gandhi P., 2015, The ApJL, 815, L13
Ricci C., et al., 2017, ApJSS, 233, 17
Riffel R. A., et al., 2018, MNRAS, 474, 1373
Roche P. F., Alonso-Herrero A., Gonzalez-Martin O., 2015, MNRAS, 449, 2598
Sakamoto K., Aalto S., Costagliola F., Martín S., Ohyama Y., Wiedner M. C., Wilner D. J., 2013, ApJ, 764, 42
Sakamoto K., et al., 2017, ApJ, 849, 14
Sarkar S., Pandey B., Khatri R., 2019, MNRAS, 483, 2453
Satyapal S., Abel N. P., Secrest N. J., 2018, ApJ, 858, 38
Schmitt H. R., Antonucci R. R. J., Ulvestad J. S., Kinney A. L., Clarke C. J., Pringle J. E., 2001, ApJ, 555, 663
Shankar F., Lapi A., Salucci P., De Zotti G., Danese L., 2006, ApJ, 643, 14
Shankar F., Weinberg D. H., Miralda-Escudé J., 2009, ApJ, 690, 20
Shankar F., et al., 2016, MNRAS, 460, 3119
Shankar F., et al., 2019, Nature Astronomy
Singh V., Risaliti G., Braito V., Shastri P., 2012, MNRAS, 419, 2089
Skrutskie M. F., et al., 2006, AJ, 131, 1163
Stalevski M., Ricci C., Ueda Y., Lira P., Fritz J., Baes M., 2016, MNRAS, 458, 2288
StasiÅĎska G., Vale Asari N., Cid Fernandes R., Gomes J. M., Schlickmann M., Mateus A., Schoenell W., Sodré L., 2008, MNRAS, 391, L29
Steer I., et al., 2017, AJ, 153, 37
Stern D., et al., 2012, ApJ, 753, 30
Tadhunter C., 2016, A&ARv, 24, 10
Taylor M. B., 2005, in Astronomical Data Analysis Software and Systems XIV. p. 29, `http://adsabs.harvard.edu/abs/2005ASPC..347...29T`
Teng S. H., et al., 2015, ApJ, 814, 56
Tueller J., Mushotzky R. F., Barthelmy S., Cannizzo J. K., Gehrels N., Markwardt C. B., Skinner G. K., Winter L. M., 2008, ApJ, 681, 113
Ueda Y., Akiyama M., Ohta K., Miyaji T., 2003, ApJ, 598, 886
Ueda Y., Akiyama M., Hasinger G., Miyaji T., Watson M. G., 2014, ApJ, 786, 104
Varenius E., Conway J. E., Martí-Vidal I., Aalto S., Beswick R., Costagliola F., Klöckner H.-R., 2014, A&A, 566, A15
Vasudevan R. V., Fabian A. C., 2007, MNRAS, 381, 1235
Véron-Cetty M.-P., Véron P., 2010, A&A, 518, 10
Wen X.-Q., Wu H., Zhu Y.-N., Lam M. I., Wu C.-J., Wicker J., Zhao Y.-H., 2013, MNRAS, 433, 2946
Wenger M., et al., 2000, A&A Supplement Series, 143, 9
Wright E. L., et al., 2010, AJ, 140, 1868
Yan R., Blanton M. R., 2012, ApJ, 747, 61
Yoast-Hull T. M., Gallagher III J. S., Aalto S., Varenius E., 2017, MNRAS, 469, L89
Zaw I., Chen Y.-P., Farrar G. R., 2019, ApJ, 872, 134

Table 1. LASr-GPS

Name (1)	Origin (2)	in 2MRS (3)	known AGN (4)	starburst (5)	RA [°] (6)	DEC [°] (7)	z (8)	z Flag (9)	D [Mpc] (10)	No Nucleus (11)	*W1* [mag] (12)	*W2* [mag] (13)	*W3* [mag] (14)	*W4* [mag] (15)	*W1-W2* [mag] (16)	*W2-W3* [mag] (17)	log *L* (*W1*) [erg/s] (18)	log *L* (*W3*) [erg/s] (19)
2dFGRS S805Z417	NED	False	False	False	0.00162	-56.14106	0.01010	0	45.0	False	15.98	15.92	≥12.56	≥9.00	0.07	3.36	40.4	≤40.3
UGC 12889	NED	True	False	False	0.00696	47.27479	0.01673	0	75.0	False	11.07	11.13	9.04	7.03	-0.05	2.09	42.8	42.1
KUG 2357+156	NED	False	False	False	0.00905	15.88188	0.02002	0	89.9	False	12.18	12.09	8.11	6.02	0.09	3.98	42.6	42.7
SDSS J000003.22-010646.9	NED	False	False	False	0.01342	-1.11303	0.02178	0	98.0	True	15.41	15.11	≥11.98	≥8.88	0.30	3.13	41.3	≤41.2
KUG 2357+228	NED	False	False	False	0.01464	23.08753	0.01488	0	66.6	False	14.77	14.69	≥11.81	≥8.62	0.08	2.88	41.3	≤40.9
MCG -01-01-016	NED	True	False	False	0.03600	-6.37400	0.02179	0	98.0	False	11.95	11.90	8.53	6.66	0.04	3.37	42.7	42.6
MCG -01-01-017	NED	True	True	False	0.04708	-5.15875	0.01898	0	85.2	False	12.43	12.45	9.40	7.46	-0.02	3.05	42.4	42.1
2MASX J00001215+0205503	NED	False	False	False	0.05067	2.09742	0.02170	0	97.6	False	12.01	11.75	7.67	4.57	0.26	4.09	42.7	42.9
CGCG 548-023	NED	True	False	True	0.05404	46.96514	0.01790	0	80.3	False	11.29	11.13	8.60	6.33	0.16	2.54	42.8	42.4
CGCG 498-057	NED	False	False	False	0.05542	33.13417	0.01684	0	75.5	False	12.12	12.00	9.05	7.05	0.12	2.95	42.4	42.1
2MFGC 00003	NED	False	False	False	0.05975	70.03300	0.01530	0	68.5	False	11.80	11.57	7.50	5.59	0.23	4.07	42.5	42.7
GALEXASC J000017.22+272403.0	NED	False	False	False	0.07208	27.40083	0.01552	0	69.5	False	15.18	14.95	≥12.02	8.97	0.22	2.93	41.1	≤40.9
GALEXASC J000019.31-315611.3	NED	False	False	False	0.08050	-31.93667	0.01230	0	54.9	False	15.42	15.06	12.30	≥9.07	0.36	2.76	40.8	40.6
FAIRALL 1061	NED	True	False	False	0.09838	-47.01881	0.01998	0	89.8	False	11.04	11.12	10.54	≥8.51	-0.08	0.58	43.0	41.7
2MASX J00002482-0451473	NED	False	False	False	0.10351	-4.86313	0.01892	0	85.0	False	13.10	13.17	≥11.48	≥7.97	-0.06	1.69	42.1	≤41.3
UGC 12893	NED	False	False	False	0.11638	17.21869	0.00367	0	16.3	False	14.95	15.00	≥12.58	≥8.22	-0.05	2.42	40.0	≤39.4
LEDA 089491	NED	False	False	False	0.12167	-60.68076	0.02210	0	99.5	False	14.64	14.44	10.91	7.58	0.20	3.53	41.7	41.6
ESO 293- G 027	NED	False	False	False	0.12283	-40.48447	0.01061	0	47.3	False	12.60	12.58	9.42	7.22	0.02	3.15	41.8	41.6
KUG 2357+225	NED	False	False	False	0.13946	22.77844	0.02020	0	90.8	False	13.20	13.03	9.43	6.73	0.18	3.59	42.1	42.1
UGC 12898	NED	False	False	False	0.15600	33.60127	0.01594	0	71.4	False	15.08	14.88	12.39	≥8.22	0.20	2.48	41.2	40.7
2dFGRS S357Z026	NED	False	False	False	0.19546	-30.64639	0.01428	0	63.9	False	16.00	16.07	≥12.63	≥8.86	-0.08	3.45	40.7	≤40.6
ESO 193- G 009	NED	True	False	False	0.22192	-47.35681	0.01972	0	88.6	False	11.28	11.31	9.28	7.85	-0.03	2.03	42.9	42.2
APMUKS(BJ) B235824.83-412603.8	NED	False	False	False	0.24577	-41.15485	0.00050	0	2.2	True	17.39	17.05	≥12.66	≥9.24	0.33	4.39	37.3	≤37.6
NGC 7802	NED	True	False	False	0.25175	6.24206	0.01776	0	79.7	False	10.46	10.48	9.54	7.66	-0.02	0.94	43.1	42.0
SDSS J000103.59+143448.6	NED	False	False	True	0.26500	14.58018	0.00573	0	25.5	False	15.58	15.40	≥11.98	≥8.54	0.18	3.42	40.1	≤40.0
GALEXASC J000109.10-162721.7	NED	False	False	False	0.28813	-16.45619	0.01574	0	70.5	False	15.34	15.27	≥11.99	≥8.68	0.07	3.28	41.1	≤40.9
KUG 2358+128A	NED	False	False	False	0.30575	13.14406	0.01830	0	82.1	False	13.13	13.05	9.65	7.12	0.08	3.40	42.1	42.0
MCG +02-01-010	NED	False	False	False	0.31238	13.11256	0.01873	0	84.1	False	14.20	14.06	11.02	≥8.36	0.14	3.04	41.7	41.4
IC 5376	NED	True	True	False	0.33237	34.52572	0.01678	0	75.2	False	10.95	11.00	8.95	7.28	-0.05	2.05	42.9	42.2
NGC 7803	NED	True	False	False	0.33321	13.11125	0.01790	0	80.3	False	10.27	10.17	6.92	4.48	0.11	3.25	43.2	43.0
2MASX J00012334+4733537	NED	True	True	False	0.34764	47.56505	0.01747	0	78.3	False	11.77	11.18	7.76	5.19	0.59	3.42	42.6	42.7
MRK 0934	NED	False	False	False	0.35850	13.11300	0.01753	0	78.6	False	12.59	12.44	8.65	6.25	0.15	3.80	42.3	42.3
NGC 7805	NED	True	False	False	0.36154	31.43375	0.01605	0	71.9	False	10.55	10.61	10.13	8.89	-0.06	0.49	43.0	41.7
UGC 12910	NED	False	False	False	0.36833	5.38944	0.01317	0	58.9	False	15.48	15.08	12.02	≥8.38	0.40	3.06	40.9	40.7
NGC 7806	NED	True	False	False	0.37521	31.44186	0.01590	0	71.2	False	10.82	10.80	8.62	6.89	0.03	2.17	42.9	42.2
CGCG 433-016	NED	False	False	True	0.39146	15.08156	0.02119	0	95.3	False	14.25	14.03	10.20	7.52	0.22	3.82	41.8	41.9
UGC 12913	NED	False	False	False	0.40292	3.50558	0.02115	0	95.1	False	14.21	14.05	11.32	≥8.47	0.16	2.73	41.8	41.4
GALEXASC J000137.80+172918.9	NED	False	False	False	0.40708	17.48861	0.02151	0	96.7	False	16.50	16.43	≥12.50	≥9.01	0.06	3.94	40.9	≤41.0
UGC 12914	NED	True	True	False	0.40967	23.48364	0.01458	0	65.2	False	10.28	10.25	7.78	5.34	0.03	2.47	43.0	42.5
AGC 748776	SIMBAD	False	False	False	0.42229	13.84256	0.02112	0	95.0	False	15.27	14.95	≥12.17	≥8.80	0.33	2.78	41.4	≤41.1

Abridged. Full table available online in digitial format.

– *Notes:* (1) object name, mostly following NED nomenclature; (2) origin of object with preference to NED if available; (3) flag whether the galaxy is in 2MRS; (4) and (5) flag whether galaxy is known to host an AGN or starburst, respectively; (6) and (7) equatorial coordinates of the object centre in J2000 in degrees; (8) redshift; (9) redshift confidence flag: 0 means that the value is robust, 1 means that the value is not robust but there is no reason to doubt, and 2 means that the redshift is controversial; (10) object distance in Mpc; (11) No nucleus flag: If true, the source does not show any clear centre or nucleus in the optical/infrared images; (12), (13), (14), and (15) *WISE* profile-fitting photometric magnitudes; (16) and (17) *WISE W1-W2* and *W2-W3* colours; (18) and (19) observed *W1* and *W3* continuum luminosities , calculated from the selected distance and the profile-fitting magnitudes.

Table 2: known AGN selected by R90

Name (1)	in 2MRS (2)	Seyfert (3)	Sy 1 (4)	Sy 2 (5)	LINER (6)	H II (7)	starburst (8)	RA [°] (9)	DEC [°] (10)	z (11)	D [Mpc] (12)	*W1-W2* [mag] (13)	*W2-W3* [mag] (14)	log L (*W1*) [erg/s] (15)	log L (*W3*) [erg/s] (16)	log L^{nuc} (12 μm) [erg/s] (17)	log L^{int} (2-10 keV) [erg/s] (18)	S18 (19)
UGC 00006	True	True	True	True	False	True	False	0.79009	21.96016	0.02195	98.7	0.81	3.51	43.6	43.8	43.58±0.57	…	True
MCG -01-01-069	True	True	True	False	False	True	False	4.36917	-3.23050	0.02129	95.8	1.68	3.02	42.8	43.2	42.81±0.57	…	True
2MASX J00193596-0440105	True	True	False	True	True	False	False	4.89999	-4.66957	0.02052	92.2	1.02	3.16	43.4	43.6	43.21±0.57	…	True
2MASX J00253292+6821442	False	True	False	True	False	False	False	6.38696	68.36228	0.01200	53.6	0.68	3.09	42.9	42.9	42.62±0.22	43.2	True
ESO 350-IG 038	False	False	False	False	False	True	False	9.21958	-33.55472	0.02060	92.6	1.34	4.46	43.2	44.0	43.39±0.23	…	False
NGC 0253	True	True	False	True	False	True	True	11.88800	-25.28822	0.00081	3.2	0.73	4.94	42.2	43.0	≤41.50	39.7	False
NGC 0262	True	True	True	True	False	False	False	12.19642	31.95697	0.01502	67.2	1.21	3.11	43.4	43.6	43.45±0.22	43.5	True
IC 1623B	True	True	True	False	False	True	False	16.94817	-17.50697	0.02025	91.0	1.24	3.85	43.6	44.1	43.92±0.57	…	True
NGC 0424	True	True	True	True	False	False	False	17.86511	-38.08347	0.01178	52.6	1.22	2.83	43.7	43.8	43.78±0.11	43.8	True
NGC 0454 NED02	True	True	False	True	False	False	False	18.60387	-55.39708	0.01213	54.2	0.70	2.88	43.1	43.0	43.08±0.09	42.2	True
NGC 0449	True	True	False	True	False	False	False	19.03020	33.08956	0.01595	71.4	1.31	4.10	42.8	43.4	43.23±0.22	…	True
MCG +08-03-018	True	False	False	False	False	False	False	20.64346	50.05500	0.02040	91.7	1.21	3.83	43.0	43.5	43.25±0.57	44.0	True
NGC 0526A	True	True	True	True	False	False	False	20.97664	-35.06553	0.01897	85.2	0.79	2.52	43.7	43.5	43.71±0.05	43.3	True
UGC 01032	True	True	True	False	False	False	False	21.88563	19.17883	0.01739	78.0	0.72	3.25	43.2	43.3	43.10±0.22	42.7	True
ESO 543- G 008	False	False	False	False	False	False	False	24.83504	-20.45306	0.02122	95.4	0.98	3.49	42.9	43.1	42.76±0.57	…	True
NGC 0660	True	True	False	True	True	True	False	25.76000	13.64506	0.00286	13.4	1.15	3.33	42.6	42.8	42.43±0.57	…	True
UGC 01214	True	True	True	True	False	False	False	25.99084	2.34990	0.01718	77.0	1.13	3.65	43.3	43.7	43.58±0.07	43.2	True
2MASX J01500266-0725482	False	True	True	True	False	False	False	27.51124	-7.43014	0.01803	80.9	1.34	4.24	42.8	43.5	43.35±0.22	…	True
NGC 0788	True	True	True	True	False	False	False	30.27686	-6.81552	0.01360	60.8	0.78	3.17	43.2	43.2	43.17±0.05	43.0	True
ESO 246- G 004	True	True	True	False	False	False	False	33.98746	-45.60003	0.02131	95.8	1.04	2.76	43.0	43.0	42.79±0.22	…	True
MRK 1044	True	True	True	False	False	False	False	37.52302	-8.99814	0.01611	72.2	0.83	2.74	43.4	43.3	43.06±0.22	42.5	True
MESSIER 077	True	True	True	True	False	False	False	40.66963	-0.01328	0.00379	10.5	1.13	3.61	43.9	44.3	43.58±0.07	42.5	True
MRK 1058	True	True	False	True	False	False	False	42.46596	34.98799	0.01714	76.8	0.69	3.45	43.0	43.1	42.87±0.22	…	True
SWIFT J0250.2+4650	False	True	False	True	False	False	False	42.61325	46.79150	0.02120	95.3	1.04	3.16	42.6	42.8	42.54±0.22	42.9	True
NGC 1125	True	True	True	True	False	False	False	42.91850	-16.65067	0.01102	49.2	0.68	3.78	42.7	43.0	42.78±0.22	42.8	True
MCG -02-08-014	True	True	False	True	False	True	False	43.09748	-8.51041	0.01675	75.1	0.94	2.50	43.0	42.9	42.87±0.08	42.9	True
UGC 02456	True	True	False	True	False	False	False	44.99413	36.82063	0.01202	53.7	0.81	4.05	43.1	43.5	43.38±0.22	…	True
NGC 1194	True	True	True	True	False	False	False	45.95462	-1.10374	0.01361	60.9	1.31	2.97	43.2	43.4	43.49±0.04	43.7	True
NGC 1275	True	True	True	True	False	False	False	49.95067	41.51170	0.01756	78.8	1.01	4.01	43.7	44.2	44.23±0.04	44.0	True
NGC 1320	True	True	False	True	False	False	False	51.20292	-3.04228	0.00923	37.7	0.92	3.55	42.9	43.1	42.91±0.22	…	True
ESO 116- G 018	True	True	False	True	False	False	False	51.22104	-60.73844	0.01850	83.0	0.95	3.55	43.3	43.6	43.41±0.22	…	True
NGC 1365	True	True	True	True	False	True	False	53.40155	-36.14040	0.00550	17.8	0.76	3.89	42.9	43.3	42.53±0.04	42.1	True
NGC 1386	True	True	True	True	False	False	False	54.19242	-35.99939	0.00290	16.2	0.85	3.45	42.4	42.6	42.37±0.08	42.0	True
ESO 548- G 081	True	True	True	False	False	False	False	55.51529	-21.24426	0.01447	64.7	0.71	1.99	43.6	43.2	43.04±0.16	43.0	True
ESO 420- G 013	True	True	False	True	True	True	False	63.45704	-32.00697	0.01195	53.4	0.97	3.86	43.2	43.6	43.21±0.08	…	True
2MASX J04282604-0433496	False	True	False	True	True	False	False	67.10854	-4.56375	0.01572	70.4	0.86	5.30	42.4	43.3	42.91±0.57	…	False
2MASX J04344151+4014219	True	True	True	False	False	False	False	68.67304	40.23939	0.02048	92.1	0.73	3.25	43.5	43.6	43.44±0.22	…	True
2MASX J04405494-0822221	True	True	True	True	False	False	False	70.22902	-8.37284	0.01517	67.9	1.53	3.13	43.4	43.8	43.61±0.22	…	True
UGC 03142	True	True	True	False	False	False	False	70.94496	28.97192	0.02168	97.5	0.80	2.98	43.3	43.3	43.08±0.22	43.3	True
UGC 03157	True	True	False	True	False	False	False	71.62363	18.46089	0.01541	69.0	0.71	3.44	43.1	43.3	43.06±0.22	42.9	True
2MASX J04524451-0312571	True	True	True	True	False	False	False	73.18529	-3.21593	0.01569	70.3	0.89	4.32	42.7	43.3	43.08±0.22	…	True
ESO 033- G 002	True	True	False	True	False	False	False	73.99567	-75.54117	0.01826	82.0	0.94	3.14	43.5	43.6	43.54±0.14	42.2	True
CGCG 468-002 NED02	True	True	True	False	False	False	False	77.08837	17.36894	0.01684	75.5	0.76	4.42	42.7	43.3	43.08±0.22	…	False
GALEXASC J051045.55+162958.9	False	True	True	False	False	False	False	77.68962	16.49885	0.01788	80.2	1.05	3.50	43.4	43.7	43.55±0.22	43.6	True
2MFGC 04298	True	True	False	True	False	False	False	79.09471	19.45311	0.01875	84.2	0.91	2.98	43.0	43.0	42.81±0.22	42.4	True
ESO 362- G 018	True	True	True	True	False	False	False	79.89916	-32.65758	0.01258	56.2	0.69	3.51	43.1	43.2	43.17±0.05	43.0	True
2MASX J05353211+4011152	False	True	True	False	False	False	False	83.88385	40.18770	0.02083	93.6	0.96	3.56	43.0	43.3	43.08±0.22	42.4	True
NGC 2110	True	True	True	True	True	False	False	88.04742	-7.45621	0.00780	35.6	0.78	2.62	43.3	43.2	43.08±0.06	42.7	True
2MASX J05523323-1122290	True	True	False	True	False	False	False	88.13837	-11.37478	0.02189	98.5	1.17	3.75	43.1	43.6	43.42±0.22	…	True
UGC 03374	True	True	True	False	False	False	False	88.72338	46.43934	0.02048	92.1	1.02	2.95	44.1	44.2	44.06±0.22	43.8	True
UGC 03426	True	True	True	True	False	False	False	93.90152	71.03753	0.01350	60.4	0.87	…	43.4	…	43.69±0.10	43.7	True
2MASX J06230531-0607132	True	True	False	True	False	False	False	95.77217	-6.12036	0.02015	90.6	0.84	4.33	43.0	43.5	43.34±0.22	…	False
UGC 03478	True	True	True	False	False	False	False	98.19654	63.67367	0.01278	57.1	0.68	2.82	43.1	43.0	42.76±0.22	42.5	True
UVQS J064939.21+261109.0	False	False	False	False	False	False	False	102.41337	26.18583	0.01700	76.2	0.73	4.95	41.5	42.3	41.76±0.57	…	False
NGC 2273	True	True	True	True	False	False	False	102.53607	60.84581	0.00614	30.2	0.69	3.69	42.8	43.0	42.78±0.22	…	True
IC 0450	True	True	True	True	False	False	False	103.05105	74.42707	0.01881	84.4	0.79	2.42	44.0	43.8	43.62±0.22	43.1	True

Table 2: continued.

Name	in 2MRS	Seyfert	Sy 1	Sy 2	LINER	H II	starburst	RA [°]	DEC [°]	z	D [Mpc]	*W1-W2* [mag]	*W2-W3* [mag]	log L (*W1*) [erg/s]	log L (*W3*) [erg/s]	log L^{nuc} (12 μm) [erg/s]	log L^{int} (2-10 keV) [erg/s]	S18
(1)	(2)	(3)	(4)	(5)	(6)	(7)	(8)	(9)	(10)	(11)	(12)	(13)	(14)	(15)	(16)	(17)	(18)	(19)
CGCG 234-021	True	True	False	True	False	False	False	103.15412	45.78064	0.02184	98.3	0.75	3.90	43.1	43.5	43.30±0.22	…	True
UGC 03752	True	True	False	True	False	False	False	108.51608	35.27928	0.01569	70.3	0.90	3.28	43.4	43.6	43.39±0.22	43.1	True
2MASX J07170726-3254197	True	True	True	False	False	False	False	109.28017	-32.90542	0.00772	34.4	0.97	2.90	42.5	42.5	42.22±0.22	…	True
CGCG 147-020	True	False	False	False	False	False	False	111.40569	29.95411	0.01885	84.6	1.15	3.31	43.1	43.4	43.08±0.57	43.3	True
UGC 03901	True	True	True	False	False	False	False	113.47120	49.29183	0.02048	92.0	0.74	3.28	42.9	43.0	42.78±0.22	…	True
UGC 03995B	True	True	False	True	False	False	False	116.03803	29.24740	0.01597	71.5	0.85	2.94	43.4	43.4	43.19±0.22	42.5	True
IC 2207	True	True	False	True	False	True	False	117.46204	33.96228	0.01602	71.8	0.75	2.51	43.1	42.8	42.41±0.57	…	True
UGC 04145	True	True	True	True	False	False	False	119.91716	15.38682	0.01552	69.5	0.68	3.77	43.3	43.5	43.36±0.22	…	True
Phoenix Galaxy	True	True	True	True	False	False	False	121.02441	5.11385	0.01350	60.3	1.39	3.98	43.1	43.7	43.55±0.22	43.2	True
MCG -02-22-003	True	True	False	True	False	False	False	125.38975	-13.35114	0.01436	64.2	0.74	3.19	42.7	42.8	42.51±0.22	…	True
FAIRALL 0272	True	True	False	True	False	False	False	125.75458	-4.93486	0.02182	98.2	0.98	2.88	43.3	43.3	43.12±0.22	43.1	True
CGCG 032-017	False	False	False	False	False	True	True	125.89518	3.22101	0.00978	43.6	0.81	5.05	41.0	41.8	40.68±0.23	…	False
ESO 018- G 009	True	True	False	True	False	False	False	126.03288	-77.78258	0.01762	79.0	1.24	3.87	42.9	43.4	43.25±0.22	…	True
MRK 0093	False	True	False	True	False	True	True	129.17642	66.23292	0.01783	80.0	0.79	4.65	42.5	43.1	42.79±0.57	…	False
NGC 2623	True	True	True	True	True	False	False	129.60032	25.75464	0.01818	81.6	0.76	4.22	43.1	43.6	43.55±0.20	…	True
ARP 007	True	True	True	False	False	True	False	132.58433	-16.57947	0.01860	83.5	0.65	3.69	42.9	43.1	42.78±0.57	…	True
MCG -01-24-012	True	True	True	True	False	False	False	140.19271	-8.05614	0.01968	88.4	1.13	3.47	43.0	43.3	43.41±0.04	43.3	True
CGCG 122-055	True	True	True	False	False	False	False	145.51997	23.68526	0.02130	95.8	0.78	3.58	43.1	43.3	43.12±0.22	42.5	True
ESO 434- G 040	True	True	True	True	False	False	False	146.91732	-30.94873	0.00849	37.8	1.00	3.25	43.3	43.4	43.48±0.04	43.2	True
MRK 1239	True	True	True	False	False	False	False	148.07959	-1.61207	0.01960	88.0	1.05	2.70	44.2	44.2	44.12±0.07	43.2	True
NGC 3094	True	True	False	True	False	False	False	150.35809	15.77007	0.00802	38.5	1.66	2.57	43.3	43.5	43.66±0.04	…	True
WN 1	False	True	True	False	False	False	False	150.50023	-8.16157	0.01524	68.2	0.72	3.97	41.8	42.2	41.85±0.22	…	True
CGCG 064-055	True	True	True	True	False	False	False	151.46330	12.96130	0.00937	41.8	1.22	3.52	42.4	42.7	42.48±0.22	…	True
NGC 3227	True	True	True	True	False	False	False	155.87741	19.86505	0.00386	20.6	0.71	3.47	42.7	42.8	42.41±0.10	42.3	True
CGCG 009-034	True	True	True	True	False	False	False	156.58807	0.68493	0.02150	96.7	0.95	3.29	43.2	43.3	43.13±0.22	…	True
NGC 3256	True	True	False	True	False	True	True	156.96362	-43.90375	0.00941	37.4	0.79	4.75	43.3	44.0	43.81±0.57	…	False
ESO 317- G 041	True	False	False	False	False	False	False	157.84633	-42.06061	0.01932	86.8	0.87	3.36	43.4	43.6	43.31±0.57	43.3	True
UGC 05713	True	True	False	True	False	False	False	157.91206	25.98392	0.02101	94.5	0.88	3.04	43.1	43.2	42.98±0.22	…	True
NGC 3281	True	True	False	True	False	False	False	157.96704	-34.85369	0.01067	47.6	1.46	3.36	43.3	43.7	43.52±0.04	43.1	True
ESO 568- G 021	True	True	True	True	False	False	False	160.31317	-21.02300	0.01209	54.0	0.72	3.15	42.2	42.2	41.90±0.22	…	True
NGC 3516	True	True	True	False	False	False	False	166.69788	72.56858	0.00883	51.0	0.74	2.83	43.5	43.4	43.22±0.22	43.0	True
IRAS 11215-2806	True	True	False	True	False	False	False	171.01137	-28.38767	0.01376	61.5	1.52	3.61	42.7	43.2	43.00±0.22	…	True
MRK 0040	False	True	True	False	False	False	False	171.40066	54.38255	0.02069	93.0	0.80	2.45	43.1	42.9	42.67±0.22	43.0	True
NGC 3690 NED02	False	False	False	False	False	True	True	172.14004	58.56292	0.01046	46.6	1.03	4.66	43.1	43.9	43.26±0.19	39.7	False
NGC 3783	True	True	True	False	False	False	False	174.75734	-37.73867	0.00970	47.8	1.01	3.18	43.5	43.7	43.67±0.03	43.5	True
CGCG 068-036	True	True	True	True	False	False	False	175.57032	14.06660	0.02074	93.2	1.01	3.54	42.9	43.2	43.03±0.22	…	True
UGC 06728	True	True	True	False	False	False	False	176.31676	79.68151	0.00652	29.0	0.71	2.72	42.2	42.1	41.73±0.22	41.8	True
NGC 4051	True	True	True	False	False	False	False	180.79006	44.53133	0.00233	13.3	0.91	3.39	42.2	42.4	42.39±0.04	41.6	True
NGC 4151	True	True	True	False	False	False	False	182.63574	39.40573	0.00331	5.4	0.82	2.72	42.3	42.2	42.05±0.07	41.5	True
NGC 4253	True	True	True	False	False	False	False	184.61046	29.81287	0.01271	56.8	0.91	3.51	43.3	43.5	43.33±0.22	42.7	True
TOLOLO 1220+051	False	True	False	True	False	True	True	185.81890	4.83614	0.01784	80.0	0.82	4.55	41.1	41.7	41.07±0.57	…	False
NGC 4388	True	True	True	True	False	False	False	186.44478	12.66209	0.00849	18.1	1.01	3.42	42.4	42.7	42.26±0.07	42.4	True
NGC 4395	True	True	True	True	True	False	True	186.45359	33.54693	0.00106	4.3	0.79	3.23	39.7	39.8	39.72±0.08	40.4	True
NGC 4355	True	True	False	True	True	False	False	186.72758	-0.87761	0.00708	23.6	1.26	5.62	42.0	43.2	43.38±0.05	…	False
NGC 4507	True	True	True	True	False	False	False	188.90263	-39.90926	0.01180	52.7	1.08	3.16	43.5	43.7	43.71±0.04	43.5	True
IC 3599	False	True	True	True	False	True	False	189.42168	26.70766	0.02076	93.3	0.97	2.69	43.1	43.0	42.60±0.57	…	True
NGC 4593	True	True	True	False	False	False	False	189.91427	-5.34426	0.00900	31.9	0.74	3.01	43.0	42.9	42.84±0.07	42.6	True
IC 3639	True	True	True	True	False	False	False	190.22022	-36.75586	0.01098	49.0	0.87	4.27	43.0	43.5	43.44±0.04	43.7	True
NGC 4628	True	True	False	True	False	False	False	190.60525	-6.97100	0.00943	44.8	0.79	3.50	42.9	43.1	42.90±0.22	…	True
2MASX J12423600+7807203	True	True	True	True	False	False	False	190.65014	78.12230	0.02210	99.4	0.72	3.13	43.1	43.2	42.94±0.22	…	True
NGC 4945	True	True	False	True	False	False	False	196.36449	-49.46821	0.00188	3.8	1.27	3.88	41.6	42.1	39.99±0.12	41.4	True
ESO 323- G 077	True	True	True	True	False	False	False	196.60885	-40.41467	0.01501	67.2	0.83	2.72	44.0	43.9	43.67±0.09	42.9	True
NGC 4968	True	True	False	True	False	False	False	196.77492	-23.67703	0.00985	43.9	0.89	4.00	42.8	43.2	43.03±0.22	…	True
2MASX J13084201-2422581	False	True	False	True	False	False	False	197.17529	-24.38308	0.01400	62.6	1.20	4.51	42.5	43.2	43.03±0.22	…	False
2MASX J13201354+0754279	False	True	False	True	False	False	False	200.05655	7.90781	0.02169	97.6	0.71	3.39	42.4	42.6	42.29±0.22	…	True
MCG -03-34-064	True	True	True	True	False	False	False	200.60190	-16.72846	0.01692	75.8	1.43	3.90	43.5	44.1	43.96±0.05	43.5	True
NGC 5135	True	True	True	True	False	True	False	201.43358	-29.83367	0.01371	61.3	0.73	3.94	43.4	43.8	43.17±0.08	43.1	True

Table 2: continued.

Name (1)	in 2MRS (2)	Seyfert (3)	Sy 1 (4)	Sy 2 (5)	LINER (6)	H II (7)	starburst (8)	RA [°] (9)	DEC [°] (10)	z (11)	D [Mpc] (12)	*W1*-*W2* [mag] (13)	*W2*-*W3* [mag] (14)	log L (*W1*) [erg/s] (15)	log L (*W3*) [erg/s] (16)	log L^{nuc} (12 μm) [erg/s] (17)	log L^{int} (2-10 keV) [erg/s] (18)	S18 (19)
ESO 383- G 018	True	True	True	True	False	True	False	203.35875	-34.01478	0.01285	57.4	1.31	3.07	43.2	43.4	43.12±0.57	42.8	True
ESO 383- G 035	True	True	True	False	False	False	False	203.97378	-34.29554	0.00758	33.7	0.92	2.83	43.1	43.1	43.06±0.07	42.8	True
UM 595	False	True	True	False	False	True	True	204.56407	-0.39855	0.02204	99.2	0.85	3.71	42.0	42.3	41.81±0.57	…	True
MRK 0796	True	True	False	True	False	True	True	206.70605	14.40047	0.02156	97.0	0.91	3.69	43.4	43.7	43.42±0.57	…	True
2MASS J13473599-6037037	False	True	True	False	False	False	False	206.89981	-60.61772	0.01290	57.7	1.07	2.95	43.3	43.4	43.25±0.22	43.3	True
IC 4329A	True	True	True	False	False	False	False	207.33028	-30.30944	0.01613	72.3	1.09	2.83	44.2	44.2	44.26±0.04	43.9	True
2MASX J13512953-1813468	True	True	True	False	False	False	False	207.87292	-18.22972	0.01222	54.6	0.68	2.07	42.8	42.3	42.03±0.22	42.6	True
NGC 5347	True	True	True	True	False	False	False	208.32431	33.49083	0.00790	21.2	1.05	3.83	42.1	42.5	42.57±0.04	42.1	True
CGCG 074-129	True	True	True	True	True	False	False	212.67229	13.55800	0.01622	72.7	0.94	4.12	42.8	43.3	42.91±0.57	…	True
Circinus Galaxy	False	True	True	True	False	False	False	213.29146	-65.33922	0.00145	4.2	0.79	3.80	43.1	43.4	42.64±0.05	42.3	True
NGC 5506	True	True	True	True	False	False	False	213.31205	-3.20758	0.00618	24.7	1.16	2.49	43.4	43.3	43.20±0.03	42.9	True
NGC 5548	True	True	True	False	False	False	False	214.49806	25.13679	0.01672	75.0	0.81	2.80	43.6	43.5	43.32±0.21	43.1	True
NGC 5610	True	True	True	True	False	False	True	216.09558	24.61413	0.01689	75.7	0.73	3.51	43.2	43.4	43.06±0.57	42.7	True
2MASX J14320869-2704324	True	True	True	False	False	False	False	218.03625	-27.07561	0.01443	64.6	0.78	3.44	42.7	42.8	42.59±0.22	…	True
NGC 5643	True	True	True	True	False	False	False	218.16977	-44.17441	0.00400	10.4	0.65	3.99	41.8	42.1	41.92±0.10	42.0	True
MRK 1388	True	True	True	True	False	False	False	222.65772	22.73434	0.02095	94.2	1.13	3.42	43.1	43.4	43.25±0.22	…	True
WKK 4438	True	True	True	False	False	False	False	223.82254	-51.57083	0.01600	71.7	0.82	3.35	43.1	43.3	43.06±0.22	42.8	True
IC 4518A	False	True	False	True	False	False	False	224.42158	-43.13211	0.01630	73.0	1.23	3.49	43.2	43.6	43.50±0.06	42.7	True
NGC 5861	True	True	False	True	False	True	False	227.31704	-11.32167	0.00624	25.7	1.26	4.01	42.0	42.6	42.08±0.57	…	True
IC 4553	True	True	False	True	True	True	False	233.73856	23.50314	0.01813	81.3	0.75	4.74	43.3	44.0	43.76±0.57	…	False
NGC 5990	True	True	False	True	False	False	True	236.56816	2.41542	0.01228	54.9	0.79	3.44	43.4	43.6	43.29±0.57	…	True
IRAS 15514-3729	True	True	False	True	False	True	False	238.69479	-37.63867	0.01916	86.0	0.79	3.11	43.1	43.2	42.82±0.57	…	True
WKK 6092	True	True	True	False	False	False	False	242.96421	-60.63194	0.01564	70.0	0.72	2.39	43.2	42.9	42.64±0.22	42.4	True
ESO 138- G 001	True	True	False	True	False	False	False	252.83386	-59.23478	0.00914	40.7	1.24	3.48	43.2	43.6	43.58±0.02	44.1	True
ESO 044- G 007	True	True	False	True	False	False	False	258.97996	-73.34211	0.01693	75.9	0.71	3.26	42.6	42.7	42.40±0.22	…	True
NGC 6300	True	True	False	True	False	False	False	259.24779	-62.82056	0.00370	12.6	1.07	3.37	42.1	42.4	42.23±0.08	41.6	True
2MASS J17372838-2908021	False	True	True	False	False	False	False	264.36813	-29.13403	0.02140	96.3	0.78	2.58	43.7	43.6	43.38±0.22	43.9	True
ESO 139- G 012	True	True	False	True	False	False	False	264.41283	-59.94072	0.01702	76.3	0.67	2.63	43.3	43.1	42.85±0.22	42.6	True
IC 4709	True	True	False	True	False	False	False	276.08079	-56.36917	0.01690	75.8	0.90	3.11	43.1	43.1	42.92±0.22	43.1	True
2MASX J18263239+3251300	False	True	False	True	False	False	False	276.63498	32.85834	0.02200	99.0	0.70	2.73	42.9	42.7	42.47±0.22	43.0	True
FAIRALL 0049	True	True	True	True	False	False	False	279.24288	-59.40239	0.02002	90.0	1.03	2.91	44.0	44.1	43.95±0.20	43.4	True
ESO 103- G 035	True	True	True	True	False	False	False	279.58475	-65.42756	0.01330	59.5	1.57	3.75	43.2	43.8	43.71±0.19	43.4	True
ESO 140- G 043	True	True	True	False	False	False	False	281.22492	-62.36483	0.01418	63.4	0.87	2.82	43.7	43.6	43.67±0.04	43.1	True
IC 4769	True	True	False	True	False	False	False	281.93354	-63.15700	0.01512	67.7	0.85	3.87	43.1	43.4	43.26±0.22	…	True
ESO 281- G 038	True	True	True	False	False	False	False	284.08738	-43.14686	0.01667	74.7	0.90	2.51	43.1	43.0	42.75±0.22	…	True
UGC 11397	True	True	False	True	False	False	False	285.95479	33.84469	0.01509	67.6	0.67	2.95	42.9	42.9	42.63±0.22	42.6	True
2MASX J19373299-0613046	True	True	True	False	False	False	False	294.38754	-6.21800	0.01031	46.0	0.83	3.45	43.2	43.4	43.20±0.22	42.8	True
ESO 339- G 011	True	True	False	True	False	False	False	299.40658	-37.93564	0.01947	87.4	0.68	4.32	43.3	43.8	43.65±0.22	…	False
NGC 6860	True	True	True	False	False	False	False	302.19538	-61.10019	0.01525	68.3	0.94	2.50	43.7	43.6	43.46±0.05	43.2	True
2MASX J20183871+4041003	False	True	False	True	False	False	False	304.66133	40.68339	0.01420	63.5	0.81	2.96	43.1	43.1	42.85±0.22	42.6	True
IC 4995	True	True	True	True	False	False	False	304.99571	-52.62197	0.01646	73.8	0.71	3.62	43.0	43.3	43.05±0.22	…	True
MCG +04-48-002	True	True	True	True	False	False	False	307.14608	25.73333	0.01390	62.2	0.69	4.14	43.2	43.6	43.45±0.22	43.2	True
ESO 234- G 050	True	True	True	False	False	True	False	308.99117	-50.19225	0.00877	39.1	0.77	3.50	42.3	42.5	42.04±0.57	41.6	True
IC 5063	True	True	True	True	False	False	False	313.00975	-57.06878	0.01140	50.9	1.30	4.02	43.2	43.8	43.80±0.03	43.1	True
2MASX J21025564+6336248	True	False	False	False	True	True	False	315.73179	63.60686	0.01099	49.1	0.94	2.56	42.7	42.6	41.66±0.23	…	True
IC 1368	True	True	False	True	False	False	False	318.55246	2.17800	0.01305	58.3	0.84	3.62	42.8	43.1	42.83±0.22	…	True
UGC 11717	True	False	False	False	True	False	False	319.64713	19.71813	0.02102	94.5	0.69	2.85	43.3	43.2	42.44±0.23	…	True
4C +50.55	False	True	True	False	False	False	False	321.16354	50.97328	0.02000	89.9	0.89	2.37	43.6	43.4	43.19±0.22	44.0	True
IRAS 21262+5643	False	True	True	False	False	False	False	321.93914	56.94303	0.01440	64.4	0.99	2.81	43.5	43.5	43.33±0.22	43.1	True
NGC 7130	True	True	True	True	True	True	False	327.08133	-34.95124	0.01620	72.6	0.73	4.30	43.3	43.8	43.22±0.08	42.2	False
NGC 7172	True	True	True	True	False	True	False	330.50788	-31.86967	0.00863	33.9	0.84	2.44	43.2	43.0	42.80±0.04	42.7	True
NGC 7314	True	True	True	True	False	False	False	338.94246	-26.05047	0.00477	17.3	0.70	3.09	42.0	42.0	41.74±0.08	42.2	True
NGC 7378	True	True	False	True	False	False	False	341.94875	-11.81664	0.00850	29.6	0.70	2.76	42.1	42.0	41.66±0.22	…	True
NGC 7469	True	True	True	False	False	False	False	345.81510	8.87400	0.01631	73.1	0.79	3.91	43.9	44.2	43.89±0.04	43.2	True
NGC 7479	True	True	True	True	True	False	False	346.23604	12.32289	0.00793	27.7	1.34	3.89	42.5	43.1	43.20±0.06	41.9	True
NGC 7552	True	True	True	False	True	True	False	349.04483	-42.58474	0.00535	11.2	0.79	4.44	42.4	42.9	≤41.41	39.7	False
NGC 7582	True	True	True	True	False	False	False	349.59792	-42.37056	0.00525	22.2	0.93	3.18	43.2	43.3	42.81±0.07	43.5	True

Table 2: continued.

Name	in 2MRS	Seyfert	Sy 1	Sy 2	LINER	H II	starburst	RA [°]	DEC [°]	z	D [Mpc]	*W1-W2* [mag]	*W2-W3* [mag]	log L (*W1*) [erg/s]	log L (*W3*) [erg/s]	log L^{nuc} (12 μm) [erg/s]	log L^{int} (2-10 keV) [erg/s]	S18
(1)	(2)	(3)	(4)	(5)	(6)	(7)	(8)	(9)	(10)	(11)	(12)	(13)	(14)	(15)	(16)	(17)	(18)	(19)
IC 1495	True	True	True	True	False	False	False	352.69892	-13.48544	0.02119	95.3	0.77	3.13	43.1	43.2	42.97±0.22	…	True
IC 1490	True	True	True	False	False	False	False	359.79467	-4.12700	0.01858	83.4	0.75	2.77	43.4	43.3	43.11±0.22	…	True

– *Notes:* (1) object name, mostly following NED nomenclature; (2) flag whether the galaxy is in 2MRS; (3), (4), (5), (6), (7) (8) flags whether galaxy has Seyfert, Sy 1, Sy 2, LINER, H II or starburst classification, respectively; (9) and (10) equatorial coordinates of the object centre in J2000 in degrees; (11) redshift; (12) object distance in Mpc; (13) and (14) *WISE W1-W2* and *W2-W3* colours; (15) and (16) observed *W1* and *W3* continuum luminosities , calculated from the selected distance and the profile-fitting magnitudes. (17) nuclear 12 μm luminosity of the AGN either taken from Asmus et al. (2014), if uncertainty ≤ 0.1 dex, or estimated from $L(W3)$ and optical type (see Sect. 4.1 for details); (18) intrinsic 2-10 keV X-ray luminosity for AGN from the BAT70 sample (Ricci et al. 2017), and from Asmus et al. (2015) otherwise, where available; (19) flag whether the source fulfils the S18 criterion or not (see Sect. 4.4.1 for details);

Table 3: R90 AGN candidates

Name	in 2MRS	H II	starburst	RA [°]	DEC [°]	z	D [Mpc]	*W1-W2* [mag]	*W2-W3* [mag]	log L (*W1*) [erg/s]	log L (*W3*) [erg/s]	log L^{nuc} (12 μm) [erg/s]	S18
(1)	(2)	(3)	(4)	(5)	(6)	(7)	(8)	(9)	(10)	(11)	(12)	(13)	(14)
2MASX J00042025+3120313	False	False	False	1.08440	31.34204	0.01692	75.8	1.14	4.02	42.5	43.0	42.64±0.57	True
ESO 409-IG 015	False	False	False	1.38273	-28.09818	0.00244	8.2	0.83	3.88	39.4	39.8	38.81±0.57	True
HS 0017+1055	False	False	False	5.08917	11.20583	0.01885	84.6	1.27	4.70	41.1	41.9	41.37±0.57	False
2MASS J00203545-2751440	False	False	False	5.14779	-27.86225	0.02079	93.5	0.69	2.88	41.9	41.8	41.23±0.57	True
UGC 00521	False	False	False	12.80075	12.02525	0.00226	33.0	0.66	1.97	40.8	≤40.3	39.44±0.57	True
MCG +12-02-001	True	False	False	13.51664	73.08485	0.01576	70.6	0.65	4.82	43.3	44.0	43.74±0.57	False
UM 296	False	True	True	14.76710	1.00119	0.01782	79.9	0.93	3.89	42.0	42.4	41.44±0.23	True
MCG -01-03-072	False	False	False	15.59546	-4.50859	0.00584	25.9	1.54	3.52	39.4	≤39.9	38.96±0.57	True
SDSS J011136.95+001621.7	False	False	True	17.90399	0.27270	0.00628	27.9	1.04	3.39	39.8	≤40.0	38.50±0.23	True
GALEXASC J011551.69-393638.8	False	False	False	18.96581	-39.61122	0.02197	98.9	1.21	2.48	41.1	41.1	40.33±0.57	True
UGC 00819	False	False	False	19.00258	6.63703	0.00806	28.5	0.74	2.92	40.4	40.4	39.50±0.57	True
NGC 0520	True	False	False	21.14613	3.79242	0.00756	23.9	0.65	4.39	42.5	43.0	42.62±0.57	False
2MASS J01290606+5511020	False	False	False	22.27538	55.18392	0.01836	82.4	1.31	3.35	42.4	42.7	42.26±0.57	True
GALEXASC J013121.37+284812.1	False	True	False	22.83875	28.80333	0.01613	72.3	0.83	5.10	41.3	42.1	41.10±0.23	False
LSBC F613-V05	False	False	False	28.48752	13.46764	0.02068	93.0	1.05	3.49	41.7	42.0	41.47±0.57	True
GALEXASC J020645.07-365655.2	False	False	False	31.68796	-36.94894	0.02064	92.8	1.77	3.43	42.4	43.0	42.59±0.57	True
KUG 0204-106	False	False	False	31.81279	-10.40844	0.01863	83.6	0.75	4.57	41.4	42.0	41.43±0.57	False
GALEXASC J020827.99+322705.6	False	False	False	32.11708	32.45139	0.01682	75.4	1.39	4.86	41.0	42.0	41.43±0.57	False
NGC 0814	True	True	False	32.65679	-15.77358	0.00539	24.0	0.68	4.88	41.6	42.4	41.37±0.23	False
GALEXASC J021131.52+241253.8	False	False	False	32.88167	24.21500	0.00930	41.5	1.05	3.92	40.3	40.8	39.98±0.57	True
MRK 1039	False	True	False	36.89054	-10.16493	0.00704	20.0	0.94	5.20	40.9	41.8	40.70±0.23	False
AM 0234-652	False	False	False	38.84271	-65.26039	0.01930	86.7	1.26	3.45	42.6	43.0	42.60±0.57	True
SDSS J023850.49+272159.0	False	False	False	39.70833	27.36556	0.00489	21.7	0.71	2.55	40.3	40.1	39.18±0.57	True
SHOC 137	False	True	True	42.06638	-8.28792	0.00458	20.3	0.74	4.70	40.1	40.7	39.39±0.23	False
NGC 1377	True	True	False	54.16283	-20.90225	0.00591	23.4	1.99	3.70	42.1	42.8	41.99±0.23	True
FCOS 4-2106	False	False	False	54.37321	-34.99769	0.02193	98.7	1.29	3.01	41.1	41.3	40.64±0.57	True
SBS 0335-052	False	True	True	54.43359	-5.04450	0.01350	60.4	1.99	4.85	41.3	42.5	41.53±0.23	False
IRAS 03337+6725	False	False	False	54.60490	67.59092	0.00478	21.2	0.75	5.11	40.4	41.3	40.56±0.57	False
6dF J0356565-352240	False	False	False	59.23550	-35.37783	0.02218	99.8	0.90	3.54	41.3	41.6	40.95±0.57	True
6dF J0358492-413530	False	False	False	59.70479	-41.59161	0.02130	95.8	0.81	4.19	41.7	42.1	41.58±0.57	True
6dF J0410497-272959	False	False	False	62.70733	-27.49978	0.01192	53.2	1.09	3.12	40.5	40.6	39.80±0.57	True
2MASS J04111822-2314422	False	False	False	62.82596	-23.24511	0.00539	24.0	0.75	3.05	40.6	40.6	39.78±0.57	True
2MASS J04211939-3138045	False	False	False	65.33075	-31.63458	0.00851	37.9	1.13	2.69	41.8	41.8	41.21±0.57	True
FGC 0483	False	False	False	66.31421	4.98758	0.01653	74.1	0.79	2.69	42.1	42.0	41.37±0.57	True
2MASX J04275677+4050536	False	False	False	66.98663	40.84825	0.01963	88.2	1.77	3.89	42.3	43.0	42.61±0.57	True
IRAS 04277+5918B	False	False	False	68.00985	59.40909	0.01524	68.2	1.45	3.15	42.6	42.9	42.53±0.57	True
UGC 03097	True	True	False	68.95154	2.25805	0.01197	53.5	1.54	4.25	42.3	43.1	42.24±0.23	True
2MASX J04355886+4743034	False	False	False	68.99550	47.71747	0.02158	97.1	1.09	3.70	43.2	43.6	43.27±0.57	True

Table 3: continued.

Name	in 2MRS	H II	starburst	RA [°]	DEC [°]	z	D [Mpc]	*W1-W2* [mag]	*W2-W3* [mag]	log L (*W1*) [erg/s]	log L (*W3*) [erg/s]	log L^{nuc} (12 μm) [erg/s]	S18
(1)	(2)	(3)	(4)	(5)	(6)	(7)	(8)	(9)	(10)	(11)	(12)	(13)	(14)
UGC 03147	True	False	False	71.95737	72.86006	0.00963	47.1	0.84	4.61	42.2	42.9	42.47±0.57	False
2MASX J04483527-0449105	False	False	False	72.14696	-4.81958	0.01590	71.2	1.78	3.57	42.4	43.0	42.63±0.57	True
2MASS J04505295-3556304	False	False	False	72.72067	-35.94178	0.01759	78.9	1.30	4.35	42.3	43.0	42.62±0.57	True
2MASS J05150251-2624114	False	False	False	78.76042	-26.40300	0.01330	59.4	0.67	3.90	41.6	41.9	41.29±0.57	True
IRAS 05321+3205	False	False	False	83.83745	32.11793	0.00909	40.5	1.40	2.73	41.7	41.9	41.28±0.57	True
MCG +08-11-002	True	False	False	85.18212	49.69486	0.01916	86.0	0.68	4.26	43.3	43.7	43.47±0.57	True
NGC 2087	True	False	False	86.06679	-55.53244	0.01491	66.7	0.69	4.41	42.5	43.1	42.68±0.57	False
2MASX J05521634-8123257	False	True	False	88.06846	-81.39042	0.01285	57.4	0.83	4.39	42.3	42.9	42.02±0.23	False
UGCA 116	False	True	False	88.92750	3.39222	0.00265	10.3	1.40	5.49	40.8	42.0	40.98±0.23	False
IC 2153	False	True	False	90.02158	-33.91975	0.00956	42.6	0.66	4.85	41.8	42.5	41.57±0.23	False
UGC 03435	True	False	False	96.23817	82.31846	0.01440	64.4	0.75	4.07	42.9	43.3	43.00±0.57	True
ESO 308-IG 015	False	True	False	98.79371	-41.56119	0.01700	76.2	0.93	5.05	41.6	42.5	41.56±0.23	False
2MASX J06463429+6336323	False	True	False	101.64400	63.60909	0.01890	84.9	0.96	4.82	42.1	42.9	42.09±0.23	False
ESO 256-IG 009	False	False	False	104.13942	-45.17725	0.01412	63.2	0.91	4.91	41.8	42.6	42.18±0.57	False
HIZSS 003B	False	False	False	105.10227	-4.22013	0.00100	4.4	0.86	4.02	38.6	39.1	37.98±0.57	True
HIZOA J0701-07	False	False	False	105.60745	-7.31115	0.00584	25.9	0.74	6.04	40.7	41.8	41.25±0.57	False
HIZOA J0705+02	False	False	False	106.40715	2.63388	0.00582	25.9	0.86	4.09	40.9	41.3	40.65±0.57	True
IRAS 07155-2215	False	False	False	109.40867	-22.35272	0.00940	41.9	0.67	4.84	42.2	42.9	42.53±0.57	False
ESO 257- G 006	False	False	False	109.78892	-44.28869	0.01214	54.2	0.71	3.06	42.4	42.4	41.86±0.57	True
ESO 163- G 007	False	False	False	113.78563	-55.28668	0.00994	44.3	1.16	3.16	40.8	41.1	40.32±0.57	True
CGCG 058-009	True	True	False	113.93072	11.70932	0.01625	72.8	1.28	3.61	43.0	43.4	42.68±0.23	True
2MASX J08100697+1838176	False	True	False	122.52917	18.63836	0.01626	72.9	1.31	4.65	42.6	43.5	42.75±0.23	False
ESO 495- G 005	True	False	False	124.81142	-25.18797	0.00557	24.8	1.23	3.52	42.8	43.2	42.83±0.57	True
UGC 04459	False	False	False	128.53000	66.18167	0.00005	3.6	1.36	3.72	38.5	39.0	37.94±0.57	True
CGCG 331-070	True	False	False	133.21858	72.92656	0.01262	56.4	0.67	3.77	42.6	42.9	42.45±0.57	True
ESO 060- G 019	True	False	False	134.36133	-69.06008	0.00483	18.9	0.77	4.66	41.4	42.0	41.48±0.57	False
ESO 090-IG 014 NED03	True	False	False	135.40533	-64.27433	0.02204	99.2	0.84	3.89	43.2	43.6	43.32±0.57	True
2MASX J09224519-6845085	False	False	False	140.68842	-68.75239	0.01176	52.5	1.19	4.66	41.5	42.3	41.75±0.57	False
2MASS J09315693+4248577	False	False	True	142.98707	42.81609	0.01444	64.6	1.13	4.45	41.4	42.1	41.06±0.23	False
NGC 2964	True	True	False	145.72596	31.84739	0.00439	17.5	0.86	2.47	42.6	42.4	41.44±0.23	True
UGC 05189 NED02	False	True	True	145.73644	9.47116	0.01085	48.4	1.29	5.02	41.1	42.1	41.11±0.23	False
CGCG 007-025	False	True	True	146.00780	-0.64227	0.00482	21.4	1.35	4.77	40.5	41.4	40.17±0.23	False
2MASS J09472215+0044270	False	False	False	146.84223	0.74081	0.02013	90.5	1.75	4.54	41.8	42.8	42.38±0.57	False
CASG 46	False	False	True	149.76996	30.47364	0.02142	96.3	0.78	4.24	41.5	42.0	40.91±0.23	True
6dF J101101.7-144041	False	False	False	152.75864	-14.67686	0.00786	35.0	2.05	4.03	41.5	42.4	41.96±0.57	True
ESO 127- ?011	True	False	False	153.04942	-62.53339	0.01147	51.2	0.67	4.80	43.1	43.8	43.54±0.57	False
GALEXASC J101921.18-220835.0	False	True	False	154.83846	-22.14306	0.01214	54.2	1.21	4.87	41.1	42.0	40.98±0.23	False
2MASS J10242019-2014571	False	False	False	156.08400	-20.24931	0.01724	77.3	0.99	2.57	41.9	41.8	41.15±0.57	True
SDSS J1044+0353	False	True	True	161.24082	3.88698	0.01287	57.5	1.00	4.88	40.6	41.4	40.25±0.23	False
CTS 1020	False	True	False	161.93479	-20.96350	0.01241	55.4	0.68	5.18	41.4	42.2	41.17±0.23	False
ESO 264- G 050	True	False	False	163.61912	-46.21150	0.01957	87.9	0.81	3.06	42.8	42.9	42.44±0.57	True
CGCG 038-051	False	True	True	163.91321	2.39576	0.00341	21.7	0.75	4.28	40.1	40.6	39.17±0.23	True
LCRS B111014.3-021907	False	False	False	168.19754	-2.59083	0.00890	39.7	0.71	3.03	41.1	41.1	40.38±0.57	True
ECO 1305	False	True	True	169.68633	2.90836	0.02033	91.4	0.96	4.48	41.2	41.9	40.79±0.23	False
2MASS J11225861-2601456	False	False	False	170.74417	-26.02931	0.01176	52.5	1.04	2.95	41.9	42.0	41.40±0.57	True
UGC 06433	False	False	True	171.38254	38.06058	0.00704	31.3	0.73	5.03	40.9	41.7	40.61±0.23	False
NGC 3690 NED01	True	True	True	172.12925	58.56131	0.01022	45.6	1.50	3.59	43.7	44.2	43.68±0.21	True
WISE J113858.90-380041.9	False	False	False	174.74546	-38.01164	0.00896	39.9	1.29	2.98	40.9	41.1	40.35±0.57	True
6dF J115111.7-203557	False	True	False	177.79870	-20.59890	0.01217	54.4	1.12	4.75	41.4	42.3	41.27±0.23	False
UM 461	False	True	False	177.88896	-2.37276	0.00352	15.6	0.75	4.88	39.9	40.7	39.31±0.23	False
GALEXASC J115153.52-132447.1	False	False	False	177.97329	-13.41311	0.00674	30.0	0.81	5.30	40.5	41.4	40.70±0.57	False
MRK 0193	False	True	True	178.86808	57.66444	0.01726	77.4	1.46	4.69	41.4	42.4	41.38±0.23	False
SHOC 357	False	True	True	180.34295	2.18564	0.00325	14.0	1.83	3.98	39.7	40.5	39.04±0.23	True
ESO 380- G 027	False	True	False	186.44562	-36.23353	0.00934	41.6	1.13	4.42	40.5	41.2	39.96±0.23	False
MRK 0209	False	True	True	186.56539	48.49398	0.00100	5.7	0.66	4.45	39.3	39.8	38.26±0.23	False
2MASS J12265539+4242081	False	False	False	186.73081	42.70230	0.00890	39.7	0.86	4.20	40.7	41.2	40.53±0.57	True
2MASX J12294019-4007220	False	False	False	187.41742	-40.12272	0.01044	46.6	0.76	4.80	41.4	42.1	41.49±0.57	False

Table 3: continued.

Name	in 2MRS	H II	starburst	RA [°]	DEC [°]	z	D [Mpc]	*W1*-*W2* [mag]	*W2*-*W3* [mag]	log L (*W1*) [erg/s]	log L (*W3*) [erg/s]	log $L^{\rm nuc}$ (12 μm) [erg/s]	S18
(1)	(2)	(3)	(4)	(5)	(6)	(7)	(8)	(9)	(10)	(11)	(12)	(13)	(14)
ESO 322-IG 021	True	False	False	187.56675	-40.87131	0.01535	68.7	0.82	3.28	42.8	42.9	42.54±0.57	True
SDSS J123529.26+504803.4	False	False	False	188.87419	50.80194	0.00028	1.2	0.94	3.11	37.2	37.3	35.88±0.57	True
KUG 1243+265	False	False	True	191.54517	26.24915	0.00631	28.0	0.88	4.56	40.3	41.0	39.68±0.23	False
HIPASS J1247-77	False	False	False	191.88805	-77.58309	0.00138	3.2	1.63	3.79	37.8	38.4	37.18±0.57	True
UGCA 307	False	False	False	193.48566	-12.10540	0.00274	8.0	0.76	2.84	39.2	39.1	38.03±0.57	True
WISE J125949.83-322328.8	False	False	False	194.95754	-32.39136	0.01375	61.5	0.98	3.00	41.8	41.9	41.30±0.57	True
LEDA 200293	False	False	True	194.99062	2.05030	0.00292	12.9	0.69	5.18	40.1	41.0	39.67±0.23	False
GMP 1966	False	False	False	195.40133	28.15158	0.02007	90.2	1.52	3.15	42.0	42.3	41.83±0.57	True
ESO 443- G 035	False	False	False	195.53371	-29.21706	0.01313	58.7	0.79	4.26	41.3	41.8	41.21±0.57	True
MCG -02-33-098W	False	True	False	195.58120	-15.76810	0.01610	72.1	0.68	4.81	42.8	43.5	42.74±0.23	False
LEDA 045394	False	False	False	196.67681	-12.07282	0.02085	93.7	0.79	4.78	41.2	41.9	41.35±0.57	False
ESO 323-IG 083	False	True	False	196.83929	-38.91215	0.01398	62.5	1.71	5.31	40.9	42.2	41.20±0.23	False
LEDA 045469	False	True	False	196.90580	-35.64330	0.01393	62.3	0.92	4.47	40.9	41.5	40.37±0.23	False
SDSS J131447.36+345259.7	False	True	True	198.69736	34.88328	0.00288	12.8	0.98	4.97	39.9	40.8	39.45±0.23	False
2MASXi J1320008-195924	False	False	False	200.00350	-19.99019	0.02049	92.1	0.67	4.25	41.7	42.1	41.55±0.57	True
ESO 173- G 015	True	False	False	201.84908	-57.48950	0.00974	43.4	0.88	4.51	43.0	43.7	43.38±0.57	False
SDSS J132932.41+323417.0	False	False	False	202.38508	32.57142	0.01561	69.9	0.73	2.59	41.1	40.9	40.12±0.57	True
ESO 383-IG 043	False	True	False	204.28460	-32.92560	0.01209	54.0	1.21	4.78	40.9	41.8	40.68±0.23	False
NGC 5253	True	True	True	204.98318	-31.64011	0.00136	3.6	1.74	4.74	40.9	42.0	40.91±0.23	False
NGC 5471	False	True	False	211.12283	54.39647	0.00098	4.3	0.70	4.83	39.4	40.1	38.65±0.23	False
SDSS J141755.49+215534.2	False	False	False	214.48125	21.92619	0.01594	71.4	1.19	3.27	41.0	41.3	40.59±0.57	True
UGC 09164	False	False	False	214.68007	21.81612	0.00877	39.1	0.68	4.91	40.7	41.4	40.71±0.57	False
SBS 1420+544	False	False	False	215.66188	54.23589	0.02060	92.6	1.36	4.64	40.9	41.8	41.15±0.57	False
PKS 1444-301	False	False	False	221.97243	-30.30868	0.01600	71.7	1.08	2.86	42.3	42.3	41.84±0.57	True
GLIMPSE:[JKK2007] G1	False	False	False	222.15000	-60.12083	0.01522	68.1	0.73	3.90	42.5	42.8	42.40±0.57	True
SBS 1533+574B	False	True	False	233.55901	57.28430	0.01144	51.1	1.00	4.65	41.1	41.9	40.77±0.23	False
MRK 0487	False	True	True	234.26740	55.26406	0.00218	15.0	0.96	4.49	40.4	41.1	39.81±0.23	False
SBS 1543+593	False	False	False	236.08458	59.20672	0.00930	41.5	1.28	2.98	41.4	41.5	40.89±0.57	True
2MASX J15480728-4738187	False	False	False	237.03025	-47.63864	0.02077	93.4	0.89	3.66	43.4	43.7	43.45±0.57	True
SDSS J155320.20+420735.6	False	False	False	238.33416	42.12658	0.02164	97.4	1.09	3.10	41.2	41.3	40.65±0.57	True
SDSS J162054.53+622558.1	False	False	True	245.22685	62.43331	0.01005	44.8	0.82	4.26	40.6	41.1	39.88±0.23	True
2MASX J16241633-2209314	False	True	False	246.06817	-22.15883	0.01406	62.9	0.68	4.98	42.5	43.2	42.42±0.23	False
WKK 6774	False	False	False	246.16450	-56.33019	0.00891	39.7	1.08	3.91	42.3	42.8	42.38±0.57	True
ESO 101- G 007	True	False	False	250.14123	-67.45249	0.02202	99.1	0.90	3.26	43.1	43.3	42.93±0.57	True
ESO 069- G 011	True	False	False	252.47550	-71.20222	0.01722	77.2	0.94	3.19	42.6	42.8	42.32±0.57	True
IC 4662	True	False	False	266.78830	-64.63870	0.00101	2.3	0.66	4.78	39.4	40.0	39.11±0.57	False
CGCG 055-018	True	True	False	267.27879	8.10275	0.02117	95.2	1.18	3.44	43.6	43.9	43.32±0.23	True
MCG +03-45-037	False	False	False	267.84371	18.75218	0.01126	50.3	1.04	5.12	41.1	42.1	41.52±0.57	False
2MASX J18195279-4324572	False	False	False	274.96999	-43.41578	0.01204	53.8	0.68	4.59	42.1	42.7	42.28±0.57	False
ESO 338- G 008	False	False	False	292.55515	-39.40985	0.00941	42.0	1.36	4.80	40.6	41.5	40.90±0.57	False
2MASX J19331434+4101056	False	False	False	293.30971	41.01822	0.01575	70.5	1.94	3.08	42.8	43.3	42.99±0.57	True
2MASXi J1937323+234438	False	False	False	294.38488	23.74394	0.01334	59.7	1.16	2.86	42.7	42.8	42.32±0.57	True
IRAS 19402+0948	False	False	False	295.64750	9.92694	0.01722	77.2	1.00	3.84	42.4	42.8	42.40±0.57	True
CGCG 324-002	True	False	False	296.52263	64.14714	0.01881	84.4	0.65	3.98	42.7	43.0	42.64±0.57	True
AM 2040-620	True	False	False	311.04829	-61.98875	0.01096	48.9	0.72	1.07	42.3	41.5	40.80±0.57	True
GALEXASC J211258.71-462852.8	False	False	False	318.24550	-46.48167	0.01710	76.7	0.99	3.01	41.3	41.4	40.72±0.57	True
2MASS J21212094-1317300	False	False	False	320.33738	-13.29164	0.01111	49.6	1.08	2.41	41.4	41.3	40.59±0.57	True
ESO 343-IG 013 NED02	False	True	False	324.04627	-38.54250	0.01945	87.4	0.79	4.66	42.7	43.4	42.67±0.23	False
2MASX J21423859+4330562	True	False	False	325.66104	43.51581	0.01791	80.3	0.98	3.05	43.5	43.6	43.32±0.57	True
2MASS J22101082-5604285	False	False	False	332.54529	-56.07483	0.01360	60.8	0.97	2.90	41.5	41.5	40.85±0.57	True
GALEXASC J222611.41-282412.7	False	False	False	336.54784	-28.40351	0.01553	69.6	0.74	2.69	41.4	41.2	40.49±0.57	True
2MASX J22263365-2917276	False	False	False	336.64013	-29.29103	0.00342	15.2	1.01	2.75	40.9	40.8	40.06±0.57	True
SDSS J223831.12+140029.7	False	False	True	339.62967	14.00827	0.02061	92.6	1.73	4.56	41.1	42.1	41.08±0.23	False
FGC 2420	False	False	False	341.81000	75.75528	0.00518	37.2	2.46	1.83	40.9	41.1	40.33±0.57	True
KUG 2251+110	False	False	False	343.42644	11.27555	0.00748	33.3	0.85	5.07	40.6	41.4	40.73±0.57	False
GALEXASC J230718.90+231153.9	False	False	False	346.82875	23.19833	0.02099	94.4	0.76	4.56	41.3	41.9	41.28±0.57	False
UGC 12381	True	False	False	346.84521	43.60394	0.01546	69.2	0.93	3.13	42.8	42.9	42.53±0.57	True

Table 3: continued.

Name	in 2MRS	H II	starburst	RA [°]	DEC [°]	z	D [Mpc]	*W1-W2* [mag]	*W2-W3* [mag]	log L (*W1*) [erg/s]	log L (*W3*) [erg/s]	log L^{nuc} (12 μm) [erg/s]	S18
(1)	(2)	(3)	(4)	(5)	(6)	(7)	(8)	(9)	(10)	(11)	(12)	(13)	(14)
2MASX J23154464+0654391	False	False	False	348.93608	6.91089	0.00800	35.6	0.87	4.21	41.7	42.2	41.71±0.57	True
2MASS J23195620-3025139	False	False	False	349.98425	-30.42072	0.01390	62.2	0.84	2.72	41.6	41.5	40.80±0.57	True
UM 161 NED02	False	False	False	351.93500	-2.01317	0.01820	81.7	1.25	4.46	41.1	41.8	41.22±0.57	False
2MASX J23313624-1235537	False	False	False	352.90104	-12.59817	0.02120	95.4	2.35	3.92	42.4	43.4	43.08±0.57	True
2MASS J23352324-3945052	False	False	False	353.84692	-39.75144	0.01875	84.1	1.07	2.84	42.0	42.0	41.47±0.57	True
NGC 7770	True	True	False	357.84393	20.09652	0.01373	61.4	0.84	3.99	42.8	43.2	42.39±0.23	True
2MASX J23535252-0005558	False	False	False	358.46880	-0.09872	0.02196	98.8	1.83	3.53	42.1	42.7	42.24±0.57	True

– *Notes:* (1) object name, mostly following NED nomenclature; (2) flag whether the galaxy is in 2MRS; (3) and (4) flags whether galaxy has a H II or starburst classification, respectively; (5) and (6) equatorial coordinates of the object centre in J2000 in degrees; (7) redshift; (8) object distance in Mpc; (9) and (10) *WISE W1-W2* and *W2-W3* colours; (11) and (12) observed *W1* and *W3* continuum luminosities, calculated from the selected distance and the profile-fitting magnitudes. (13) nuclear 12 μm luminosity of an assumed AGN estimated from $L(W3)$ and optical type (see Sect. 4.1 for details); (14) flag whether the source fulfils the S18 criterion or not (see Sect. 4.4.1 for details);